EXPLORING THE INKJET PRINTING OF FUNCTIONAL MATERIALS AND THEIR USE IN ENERGETIC SYSTEMS AND SENSING APPLICATIONS

A Dissertation

Submitted to the Faculty

of

Purdue University

by

Allison K. Murray

In Partial Fulfillment of the

Requirements for the Degree

of

Doctor of Philosophy

December 2019

Purdue University

West Lafayette, Indiana

THE PURDUE UNIVERSITY GRADUATE SCHOOL
STATEMENT OF DISSERTATION APPROVAL

Dr. Jeffrey Rhoads, Co-Chair

School of Mechanical Engineering

Dr. George Chiu, Co-Chair

School of Mechanical Engineering

Dr. James Gibert

School of Mechanical Engineering

Dr. Bryan Boudouris

School of Chemical Engineering

Approved by:

Dr. Nicole Key

Head of the School Graduate Program

ACKNOWLEDGMENTS

I would like to thank my committee for their support and guidance. I am grateful for my advisors, Dr. Jeff Rhoads and Dr. George Chiu. They poured endless support and energy into helping me grow and believed in my potential. Their counsel will be forever appreciated.

Thank you to my family and loved ones for your unending encouragement. You have supported me in my studies and all other aspects of life. Thank you to my friends; you have made my graduate school experience incredible and I will always be grateful for your friendship.

I am ever grateful to the Stamps Family Charitable Foundation for the great gift of education. Being a Stamps Scholar put me on a path that led to this accomplishment. Thank you to Dr. and Mrs. Roe and Penny Stamps. Additionally, thank you to my Purdue Stamps Scholars for bringing me joy, growth, and a lot of fun.

Research is a road I traveled with many collaborators. Thank you to all those that shared in this work: Dr. Nikhil Bajaj, Dr. Bryan Boudouris, Nikhil Carneiro, Trevor Fleck, Dr. George Chiu, Dr. Emre Gunduz, John Hodul, Jillian Joffe, Lindsey May, Miranda McConnell, Joseph Meseke, Jacob Morris, Whitney Novotny, Allison Range, Dr. Jeffrey Rhoads, Zachary Siefker, Dr. Steven Son, and Michael Wadas.

This research was supported in part by the U.S. Department of Defense, Defense Threat Reduction Agency, through Grant No. HDTRA1-15-1-0010. Additionally, this research was supported by the National Science Foundation under Grant No. 1537988. The content of the information does not necessarily reflect the position or the policy of the U.S. federal government, and no official endorsement should be inferred. Additionally, this work was funded, in part, by the Center for High Performance Buildings at Purdue University.

TABLE OF CONTENTS

Page

LIST OF TABLES 6

LIST OF FIGURES 7

ABSTRACT 11

1. INTRODUCTION 12

2. PIEZOELECTRIC INKJET PRINTING OF NANOTHERMITES 16
   2.1 Introduction 16
   2.2 Materials and Methods 18
      2.2.1 Material Preparation 18
      2.2.2 Deposition Methods 19
      2.2.3 Side-View Imaging 19
      2.2.4 Sample Preparation 21
      2.2.5 Sample Testing 21
      2.2.6 Propagation Speed Calculations 22
   2.3 Results 22
      2.3.1 Side-View Imaging of Drop Formation 22
      2.3.2 Printer Robustness 23
      2.3.3 Propagation Speeds 25
   2.4 Discussion 28
   2.5 Conclusions 30

3. REACTIVE INKJET PRINTING OF NANOTHERMITES 31
   3.1 Introduction 31
   3.2 Experimental Methods 32
      3.2.1 Ink Preparation 32
      3.2.2 Inkjet Printing 33
   3.3 Results 37
   3.4 Conclusions 40

4. PIEZOELECTRIC INKJET PRINTED METALLIC IGNITERS 43
   4.1 Introduction 43
   4.2 Experimental Methods 44
      4.2.1 Sample Preparation 44
      4.2.2 Sample Testing 46
   4.3 Results 48
      4.3.1 Electrical Characterization 48
      4.3.2 Igniter Testing with Energetic Material 52

Page

4.4 Discussion . . . 54
4.5 Conclusions . . . 55

5. RESONANT MASS SENSORS FOR THE DETECTION OF TRAUMATIC BRAIN INJURY BIOMARKERS . . . 56
5.1 Introduction . . . 56
5.2 Methods . . . 57
5.3 Results . . . 60
5.4 Discussion . . . 62
5.5 Conclusions . . . 64

6. ADDRESSING THE PREDICTIVE CAPABILITIES OF VOLATILE ORGANIC COMPOUND SENSORS . . . 65
6.1 Introduction . . . 65
6.2 Materials and Methods . . . 67
6.2.1 Sensor Design and Fabrication . . . 67
6.2.2 Sensor Functionalization . . . 68
6.2.3 Sensor Testing . . . 70
6.3 Results . . . 71
6.4 Discussion and Conclusions . . . 74

7. SELECTIVE DETECTION OF AROMATIC HYDROCARBONS USING PIERCE OSCILLATOR SENSORS . . . 79
7.1 Introduction . . . 79
7.2 Experimental Methods . . . 81
7.2.1 Material Preparation and Characterization . . . 81
7.2.2 Sensor Configuration . . . 81
7.2.3 Device Functionalization . . . 83
7.2.4 Sensor Testing . . . 83
7.3 Results . . . 85
7.3.1 Chemical Characterization . . . 85
7.3.2 Sensor Testing . . . 85
7.4 Discussion . . . 92
7.5 Conclusions . . . 94

8. CONCLUSIONS . . . 96

REFERENCES . . . 99

VITA . . . 109

PUBLICATIONS . . . 110

LIST OF TABLES

Table Page

2.1 Multi-factor comparison of the piezoelectric inkjet printers examined herein as a method for the deposition of energetic material where + indicates a positive attribute and - indicates a negative attribute. 25

4.1 The effects of bridge wire length on failure. 49

4.2 The estimated breakdown voltage for three spark gap widths in air for needle- and sphere-like electrodes. The approximations begin to break down for gap widths below 1 mm because gaseous and surface discharge begin to play a role [92]. . . . 51

6.1 Functional chemistries inkjet printed on the resonators at 5 nL per device. All of the solvents and polymer were sourced from Sigma Aldrich. 69

6.2 Linear regression coefficients and coefficients of determination for each ink grouping where PMMA is polymethylmethacrylate and P4VP is poly(4-vinylpyridine). . 73

7.1 The minimum, mean, and maximum shift of resonator groups exposed to five pulses of 100 ppm of xylene. Note that the first group was not functionalized to account for temperature and humidity changes. 89

7.2 Functional materials deposited on the resonators for toluene, xylene, and trimethylbenzene selectivity tests. 90

LIST OF FIGURES

Figure Page

2.1 (a) An Aerotech Planar DL 200-XY, 200 mm travel, 0.5 μm accuracy linear positioning stage mounted beneath a MicroFab MJ-AL-01 piezoelectric nozzle, a MicroDrop MD-K-10 piezoelectric nozzle, and a PipeJet P9 piezoelectrically-actuated pipette; (b) MicroFab MJ-AL-01 80 μm piezoelectric nozzle schematic; (c) MicroDrop MD-K-130 70 μm piezoelectric nozzle schematic; and (d) PipeJet P9 500 μm pipe schematic. 20

2.2 Side-view imaging of drop formation captured with a Edmund Optics 3X 110 mm telecentric lens and EO-1312 color USB camera strobed with an LED at the nozzle firing frequency. (a) MicroDrop MD-K-130 printing 6% AlCuO with 0.5% polyvinylpyrrolidone (PVP) in dimethylformamide (DMF) strobed at 10 μs increments from 80 μs to 250 μs after the firing pulse. (b) MicroFab MJ-AL-01-80 printing 2% AlCuO with 1% PVP in DMF strobed at 5 μs increments from 40 μs to 125 μs after the firing pulse. (c) BioFluidix PipeJet P9 500 μm pipe printing 8% AlCuO with 0.5% PVP in DMF captured with a back lit BW Phantom Camera V 7.3. The images are captured at intervals of 0.5 ms. 24

2.3 Representative printed samples of aluminum copper (II) oxide printed with a PipeJet P9 500 μm pipe at 50 nL per drop. Pixels indicate the width of the lines. Layers indicate the thickness of the samples out of the page. (a) 1 pixel wide, 1 layer thick before initiation and (b) 1 pixel wide, 1 layer thick after initiation . . . 26

2.4 An image sequence obtained from a typical sample reaction: The flame propagation of a printed single pixel wide, single layer thick sample captured with BW Phantom Camera V 7.3 at 1 ms intervals. 27

2.5 The reaction location with respect to time as determined by tracking the greatest light intensity through frames of a high speed video for a single pixel wide, single layer sample. The experimental results are shown with a linear best fit overlay; R^2 of 99.98%. 27

2.6 Propagation speeds determined by tracking the greatest light intensity through frames of a high speed video captured with a BW Phantom Camera V 7.3, as obtained across all of the batches as a function of pixels and layers. The symbols indicate different sample batches. A batch is considered a set of samples printed in the same job from one vial of energetic material. 28

3.1 An Aerotech Planar DL 200-XY, 200 mm travel, 0.5 μm accuracy, linear positioning stage mounted beneath two MicroDrop MD-K-130-022 70 μm piezoelectric inkjet nozzles. 33

Figure Page

3.2 Side-view imaging of the drop formation realized with MD-K-130-022 nozzles as captured with an Edmund Optics 3X 110 mm telecentric lens and EO-1312 color USB camera strobed with an LED at the nozzle firing frequency. (a) The aluminum ink printed with a 143 V trigger pulse, 27 μs pulse width, 75 Hz firing frequency, and -8 mbar back pressure. (b) The copper (II) oxide ink was printed with a 93 V trigger pulse, 25 μs pulse width, 230 Hz firing frequency, and -8 mbar back pressure. 35

3.3 Four pass printing sublayer assignments. 36

3.4 Representative images of samples printed using two piezoelectric nozzles with a fuel ink and an oxidizer ink that is mixed in situ. The samples are squares with 10 drops per side. (a) A 3 layer nanothermite sample before ignition. (b) A 3 layer nanothermite sample after ignition. 38

3.5 Still frames of the reacting samples printed with 5 layers captured with a BW Phantom Camera V 7.3. (a) The ignition of 5 layer samples printed with a dual nozzle system and in situ mixing. (b) The ignition of 5 layer samples printed with a single nozzle and premixed nanothermite ink. 39

3.6 The maximum temperature reached by printed aluminum copper (II) oxide samples as observed with a FLIR SC2500 thermal imaging camera at 2,000 fps. 39

3.7 (a) An STEM image of a single nozzle sample; (b) an STEM image of a double nozzle sample; (c) and (d) the EDX mapping results collected from a portion of subfigures (a) and (b) respectively. Note that red, blue, and green areas denote the presence of copper, aluminum, and oxygen respectively. 41

4.1 Drop formation of the Metalon silver nanoparticle ink at 40 V, 1100 Hz as imaged from a side mounted camera (Edmund Optics, EO-1312 Color) with telecentric lens (3x, 110 mm WD). 45

4.2 (a) A bridge wire and (b) a 0.85 mm spark gap both printed with a single layer of an aqueous dispersion of silver on a flexible, mesoporous medium using a MicroFab piezoelectric inkjet printer. (c) Nanothermite printed on a spark gap, covering both electrodes, with a BioFluidix piezoelectrically actuated pipette. . . 46

4.3 A schematic of the test circuit used for bridge wire characterization. 47

4.4 The average power through the 1 mm bridge wire compared to the failure time. . 48

4.5 The voltage required for a spark discharge across the three different spark gap widths. 30 of 31 samples exhibited a spark-over behavior. 51

4.6 High-speed video schlieren images of the ignition of aluminum and bismuth (III) oxide nanothermite obtained with a printed igniter excited at 13.75 V using the test circuit detailed in Figure 4.3. The observed failure time was 70 μs. 52

Figure Page

4.7 (a) Unreacted nanothermite printed on a spark gap. (b)-(d) High-speed video images of the ignition of the printed nanothermite with a printed spark gap. . . . 53

5.1 (left) A close up view of a 16 MHz plate-style resonator prior to functionalization. (right) The same resonator after functionalization. 58

5.2 The piezoelectrically actuated pipette system. A 200 µm diameter nozzle was used to deposit 5.0 nL of anti-s100β and polystyrene in DMF onto the surface of each sensor. 59

5.3 The frequency response of a 16 MHz resonator driven by a 200 mV amplitude signal both before and after exposure to a solution of PBS containing s100β. The shift of the resonant frequency is caused by the adsorption of s100β onto the sensor's surface. 61

5.4 The resulting frequency shifts of the 28 sensors in the experimental group that were exposed to PBS and s100β and the 19 sensors in the control group that were exposed to PBS only. 61

6.1 A Pierce oscillator circuit with the oscillator (red) and a series of inverters (green) depicted along with the resonator board and instrumentation board offset to show electrical connections. 67

6.2 A graphical representation of the frequency counting method to accept 16 oscillator outputs and compute the corresponding oscillation frequencies every second with 1 Hz resolution 68

6.3 Representative view of a resonator (a) before and (b) after functionalization. Note the center of the resonator is coated with a thin film of poly(4-vinylpyridine). . . . 69

6.4 Schematic representation of the experimental apparatus used for oscillator-based VOC sensing. 70

6.5 The oscillation frequencies of 16 oscillators reported as shifts from the initial frequencies. The devices in (a) were left unfunctionalized as a reference channel and the remaining were functionalized with (b) 1 mg/mL of polymethylmethacrylate in toluene, (c) 0.3 mg/mL of polystyrene in toluene, and (d) 1 mg/mL of poly(4-vinylpyridine) in ethanol. The stacked color bars represent a makeup of the inlet gas at 150 ccm where yellow and purple indicate the methanol and toluene concentrations, respectively. 72

6.6 A subset of a single channel presented in Figure 6.5 to demonstrate the resolution achievable with the presented sensing method. This device was functionalized with polymethylmethacrylate. 73

6.7 The actual concentration of methanol (blue) and toluene (red) plotted against the predicted analyte concentration. An ideal fit would follow the black line. . . . 74

Figure Page

6.8 The residuals of methanol (blue) and toluene (red) plotted against the predicted analyte concentration. 75

7.1 A Pierce oscillator circuit with the oscillator (red) and a series of inverters (green) depicted along with the resonator board and instrumentation board offset to show connections. 82

7.2 Experimental setup for gas testing of oscillators for xylene detection. 84

7.3 Schematic illustration of the chemical synthesis functionalization of the HHCl SWCNTs. A diluted solution of HHCl in methanol ranging from 0.2 mg/mL to 100 mg/mL was drop cast printed onto SWCNTs and then dried under vacuum prior to device testing. 85

7.4 Raman spectra of SWCNTs before and after the drop casting of the 100 mg/mL HHCl solution. The Raman spectra shows similar peak locations and peak intensities before and after HHCl indicating that no structural changes occurred on the surface of the nanotubes. 86

7.5 Comparison XRD of the SWCNTs, SWCNTs after HHCl Treatment at 1 mg/mL, and HHCl separately. A different XRD pattern for each of the different samples was observed. Note important peak location at 38.11 for the SWCNTs after HHCl Treatment at 1 mg/mL. 87

7.6 Comparison XRD of the SWCNTs, SWCNTs after HHCl Treatment at 100 mg/mL, and HHCl separately. A different XRD pattern for each of the different samples was observed. Note important peak location at 48.6 for the SWCNTs after HHCl Treatment at 100 mg/mL. 88

7.7 The oscillation frequency of a single resonator functionalized with 0.2 mg/mL of HHCl and 0.1 mg/mL SWCNTs. The blue line indicates oscillation frequency and the yellow bars indicate the concentration of xylene in the chamber. 90

7.8 The oscillation frequency of devices exposed to 2000 ppm of either xylene, toluene, or trimethylbenzene. The blue lines represent the oscillation frequency of the device while the yellow, purple, and red bars indicate the concentration of xylene, toluene, and trimethylbenzene, respectively. The devices were functionalized as follows: (a) reference channels and (b) 1 mg/mL HHCl and SWCNTs. 91

ABSTRACT

Murray, Allison K. Ph.D., Purdue University, December 2019. Exploring the Inkjet Printing of Functional Materials and Their Use in Energetic Systems and Sensing Applications. Major Professors: Dr. Jeffrey F. Rhoads and Dr. George T.-C. Chiu, School of Mechanical Engineering.

With an eye towards applications such as the selective sensing of volatile organic compounds (VOCs) or micro-scale thrust generation, inkjet printing was explored as a means to selectively deposit functional materials. The work detailed herein explores a series of fundamental steps to gain expertise related to the piezoelectric inkjet printing of functional materials. The successful printing of nanothermite was demonstrated with two unique printing techniques. Furthermore, the integration of this material with an ignition mechanism was shown to create a fully printed igniter-energetic system. These advancements support future work related to the printing of other energetic materials necessary to create tunable reactive systems. This knowledge was then translated into the development of resonant mass sensing devices that are selectively functionalized using inkjet printing. This approach to functionalization allowed for the precise deposition of receptive chemistries on devices resulting in selective, highly-sensitive devices that successfully detected biomarkers secreted after traumatic brain injuries and harmful VOCs. This work implemented oscillator-based sensors to achieve a low-cost, low-power sensor platform with redundant elements. Furthermore, the predictive capabilities of these devices were explored using least squares and linear regression modeling.

1. INTRODUCTION

The work herein leveraged additive manufacturing for the selective deposition of reactive materials, sensitive chemistries, and metallic traces. This approach can open the door for many additional applications that require the selective deposition of materials with tailorable geometries or precise volumes. Presented herein are advancements related to the manufacturing of energetic material with integrated ignition sources. This work also encompasses the fabrication of selective volatile organic compound (VOCs) sensors. Through the use of additive manufacturing, sensor arrays capable of selectively detecting multiple analytes were developed. These advancements addressed practical limitations of current sensor platforms with regard to selectivity, scalability, and redundancy for improved predictive capabilities.

Additive manufacturing is used across many application spaces as a means of enabling tailorable design. For example, inkjet printing has proven advantageous for the manufacturing of components including metallic nanoparticles [1], carbon nanotubes functionalized with DNA [2], and/or hydrogels [3]. Inkjet printing has also previously been used to deposit trace quantities of energetic material for vapor detection standards [4, 5] and preliminary studies on the functional properties of reactives manufactured in this way have been conducted [6–9]. Additionally, inkjet printing has been shown to be a reliable sensor functionalization mechanism across many sensor platforms [10–14], due to its drop-on-demand, non-contact deposition approach that can be adaptive to the material and the desired form factor [15, 16].

The first study included in this work considered the additive manufacturing of energetic material as a foundational exploration into piezoelectric inkjet printing. Many practical applications require the use of miniaturized energetic materials, including microheating elements, micropower sources [17], micropropulsion systems [18,19], microactuation devices [19], and microinitiators [20, 21]. These use cases all require precisely controlled energy sources but pose manufacturing challenges due to their small form factors and reactive nature. To address these needs, nanothermites were explored, due to their high energy density and rel-

atively well understood performance [22–26]. However, there was a lack of understanding with regard to the relationship between the deposition system and the performance of the reactive materials. As such, Chapter 2 describes advancements in the inkjet printing of nanothermite and an analysis of the printing parameters that affected the propagation speed of the printed material.

When considering inkjet-based additive manufacturing as a means to develop reactive devices, safety and shelf stability of the ink may be of concern. As such, reactive inkjet printing, which is the use of adjacent nozzles containing different materials depositing at the same location, was explored to mitigate the risk of storing highly reactive inks without affecting the performance of the printed device. This approach leveraged drop kinetics to provide sufficient mixing energy to create a cohesive sample [27]. Previously, polyurethanes [28], self-assembled gold nanoparticles [29], and conductive silver films [30] were successfully printed using the two-component reactive inkjet printing method. This approach was advantageous for printing energetic material with multiple components, as it enabled the separation of the reactive ink into two relatively inert constituent inks, improving safety and shelf stability. Chapter 3 details advancements in reactive inkjet printing necessary to fabricate nanothermite samples with reaction temperatures similar to those samples printed with traditional inkjet printing. Transmission electron microscopy provided confirmation that the mixing of the constituent inks was sufficient to create a cohesive printed nanothermite sample.

The development of the techniques to print energetic material was motivated by the desire to create a fully printed initiation device that included reactive material and an ignition source. Some traditional ignition sources for energetic materials, such as bridge wires and spark gaps, require tedious fabrication processes, including some hand-made components. Due to the wide use of igniters, such as airbag triggering systems [31, 32], micropropulsion systems for microsatellites [33], and military ordnance [34, 35], the fabrication of these igniters would advance significantly if sample throughput was increased. Bridge wires, which utilize localized ohmic heating to react energetic materials [36, 37], and spark gaps, which leverage an electrode gap with localized voltage to create a spark and ignite electrostatically sensitive material [35, 38, 39], proved to be strong candidates for igniters manufactured with energetic material. Chapter 4 details the fabrication and electrical characterization of metal-

lic bridge wires and spark gaps. Additionally, these devices were implemented with printed nanothermite for a fully printed igniter system.

The methods used to characterize an ink and optimally print the aforementioned energetic materials and metallic inks could be applied to any unique material systems. For example, functional chemistries that react to certain analytes, as found in sensing applications, could be suitable candidates for inkjet printing. This approach allows for the volumetric control of the functional chemistry, as well as its location, which is essential in the development of highly selective sensing elements. Inkjet printing has been previously used for the functionalization of resonant mass sensor elements [10–14]. The adsorption of the analyte on the receptive resonant device results in a mass increase, and in turn a detectable resonant frequency shift. This has been utilized in many applications including research related to the detection of certain biomarkers in the medical field [40–43]. Chapter 5 details an investigation of an array of quartz resonators functionalized with the aforementioned inkjet printing methodology. This chapter demonstrates the ability to create devices sensitive to a biomarker commonly secreted after a traumatic brain injury with a test sample volume in the nanoliter range. This approach is translatable to a wide array of applications within, and tangential to, the biological space.

Extensive reviews of the dynamics and applications of linear, resonant mass sensors, such as the devices presented in Chapter 5, have been performed [44]. These devices have been further studied in the non-linear regime [12–14, 45, 46]. Adding to the field, there has been progress related to the use of oscillators as sensing elements [47–51]. However, much of this work was geared toward improving the detection limits associated with the analytes of interest, rather than providing technologies that can scale to practical field implementation. This gap between successful laboratory sensing advancements and deployable analyte detectors is multifaceted. One element of this challenge is the lack of predictive sensing capabilities in current sensors [52, 53]. To find widespread adoption, sensing platforms need to develop a means of identifying specific analytes and deliver quantitative measures of the analyte concentration [54–58]. Chapter 6 details work with a multi-channel sensing array based upon Pierce oscillators functionalized with inkjet printing and integrated with a frequency counting algorithm. This approach facilitated simultaneous data collection of 16 parallel channels

with 1 Hz frequency resolution and 1 s temporal resolution. This experimental approach also allowed for the implementation of a linear-regression model and least-squares solution to predict the concentration of two analytes of interest based on the frequency shifts of 16 oscillators. This work provides an avenue for addressing the limitations of current VOC sensors through a low-cost, low-power sensing platform that is integrable with a predictive model.

To expand on the work presented in Chapter 6, the oscillator-based sensing approach was applied to a VOC of interest, xylene, which has shown to be toxic even at low concentrations [59, 60]. Previously, VOCs have been primarily detected using photo ionization detectors (PIDs), amperometric detectors, semiconductors (resistive sensors), portable gas chromatographs, electronic noses/sensor arrays, and optical sensors [61–69]. These sensors are capable of xylene detection at low concentrations but lack selectivity and have high power requirements [52, 70]. As such, the need for a low-cost, low-power xylene sensor with selectivity was well established. Chapter 7 describes an oscillator-based xylene sensor capable of detecting xylene at or below 100 ppm. It also provides evidence that support claims of selectivity to xylene when the device is exposed to toluene and trimethylbenzene, aromatic hydrocarbons with one less and one more methyl group than xylene, respectively. This advancement is notable due to the meaningful signal to noise ratio achieved at 100 ppm and the implementation of redundant channels to improve detection confidence.

This work is a series of advancements in the additive manufacturing of functional materials, specifically leveraging inkjet printing as a means to create tunable devices, from energetic material systems to sensing platform. The contributions also spread beyond additive manufacturing to the deployment of VOC sensor arrays, manufactured using additive techniques.

2. PIEZOELECTRIC INKJET PRINTING OF NANOTHERMITES

The following chapter is reprinted, in part, from A. K. Murray *et al.* "Selectively-Deposited Energetic Materials: A Feasibility Study of the Piezoelectric Inkjet Printing of Nanothermites" which appeared in *Additive Manufacturing* [71].

2.1 Introduction

With the miniaturization of many engineering components that contain energetic material, there exists a need for manufacturing technologies that are capable of seamlessly functionalizing micro-scale electronics with reactive or energetic materials. For example, microheating elements, micropower sources [17], micropropulsion systems [18, 19], microactuation devices [19], and microinitiators [20, 21] all require robust electronic packages with precisely located energy sources. These devices pose manufacturing challenges due to the lack of techniques suitable for the micrometer-scale deposition of energetic material. This chapter proposes the use of piezoelectric inkjet printing for the selective deposition of energetic materials to allow for a degree of volumetric and spatial control that is not obtainable with current energetic deposition methods. This control will permit the integration of electronics with energetic material, opening the door for a multitude of micro-energetic applications.

Nano-energetic materials have been shown to be useful for MEMS applications and thus have been widely studied for a number of years [22, 23]. Within this class of materials, nanothermites are gaining popularity due to their notable, highly-exothermic reactions and relatively simple synthesis processes [23]. Nanothermites also offer significant energy density, which can be advantageous when integrating energetic materials into small areas. Currently, solutions for the deposition of energetic material include electrophoresis [24], magnetron sputtering [72], and doctor blade casting [73]. These methods allow for the bulk deposition of energetic materials on a substrate but lack sub-millimeter spatial control. Because of

this, basic geometries, which are necessary for the integration of energetic material into electronics, are difficult to achieve with these methods.

Across many industries, inkjet printing has proven to be beneficial for the small-scale deposition of functional inks for fabricating components including carbon nanotubes functionalized with DNA [2], metallic nanoparticles [1] and/or hydrogels [3]. Extensive reviews of current micro- and nano-scale printing technologies have been conducted [74, 75]. Of the many inkjet printing systems one could choose from, piezoelectric inkjet printing is advantageous due to the flexibility of ink composition that this print head design allows. In this approach, nozzles are actuated by the change in shape of a piezoelectric material. Reservoirs are either squeezed, bent, or pushed based on their design [16]. In contrast to a thermal inkjet head, which uses flash boiling to produce droplets [16], piezoelectric inkjet printing achieves droplets without affecting the ink thermally. This is potentially safer and more reliable for sensitive ink compositions, including energetic materials.

Previous work has utilized inkjet printing for the deposition of small quantities of energetic material for the development of trace vapor calibration tools [4, 5]. These samples are not necessarily intended for energetic performance but instead are manufactured as standard test samples for sensor performance validation. There has also been investigation into the effect of ink deposition parameters on the morphological changes of cyclotrimethylenetrinitramine (RDX) [6]. Initial studies of inkjet printing as a deposition method for nanothermites, on a scale that allows for reaction rather than just detection, have been conducted [7–9]. These initial works demonstrate multi-layer, single-width lines of printed nanothermites on glass slides with high ignition fidelity; however, they do not study the effects of geometric or printer parameter variation on combustion performance.

This work further investigates the use of piezoelectric inkjet printing of nanothermites as a suitable method for the controlled deposition of energetic material for the development of samples with functional geometric features. It explores the utility of three deposition systems in the precise spatial and volumetric control of deposited aluminum copper (II) oxide. The systems are evaluated for drop formation reliability, robustness to high ink solids loading, and the ignition fidelity of the printed energetic material. In addition, the work demonstrates the energetic performance of the printed samples as characterized by

propagation speed measurements. This class of measurement is widely used as an initial metric for nanothermite performance evaluation [24–26]. Finally, this work demonstrates a deposition system that allows for printed material flexibility and the spatial control of the deposited energetic material, as well as the integration of energetic material with small-scale components such as electronics.

2.2 Materials and Methods

2.2.1 Material Preparation

Due to its thermal stability, aluminum copper (II) oxide nanothermite was formulated as an energetic ink to test the capabilities of several commercial deposition systems. To prepare the material, copper (II) oxide nanoparticles (Sigma Aldrich, 50 nm) were mixed with aluminum nanoparticles (NovaCentrix, 80 nm, 82% active aluminum) and suspended in a solution of dimethylformamide (DMF) and polyvinylpyrrolidone (PVP), a surfactant.

The nanoparticles were mixed at stoichiometric ratios per the ideal reaction:

$$2\mathrm{Al} + 3\mathrm{CuO} \rightarrow \mathrm{Al_2O_3} + 3\mathrm{Cu}$$

and placed in a 10 mL syringe (BD, slip tip) [76]. DMF with 0.5% by weight PVP was added to the syringe to achieve an 8% solids loading. Airtech Flashbreaker 1 tape was placed over the tip of the syringe to prevent leaking. The syringe was then loaded into a custom polytetrafluoroethylene (PTFE) holder and secured on a LabRAM resonant mixer (Resodyn Acoustic Mixer, Inc.). The syringe was mixed at 80% intensity for 16 min and inverted after 8 min [76]. After mixing was complete, the contents of the syringe were emptied into a 1.5 mL microcentrifuge tube, the material was weighed, and additional DMF was added to achieve a desired solids loading. The tube was sealed and stored until the print process commenced.

This ink formulation was chosen based on the results of a previous study on the viscosity and settling time of aluminum and copper (II) oxide nanoparticles in DMF with various surfactants [77]. It was found that the surfactant concentration that optimized ink stability while limiting the impact on reactivity was 0.5% PVP by weight of the solids. The viscosity

of the ink used in these experiments was not tested because of concern for accidental ignition of the energetic material. However, both of the constituents inks of aluminum in DMF with PVP and copper (II) oxide in DMF with PVP had viscosities of 0.862 ± 0.035 mPas [77]. The surface tension of the aluminum copper (II) oxide ink used herein was 30.5 mN/m as measured with the pendant drop technique using a Ramé-Hart goniometer, model 500.

Immediately before printing, the microcentrifuge tube was suspended in a Branson 1800 sonicating bath (Branson Ultrasonics) for 30 min to redistribute any particles that may have fallen out of suspension. The solution was loaded into the deposition system 5 min after sonication finished.

2.2.2 Deposition Methods

Three deposition systems were evaluated in this work to determine the most effective process for reliable nanothermite printing. All of these systems are variations of open-end piezoelectric inkjet printers. These print heads consist of an ink reservoir connected to a pump chamber. This chamber includes a piezoelectric actuator that can deliver a prescribed displacement pulse which forces droplets through the nozzle orifice [78].

The three print heads tested in this work were a 70 μm piezoelectric nozzle (MicroDrop MD-K-130), an 80 μm piezoelectric nozzle (MicroFab MJ-AL-01-80), and a 500 μm piezoelectrically-actuated pipette (BioFluidix PipeJet P9). These print heads were mounted above a dual-axis linear positioning stage (Aerotech Planar DL 200-XY, 200 mm travel, 0.5 μm accuracy) as seen in Figure 2.1(a). These components were controlled through an in-house developed LabView script. The stage position was integrated with the nozzle firing to fabricate complex geometries.

2.2.3 Side-View Imaging

Each printer was evaluated using side-view drop formation analysis techniques. For the MicroFab and the MicroDrop systems, this was achieved using a 3X 110 mm telecentric lens with a color USB camera (Edmund Optics EO-1312). Specifically, the camera, nozzle, and a light-emitting diode (LED) were applied in series. The LED illuminated the nozzle and

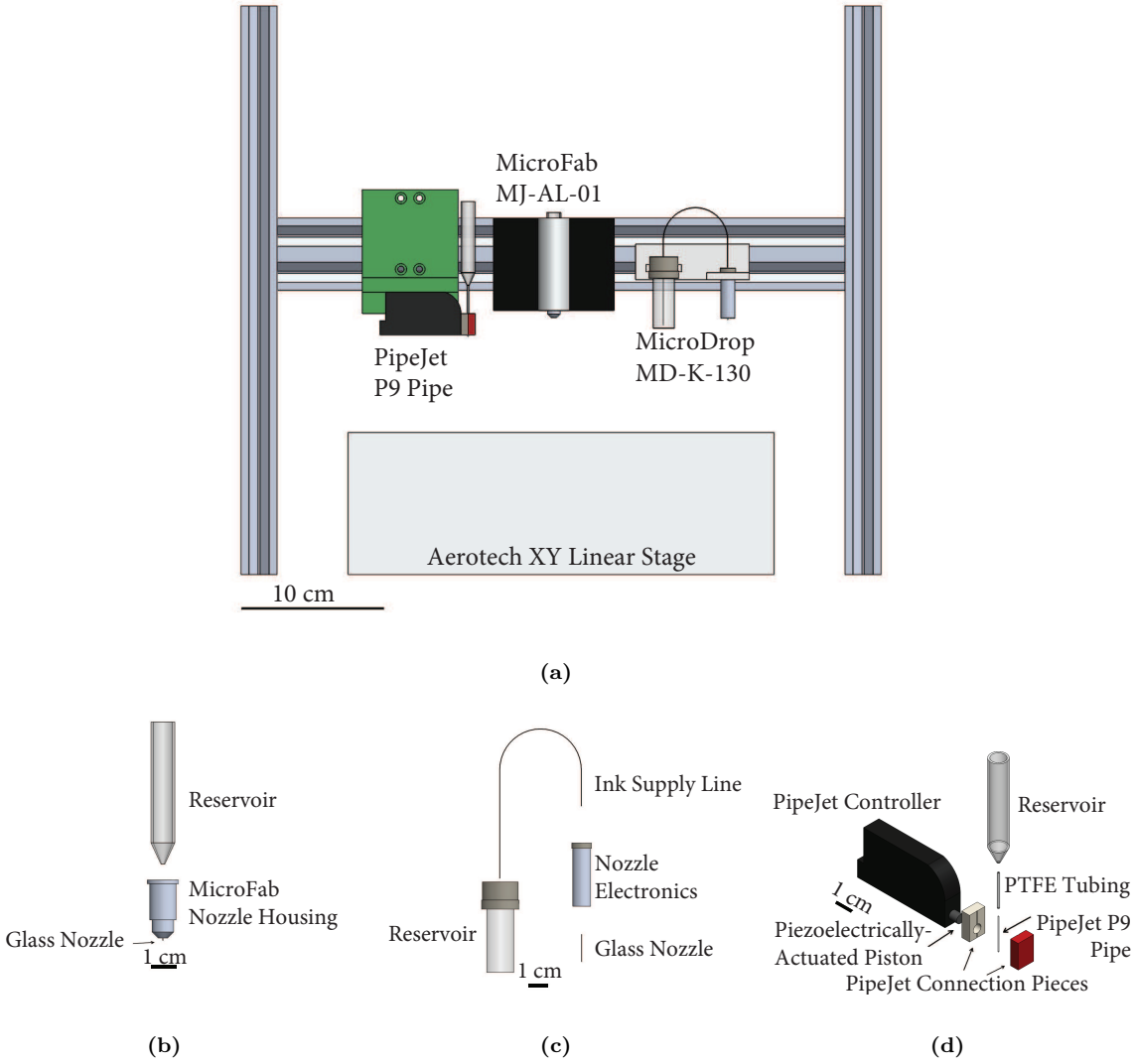

Figure 2.1. (a) An Aerotech Planar DL 200-XY, 200 mm travel, 0.5 μm accuracy linear positioning stage mounted beneath a MicroFab MJ-AL-01 piezoelectric nozzle, a MicroDrop MD-K-10 piezoelectric nozzle, and a PipeJet P9 piezoelectrically-actuated pipette; (b) MicroFab MJ-AL-01 80 μm piezoelectric nozzle schematic; (c) MicroDrop MD-K-130 70 μm piezoelectric nozzle schematic; and (d) PipeJet P9 500 μm pipe schematic.

droplet at the nozzle firing frequency. Phase shifting the LED strobe allowed for droplet observation at various positions in flight. The BioFluidix PipeJet P9 drop formation was captured with a Black and White (BW) Phantom Camera V 7.3 (Vision Research, Inc.) in series with the back lit nozzle. Printing was recorded at 4000 frames per second (fps) with an exposure time of 240 μs.

2.2.4 Sample Preparation

To validate printed energetic performance, samples were prepared with the PipeJet P9 system due to its reliability. The 500 μm P9 pipe was attached to a 2 cm piece of 1.6 mm inner diameter PTFE tubing. The tubing was secured to a 3 mL luer lock syringe (Terumo) via a barbed socket connector. The syringe was fixed to a back pressure regulation system (MicroFab) to prevent the undesirable loss of material during the printing process. The nanothermite was deposited on Novele, a mesoporous media which promotes strong adhesion and uniform deposition (NovaCentrix, IJ-220) [79]. This substrate improved geometric control for the printed material because the adhesion prevented the undesirable wetting previously seen on silicon substrates. Further, Novele may be used in final applications. The energetic material was deposited at volumes of 50 nL per drop; this equated to approximately 4.5 μg/drop as calculated from the mass of printed samples with 225, 450, and 675 drops. The samples were printed from a bitmap of a 6 pixel circle with a 25 pixel long line attached. When printing, the pixels corresponded to a single drop and were spaced at 0.6 mm. The circles, approximately 3.6 mm in diameter, were printed to allow for an increased surface area for initiation. The printed lines were approximately 15 mm long. Three line widths of 1, 2, and 3 pixels were printed, approximately 0.8, 1.6 and 2.4 mm wide respectively. Samples of all of the line widths were deposited with 1, 3, and 5 layers of material.

2.2.5 Sample Testing

Printed samples were ignited using a capacitive discharge unit (Information Unlimited). Initiation was focused at the center of the circle and the reaction along the line was observed

with a BW Phantom Camera V 7.3 (Vision Research, Inc.). Videos were captured at 20,000 fps with an exposure time of 20 μs.

2.2.6 Propagation Speed Calculations

For all of the reactions, each frame of the high speed video was analyzed. In any given image, the column with the greatest average light intensity was found. This was then correlated to a horizontal flame position using the resolution of the camera. By analyzing each image in series, the reaction position with respect to time was tracked. Propagation speeds were calculated as the slope of a linear best fit of the distance and time data.

2.3 Results

As previously noted, the work herein was completed using aluminum copper (II) oxide nanothermite suspended in a solution of polyvinylpyrrolidone (PVP) and dimethylformamide (DMF). Evaluation of the three printing systems was completed largely experimentally rather than analytically because typical analytical measurements, such as viscosity, presented a safety concern with the required amounts of energetic ink.

2.3.1 Side-View Imaging of Drop Formation

To evaluate the three deposition systems, drop formation was first investigated. Because maintaining consistent particle suspension was challenging with the high solute-to-solvent density ratio of the ink used for printing, it was critical that reliable drop formation be achieved. Acceptable droplet formation consisted of a droplet head forming, followed by a tail. As the droplet continued to form, the tail pinched off from the nozzle. As it fell to the substrate, the tail began to rejoin the head of the droplet [80]. Satellite drops, undesirable small droplets formed outside of the main drop, were deemed acceptable in this application if they followed the same trajectory as the main droplet, due to the assumption that they would impact the substrate within the spatial bounds of the original drop.

Representative side-view images for each of the printer systems can be found in Figure 2.2. The systems were tested with the material at the highest solids loading, up to an 8% limit, that allowed for repeatable printer performance. It can be seen that the MicroDrop system achieved reliable drop formation with a consistent secondary drop following the main drop's trajectory with a 6% solids loading aluminum copper (II) oxide nanothermite suspension in Figure 2.2(a). This resulted in repeatable print performance from the MicroDrop system. The MicroFab system was unable to achieve this level of quality with the energetic ink used for the testing, a 2% solids loading aluminum copper (II) oxide suspension. As seen in Figure 2.2(b), this nozzle exhibited significant wetting near the nozzle orifice; an inconsistent meniscus formed on the nozzle face. This was due, in part, to the solvent used, DMF, which is not recommended for the MJ-AL-01 nozzles. Due to the wetting effect, the drop tail did not snap off at the nozzle orifice but instead necked near the head of the drop. This resulted in unstable drop formation and inconsistencies in drop volumes. Because of the poor drop formation reliability in this application, this system was deemed impractical for the energetic ink. Drop formation of an 8% solids loading aluminum copper (II) oxide suspension printed with the BioFluidix system is displayed in Figure 2.2(c). This system produces significantly larger drops than the other systems tested due to the 500 μm nozzle orifice. Droplets exhibited necking as a pinch off for drop formation with a spherical drop falling after pinching.

The drop formation process was not analyzed further within this study; however, ongoing work is exploring the effect of drop formation on the material's reactive performance.

2.3.2 Printer Robustness

To achieve high sample throughput, the deposition methods described above were required to demonstrate a certain level of robustness. The two main components for this metric are solids loading capacity and the time scale over which acceptable print performance could be maintained; a summary of other considerations is presented in Table 2.1. Due to the frequent nozzle clogging exhibited by the MicroFab nozzle with this ink, energetic material could not be printed at solids loadings higher than 2%. In turn, sample ignition

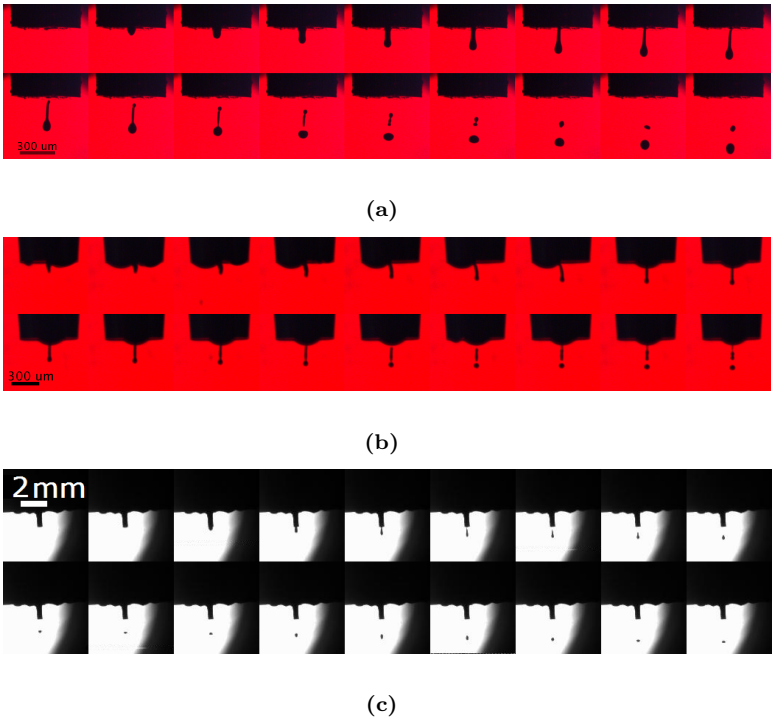

Figure 2.2. Side-view imaging of drop formation captured with a Edmund Optics 3X 110 mm telecentric lens and EO-1312 color USB camera strobed with an LED at the nozzle firing frequency. (a) MicroDrop MD-K-130 printing 6% AlCuO with 0.5% polyvinylpyrrolidone (PVP) in dimethylformamide (DMF) strobed at 10 μs increments from 80 μs to 250 μs after the firing pulse. (b) MicroFab MJ-AL-01-80 printing 2% AlCuO with 1% PVP in DMF strobed at 5 μs increments from 40 μs to 125 μs after the firing pulse. (c) BioFluidix PipeJet P9 500 μm pipe printing 8% AlCuO with 0.5% PVP in DMF captured with a back lit BW Phantom Camera V 7.3. The images are captured at intervals of 0.5 ms.

Table 2.1.
Multi-factor comparison of the piezoelectric inkjet printers examined herein as a method for the deposition of energetic material where + indicates a positive attribute and - indicates a negative attribute.

Manufacturer	MicroDrop	MicroFab	BioFluidix
Model	MD-K-130	MJ-AL-01	PipeJet P9
Nozzle Orifice	70 μm	80 μm	500 μm
Droplet Volume	20 - 180 pL	20 - 300 pL	10 - 60 nL
Viscosity Range	$\leq$ 20 cP	$\leq$ 20 cP	1 - 200 cP
Print Quality Lifetime	+	-	+
Cleaning	-	+	-
Ink Flexibility	+	-	+
Parameter Control	+	+	-
Sample Throughput	-	-	+
Clogging	-	+	+
Ease of Use	+	-	+
Nozzle Cost	-	-	+

was difficult to achieve. As such, the MicroFab system was determined to be less ideal for this ink formulation. The MicroDrop system proved reliable at a solids loading of 6%, allowing for high ignition fidelity from printed samples. However, due to the 70 μm nozzle orifice, the reservoir/nozzle interface design with a small diameter ink supply line, and the agglomeration of nanoparticles, clogging was a frequent problem. The BioFluidix PipeJet system achieved reliable multi-hour print performance at an 8% solids loading with minimal user input. Sample preparation was repeatable within a material batch and the energetic performance proved reliable. However, due to the larger nozzle orifice, the observed drop volume for the PipeJet system was about 50 nL; and this larger droplet footprint resulted in a loss in spatial precision as compared to the other systems investigated.

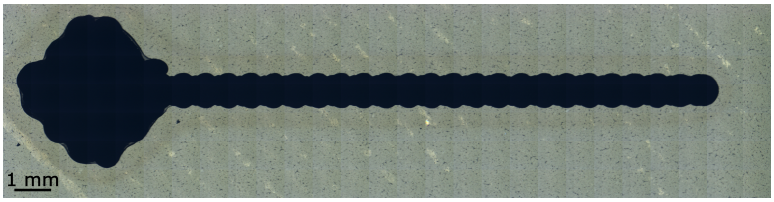

(a)

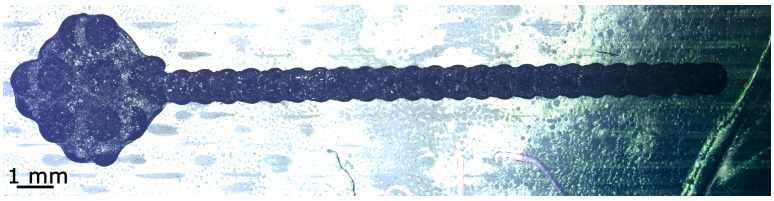

(b)

Figure 2.3. Representative printed samples of aluminum copper (II) oxide printed with a PipeJet P9 500 μm pipe at 50 nL per drop. Pixels indicate the width of the lines. Layers indicate the thickness of the samples out of the page. (a) 1 pixel wide, 1 layer thick before initiation and (b) 1 pixel wide, 1 layer thick after initiation

2.3.3 Propagation Speeds

As a means to evaluate the combustion performance of the printed material, the PipeJet P9 500 μm pipe was used to prepare samples that highlighted the relationship between reaction propagation speed and the geometry of a printed sample. The samples were tested no sooner than 24 hr after they were printed in an effort to eliminate the effect of solvent retention on the reaction performance. Images of representative printed samples before and after ignition can be seen in Figure 2.3.

Figure 2.4 shows still images from a representative high speed video of sample ignition with width and thickness as 1 pixel and 1 layer, respectively. Figure 2.5 demonstrates the flame front position tracking for the sample in Figure 2.4. The best fit line approximation found the propagation speed to be 2.7 m/s. As seen, the reaction propagation is nearly constant.

Figure 2.6 offers a comprehensive look at the propagation speeds across the two parameters varied in this study: line width (pixels) and thickness (layers). The nominal widths

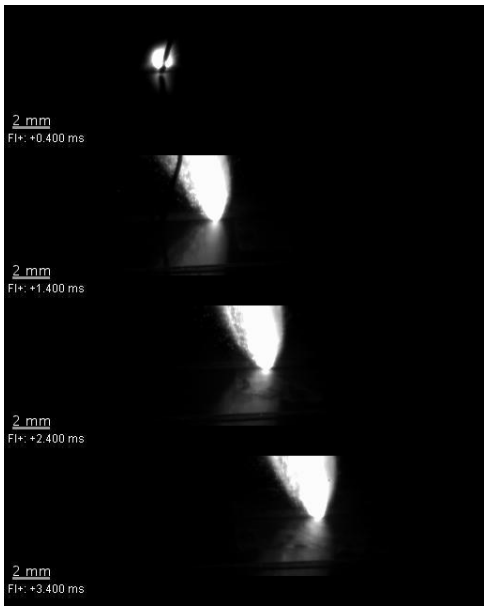

Figure 2.4. An image sequence obtained from a typical sample reaction: The flame propagation of a printed single pixel wide, single layer thick sample captured with BW Phantom Camera V 7.3 at 1 ms intervals.

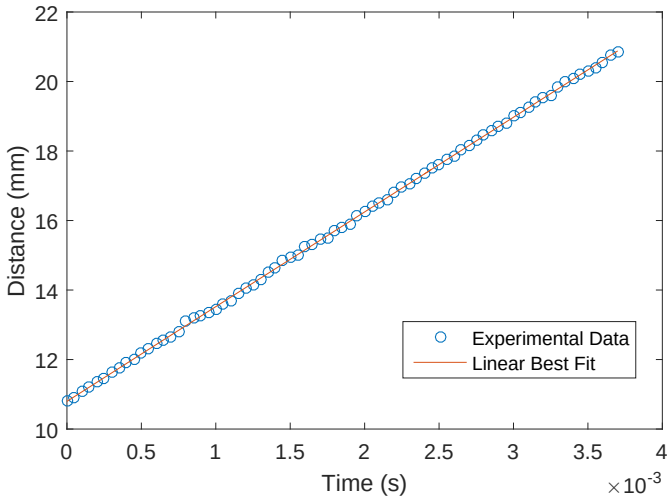

Figure 2.5. The reaction location with respect to time as determined by tracking the greatest light intensity through frames of a high speed video for a single pixel wide, single layer sample. The experimental results are shown with a linear best fit overlay; R^2 of 99.98%.

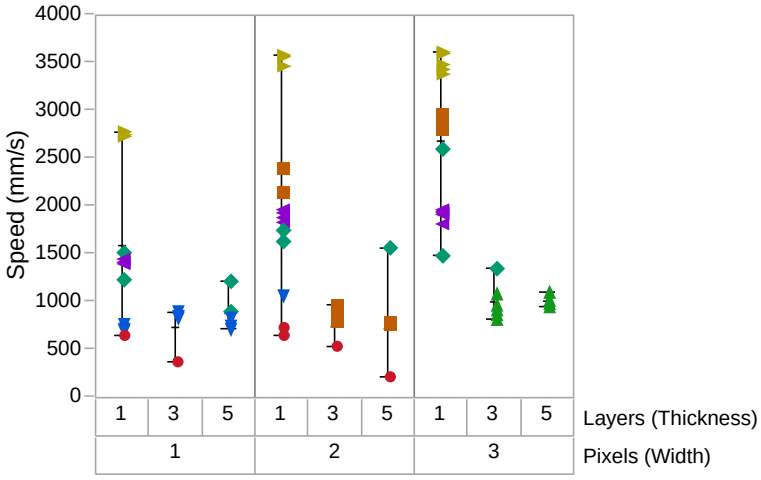

Figure 2.6. Propagation speeds determined by tracking the greatest light intensity through frames of a high speed video captured with a BW Phantom Camera V 7.3, as obtained across all of the batches as a function of pixels and layers. The symbols indicate different sample batches. A batch is considered a set of samples printed in the same job from one vial of energetic material.

of the lines for 1, 2 and 3 pixels were 1.1 ± 0.2 mm, 1.7 ± 0.3 mm, and 2.1 ± 0.2 mm, respectively. The symbols used in Figure 2.6 indicate the batch from which samples were printed. A batch is a set of samples printed in the same job from one vial of energetic material. There is a wide variation for the thinnest samples considered. However, relatively consistent results were obtained for multi-layered samples.

2.4 Discussion

As previously noted, each of the printing systems examined for nanothermite deposition had inherit benefits and drawbacks, as detailed in Table 2.1. Overall, the system must reliably deposit the energetic material to achieve controlled geometries and deposited volumes. In prior work, it was found that the MicroFab system was the best suited for the deposition of metal inks for circuit design due to the use of a manufactured ink with well defined parameters [81]. However, reliable drop formation could not be achieved with the energetic ink. The MicroDrop system has proven to be the most robust for the small-scale deposition of low

solids loading energetic material. This system delivers small enough quantities of energetic material to for allow micrometer precision in deposited geometry. However, the significant cleaning and clogging issues, attributable to the lengthy siphon tube at the nozzle/reservoir interface, limit solids loading below practically useful values. The BioFluidix system has the most potential for a wide range of energetic material due to its ability to deposit material with a wide range of viscosities. However, the deposition occurs on the order of nanoliters rather than picoliters, preventing the extent of small-scale spatial control that the other systems offer.

The printed energetic material proved to have repeatable propagation performance when evaluated within a particular batch, where a batch is defined as a set of samples printed in the same job from one vial of energetic material; however, significant interbatch variation was observed. As seen in Figure 2.6, the batch-to-batch variation outweighs significant conclusions that could be made about the data set as a whole, especially for the 1 layer cases. Within any particular batch, it was seen that the width of a line, in pixels, was a factor. However, on the whole it was not a strong factor. There were no apparent trends attributable to the number of layers deposited. This is supported by previous electrophoretic deposition work of aluminum copper (II) oxide which suggests material thickness does not affect the propagation speed until a film is 50 μm thick [24]. The measured thickness of the printed samples were 10-30 μm as determined by a Hirox 3D Microscope.

The ink-substrate interaction is a critical area of future study within this class of work. Due to the wicking behavior of the substrate, the single drops or rows of drops had crisp boundaries. However, this substrate behavior implies a variable surface roughness that could cause an inconsistent density of energetic material resulting in unpredictable reaction behavior. An extensive study is necessary in the future to fully understand the substrate's impact on the reaction with the deposited energetic material.

The potential sources of the significant interbatch variability include: inconsistencies in mixing processes; nanoparticles settling out of suspension in storage or in the printing reservoir resulting in different printed solids loadings; variability of the deposited mass due to low solids loading and small drop volume; unknown substrate and ink interactions; variability

in the substrate absorption potential; and shelf stability of the printed samples. The potential sources of variability will be investigated in future work to fully isolate process effects.

2.5 Conclusions

This work successfully demonstrated the ability to use inkjet printing for the small-scale deposition of an energetic material. This opens avenues for energetic integration into small-scale electronics and/or micropropulsion components, which previously were unattainable due to the lack of spatial control in energetic deposition techniques such as doctor blading, magnetron sputtering, and electrophoresis. Utilizing piezoelectric inkjet printing, energetic material was deposited with basic geometric features: lines of varying widths and thicknesses. The propagation speeds of the deposited material were measured through high speed imaging techniques. Within a material batch, it was found that line width and burn rate were correlated; however, no trends were attributed to the number of layers printed. In addition, inter-batch variability was a significant problem currently preventing such conclusions on a batch-to-batch level.

The primary goal for future work in this topical area will be to determine the source of the significant batch variation observed in the propagation speeds. This includes investigating how the mesoporous substrate variability affects the energetic ink; how the mixing processes contribute to material inconsistencies; and how material degradation over time affects printed material performance.

3. REACTIVE INKJET PRINTING OF NANOTHERMITES

The following chapter is reprinted, in part, from A. K. Murray *et al.* "Two-Component Additive Manufacturing of Nanothermite Structures via Reactive Inkjet Printing" which appeared in the *Journal of Applied Physics* [82].

3.1 Introduction

In the growing field of micromechanical devices, there is a subset of systems that require the microscale integration of energetic material. These applications range from micropropulsion systems [18, 19] to microinitiators [20, 21]. However, there is an inherent risk associated with handling energetic materials that limits the diversity of materials deposited using traditional methods, such as electrophoresis [24], doctor blade casting [73], and conventional inkjet printing [7–9]. In addition, methods such as electrophoresis and doctor blade casting lack the spatial and volumetric control of the deposited energetic material that is advantageous in the aforementioned microscale applications.

In many industries, reactive inkjet printing, the process of combining one droplet of ink A with a droplet of ink B to produce a new material, has been used to overcome material incompatibilities with inkjet printers [27]. Full reactive inkjet printing has been used for the deposition of polyurethanes [28], self-assembled gold nanoparticles [29], and conductive silver films [30]. Due to the separate nature of the inks, reactive inkjet printing opens the door for the fabrication of devices using a wider range of materials. The individual inks can be fine tuned with the appropriate solvent or surfactant for only one key element rather than trying to optimize an ink formulation for many constituents, as in traditional inkjet printing. In addition, materials that are volatile when mixed together can remain separate until the fabrication process to improve material safety and handling. The most significant challenge with this process lies in the significant coordination of the printer systems to achieve reliable droplet placement of the inks respective to one another. However, this can be mitigated

with a well-controlled fabrication system. Ultimately, this technique has been shown to produce picoliter volumetric control and microscale spatial precision in the deposition of new materials previously unobtainable with inkjet printing, due to material property and safety concerns.

This work utilized a piezoelectric inkjet printer for the side-by-side deposition of colloidal suspensions of aluminum and copper (II) oxide nanoparticles. These suspensions were printed sequentially such that their droplets were partially overlapping. This method resulted in the localized mixing of two inert components that produced a nanothermite. This nanothermite was analyzed with high speed thermal imaging and scanning transmission electron microscopy to compare its reaction performance and constituents to that of nanothermite printed with a single-nozzle piezoelectric inkjet printer.

3.2 Experimental Methods

3.2.1 Ink Preparation

As a means to test reactive inkjet printing as a method for the manufacturing of nanothermite samples, two ink suspensions, a fuel and an oxidizer, were prepared and printed, and the resulting samples were tested for energetic performance. These suspensions were created to achieve a stoichiometric ratio of solids when the inks were mixed volumetrically 1:1. An aluminum and a copper (II) oxide nanoparticle suspension, of 3.5% and 6% volumetric solids loading respectively, were prepared in dimethylformamide (DMF) with 0.5% polyvinylpyrrolidone (PVP) immediately prior to printing [77]. The copper (II) oxide nanoparticles (Sigma Aldrich, 50 nm) and aluminum nanoparticles (NovaCentrix, 80 nm, 82% active aluminum) were deposited in 1.5 mL microcentrifuge tubes. Subsequently, a solution of DMF with 0.5% PVP was added to the vials. These vials were then suspended in a sonicating bath (Branson Ultrasonics) for 30 min. The solution was loaded into the inkjet printer 5 min after sonication finished.

As a comparison, a pre-mixed aluminum copper (II) oxide suspension was mixed at a 6% volumetric solids loading [76]. To prepare the material, copper (II) oxide nanoparticles were mixed with aluminum nanoparticles and suspended in a solution of DMF and PVP and

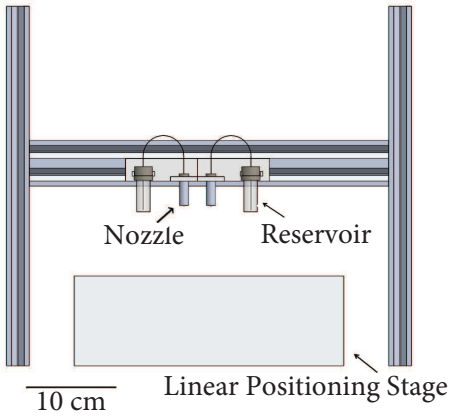

Figure 3.1. An Aerotech Planar DL 200-XY, 200 mm travel, 0.5 μm accuracy, linear positioning stage mounted beneath two MicroDrop MD-K-130-022 70 μm piezoelectric inkjet nozzles.

placed in a 10 mL syringe (BD, slip tip). The syringe was loaded into a custom polytetrafluoroethylene (PTFE) holder and secured on a LabRAM resonant mixer (Resodyn Acoustic Mixer, Inc.). The syringe was mixed at 80% intensity for 16 min and inverted after 8 min.

3.2.2 Inkjet Printing

The prepared inks were loaded into 70 μm piezoelectric inkjet nozzles (MicroDrop, MD-K-130-022) and secured above a dual-axis linear positioning stage (Aerotech Planar DL 200-XY, 200 mm travel, 0.5 μm accuracy) that was controlled by an in-house LabView program, see Figure 3.1.

For the samples printed with dual nozzles, the aluminum nanoparticle ink, ink α herein, was printed with a 143 V trigger pulse, 27 μs pulse width, 75 Hz firing frequency, and -8 mbar back pressure. The copper (II) oxide nanoparticle ink, ink β herein, was printed with a 93 V trigger pulse, 25 μs pulse width, 230 Hz firing frequency, and -8 mbar back pressure. These settings were optimized for quality droplet formation as observed using side-view imaging with a 3X 110 mm telecentric lens and a color USB camera (Edmund Optics EO-1312) backlit by a light emitting diode (LED). Acceptable droplet formation consisted of a droplet

head forming at the nozzle orifice, followed by the necking of the droplet to produce a tail. This droplet then pinched away from the orifice as it fell to the substrate. The majority of the tail morphed back into the main droplet while the remainder produced a small satellite drop. The satellite drops were deemed acceptable in this study if they fell within the spatial bounds of the main drop. Representative drop formation images can be found in Figure 3.2.

Samples were prepared using a four pass printing method in which a 10 pixel by 10 pixel square bitmap was parsed into four sublayers, described herein as A, B, C and D. Each pixel was assigned to one of the sublayers using the pattern shown in Figure 3.3. Sample preparation was achieved by printing sublayers A and D using ink β immediately followed by the printing of sublayers B and C with ink α. This pattern was repeated to achieve the desired number of layers; however, the sublayer associated with a particular ink alternated with each layer. For example, ink β was printed from sublayers A and D on layer 1 but sublayers B and C on layer 2. Samples of 3, 5, and 7 layers were printed on Novele, a mesoporous media which promotes strong adhesion and uniform deposition (NovaCentrix, IJ-220) [79].

A pre-mixed aluminum copper (II) oxide nanothermite ink was printed using the same 10 pixel by 10 pixel square bitmap and a 70 μm piezoelectric inkjet nozzle (MicroDrop, MD-K-130-022) on Novele to offer a comparison to the dual nozzle system.

After sufficient drying, printed samples were ignited using a capacitive discharge unit (Information Unlimited). The ignition was observed with a Black and White (BW) Phantom Camera V 7.3 (Vision Research, Inc.) at 20,000 fps with an exposure time of 48 μs and an SC2500 infrared camera (FLIR Systems, Inc.) at 2,000 fps with an exposure time of 6 μs.

Samples prepared with the two different printing methods were examined with a scanning transmission electron microscopy (STEM, Titan 80-300 kV Environmental Transmission Electron Microscope) equipped with an X-ray energy dispersive spectroscopy (EDX) detector to compare localized mixing and the spatial distribution of the aluminum and copper (II) oxide particles. The inks were directly deposited on copper mesh carbon coated TEM grids and dried in air.

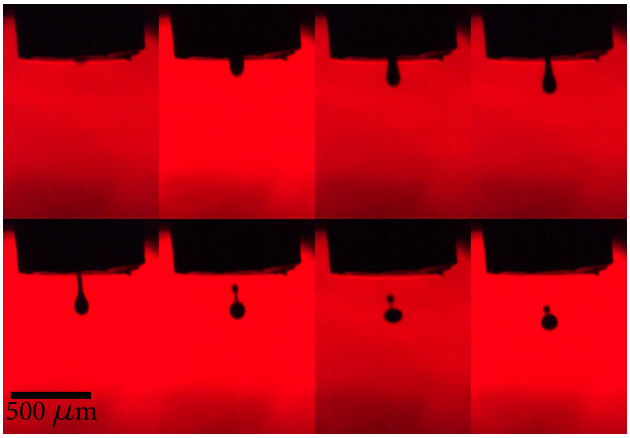

(a)

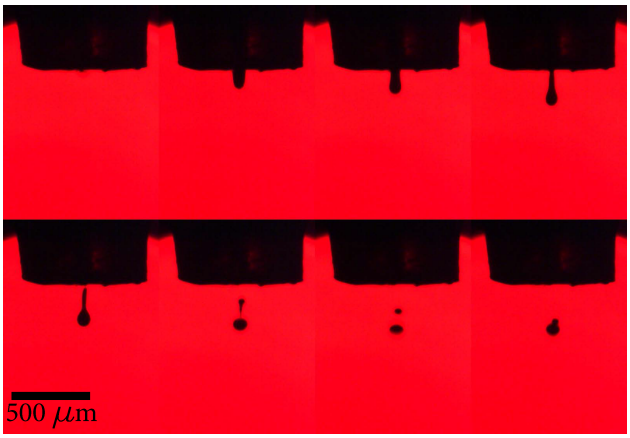

(b)

Figure 3.2. Side-view imaging of the drop formation realized with MD-K-130-022 nozzles as captured with an Edmund Optics 3X 110 mm telecentric lens and EO-1312 color USB camera strobed with an LED at the nozzle firing frequency. (a) The aluminum ink printed with a 143 V trigger pulse, 27 μs pulse width, 75 Hz firing frequency, and -8 mbar back pressure. (b) The copper (II) oxide ink was printed with a 93 V trigger pulse, 25 μs pulse width, 230 Hz firing frequency, and -8 mbar back pressure.

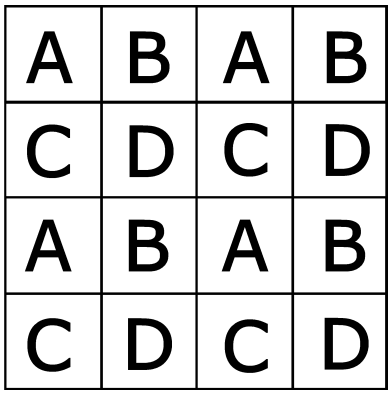

Figure 3.3. Four pass printing sublayer assignments.

3.3 Results

Representative images of the printed samples before and after ignition are shown in Figure 3.4.

The ignition of the dual and single nozzle samples were qualitatively compared using a high speed camera as an initial proof of concept for the dual nozzle manufacturing technique. The ignition progression of a 5 layer sample prepared with dual nozzle printing is shown in Figure 3.5(a). The corresponding ignition of a 5 layer sample prepared with pre-mixed ink using a single nozzle system is found in Figure 3.5(b). These images suggested comparable reaction performance due to the brightness and time scale of the reaction. As such, the samples were tested further with infrared thermography and scanning transmission electron microscopy (STEM).

The maximum temperature reached by the nanothermite samples, as determined by high speed infrared thermography, is shown in Figure 3.6. These measurements were taken assuming an emissivity of 1, thus the reported temperature is a lower bound. The data suggests that there is approximately a 200 K difference in maximum reaction temperature between the dual nozzle and single nozzle printed samples. Both types of samples reached peak temperatures above 1000 K. Samples with 5 and 7 layers had overlapping bounds of peak reaction temperature. This result confirms that there is reasonable reaction performance of the samples created with the dual nozzle system when compared to that of the samples printed using a single nozzle. When sufficient material is deposited, the two methods produce samples that are qualitatively similar. The dual nozzle technique results in samples that are slightly inferior, quantitatively, but still demonstrate acceptable relative performance for many applications. As such, this indicates that the dual nozzle system is a viable deposition technique that improves upon the safety of the single nozzle system without notably compromising reaction performance.

Representative STEM images for single nozzle, Figure 3.7(a); the sequentially deposited dual nozzle samples, Figure 3.7(b); and the corresponding EDX mapping from the insets, Figures 3.7(c) and 3.7(d), clearly show the contrast between the copper (II) oxide and aluminum nanoparticles and that both methods are consistent with each other with respect to

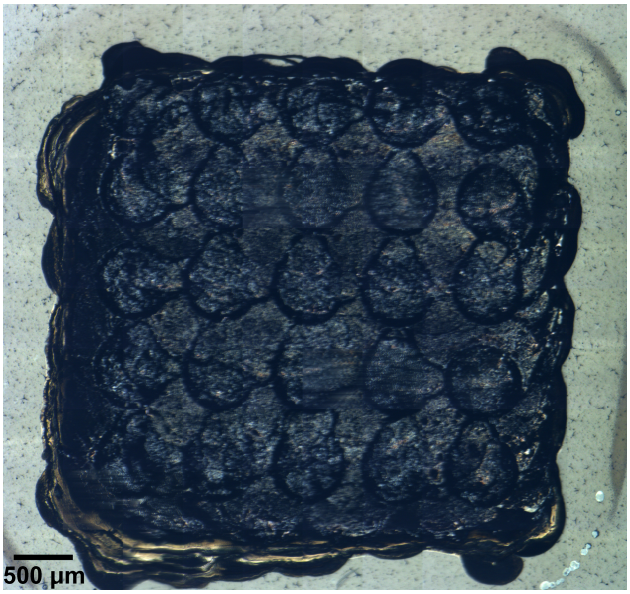

(a)

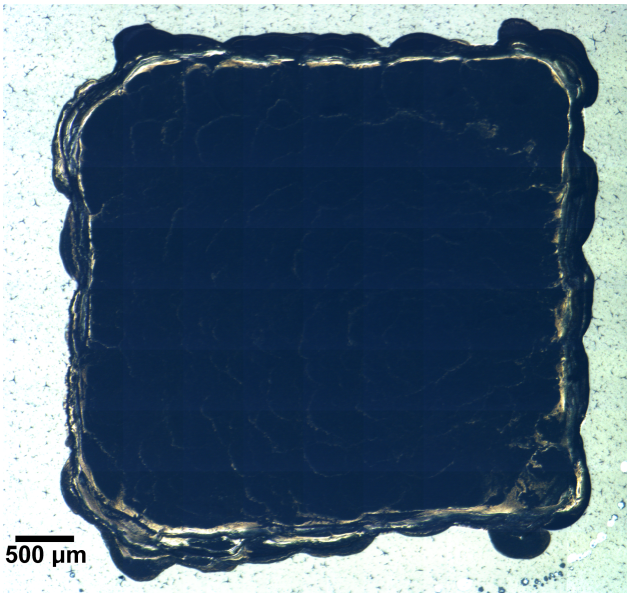

(b)

Figure 3.4. Representative images of samples printed using two piezoelectric nozzles with a fuel ink and an oxidizer ink that is mixed in situ. The samples are squares with 10 drops per side. (a) A 3 layer nanothermite sample before ignition. (b) A 3 layer nanothermite sample after ignition.

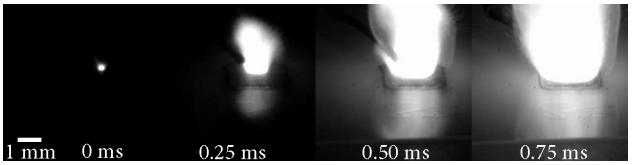

(a)

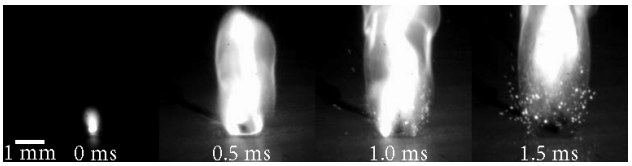

(b)

Figure 3.5. Still frames of the reacting samples printed with 5 layers captured with a BW Phantom Camera V 7.3. (a) The ignition of 5 layer samples printed with a dual nozzle system and in situ mixing. (b) The ignition of 5 layer samples printed with a single nozzle and premixed nanothermite ink.

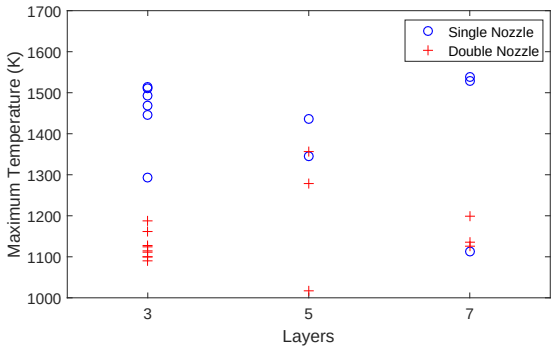

Figure 3.6. The maximum temperature reached by printed aluminum copper (II) oxide samples as observed with a FLIR SC2500 thermal imaging camera at 2,000 fps.

the particle distributions; these results are indicative of several identical samples tested at multiple locations on the sample. The single nozzle sample shows a mixture of agglomerates of copper (II) oxide and aluminum nanoparticles, with length scales for both agglomerate sizes and mixing on the order of 100s to 1000s of nanometers. It is probable that the resonant mixing method used for the pre-mixed ink is not completely effective in breaking up the agglomerates, which might limit the degree of mixing. On the other hand, the dual nozzle samples show a more layered structure. Interestingly, uniform layers of copper (II) oxide nanoparticles were observed to cover only the layer of aluminum nanoparticles, possibly due to the preferential wetting of the aluminum nanoparticle layer and subsequent drying. The thickness of the copper (II) oxide nanoparticle layer was about the size of the agglomerates, so the degree of mixing is quite similar to the single nozzle case. This is due to the minute volume of the individual droplets that only deposit a very small amount of nanoparticles. This indicates that a dual nozzle system is a viable safer alternative to a single nozzle system containing a premixed nanothermite solution. Uniquely, it can also be used to produce multilayered structures with tailorable characteristic thicknesses that can have different reaction rates by only modifying inkjet printing rates.

3.4 Conclusions

This work demonstrates the ability to perform in situ mixing of a fuel and an oxidizer to produce a nanothermite with notable energetic performance. Suitable inkjet printing of two colloidal suspension inks was achieved and used for the precise deposition of material with picoliter-scale volumetric control. When sufficient material was deposited, there was no qualitative difference between the combinatorial printing method and traditional inkjet printing. Quantitatively, the dual nozzle samples produced slightly less heat than the single nozzle samples, but still operated within acceptable ranges. By utilizing two part reactive printing, materials can be mixed and stored as inert components which improves safety and shelf stability. In addition, the separation allows for ink tuning based on one key component rather than a mixture of constituents, as required with conventional inkjet printing. This method opens the door for integrated deposition and mixing techniques for delivering precise

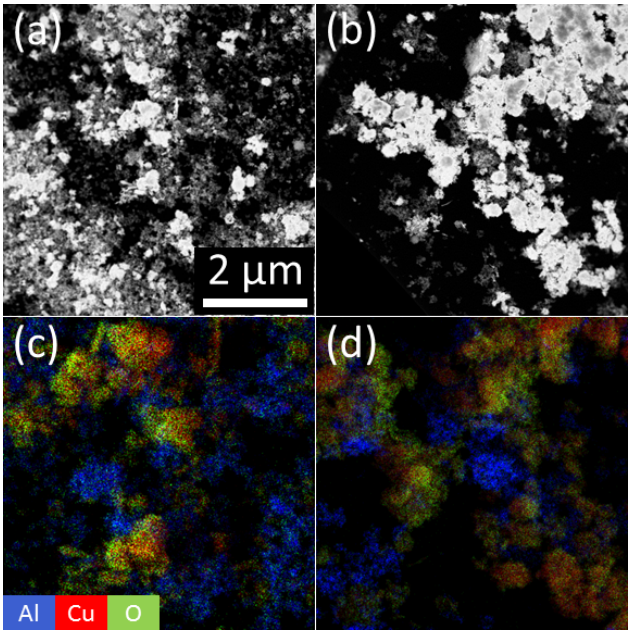

Figure 3.7. (a) An STEM image of a single nozzle sample; (b) an STEM image of a double nozzle sample; (c) and (d) the EDX mapping results collected from a portion of subfigures (a) and (b) respectively. Note that red, blue, and green areas denote the presence of copper, aluminum, and oxygen respectively.

quantities of energetic material without the added safety concern of handling energetic material prior to deposition. It can also be easily translated to other multi-component materials that are incompatible with traditional inkjet printing.

The work presented herein provides a proof of concept for the use of reactive inkjet printing as a means to fabricate nanothermite samples. However, there are many avenues to still explore in this area of interest. For instance, there is a need to develop a technique for the bulk characterization of the samples in future work. It is acknowledged by the authors that the SEM imaging of a small component of a sample is not sufficient to definitively represent the bulk properties of the printed materials due to the significant size discrepancy. In addition, the deposition feature size is an avenue of future exploration, particularly as to how it relates to the overall energetic performance of the material. This initial proof of concept and testing provide ground work for the future development of this technique as it applies to energetic materials.

4. PIEZOELECTRIC INKJET PRINTED METALLIC IGNITERS

The following chapter is reprinted, in part, from A. K. Murray *et al.* "Piezoelectric Inkjet Printed Metallic Igniters", which appeared in the *Journal of Imaging Science and Technology* [81]. A subset of this work was also reported in W. A. Novotny "Inkjet Printing of Metallic Initiators" [83].

4.1 Introduction

Initiators and igniters are used in a wide variety of applications in both the civilian and military sectors. These applications include airbag triggering systems [31, 32], micropropulsion systems for microsatellites [33], and military ordnance [34, 35]. Two such igniters are spark gaps and bridge wires. Spark gaps consist of two electrodes that are separated by a small distance, typically a fraction of a millimeter to a few millimeters. A high voltage, but relatively low current, is passed across these two electrodes resulting in an electrical breakdown spark-over. This ignites a relatively sensitive component of the energetic material and subsequently relies on propagation for the remainder of the material to ignite [35, 38, 39]. Bridge wires, on the other hand, consist of a thin wire that is designed to ignite energetic material from ohmic heating or wire vaporization [36, 37].

The current methods of fabrication for bridge wires and spark gaps are time consuming and tedious; many devices are fabricated by hand. This study explores the development of printed igniters that are fabricated using a piezoelectric inkjet printer. This method has proven to be an easy and efficient means for rapid production, while allowing for a wide material selection [84–86]. A printed bridge wire or spark gap has the advantages of automated fabrication, low cost, and device-to-device performance repeatability at scale, provided certain conditions are met. Additionally, it has been demonstrated that some energetic materials, when made into a dispersion, can also be utilized in an inkjet printing system, allowing for rapid system integration [71, 87].

Other methods of printing, such as lithography, flexography, gravure, and screen printing, rely on repeatedly transferring the ink to the substrate using a previously built master pattern. Inkjet printing uses the deposition of drops to additively build up a pattern. This allows the pattern to be changed with each print, which is difficult to realize with other methods [15].

This work used a flexible polyethylene terephthalate (PET) based substrate that promotes adhesion between the substrate and ink, which allowed for the deposition of a conductive trace without the need for thermal curing. Fabrication of the igniters without thermal curing was ideal to smooth the transition between silver printing and energetic material printing in the manufacturing process.

The objective of this work was to explore the use of piezoelectric inkjet printing as a means of rapidly fabricating printed spark gap and bridge wire igniters. The geometric features of the spark gaps were varied to determine the effect of the gap width on the spark-over voltage. Similarly, the bridge wire length was varied to investigate the effect of wire length on break time. Both types of devices were then functionalized with an inkjet-printed nanothermite to validate their respective performance as an ignition mechanism for energetic material.

4.2 Experimental Methods

4.2.1 Sample Preparation

The igniters in this work were fabricated with a piezoelectric inkjet printer (MicroFab MJ-AL-01-80) secured above a dual-axis linear positioning stage (Aerotech Planar DL 200-XY, 200 mm travel, 0.5 μm accuracy). The stage and nozzle were controlled with an in-house LabView program that coordinated the firing of the nozzle with the location of the stage. This resulted in the development of printed geometries using a zigzag printing path built from bitmap images in which each bit corresponded to 5 drops of silver ink. The samples were printed on a flexible, mesoporous printing medium (NovaCentrix, IJ-220) with an aqueous dispersion of silver nanoparticles (NovaCentrix, JS-B25HV, 25 wt% Silver) filtered with a 1 μm filter (Chroma Fil Extra, GF-100/25). This substrate was used due to its polymer coating

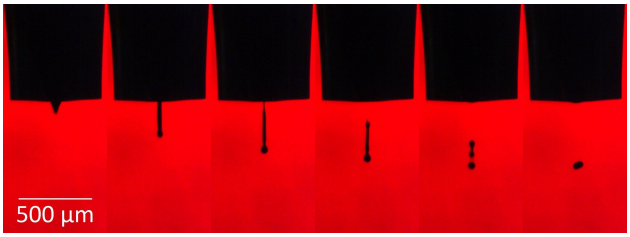

Figure 4.1. Drop formation of the Metalon silver nanoparticle ink at 40 V, 1100 Hz as imaged from a side mounted camera (Edmund Optics, EO-1312 Color) with telecentric lens (3x, 110 mm WD).

which promotes adhesion. In addition, the wicking ability of the substrate eliminated the need for thermal curing, as it removed the solvent immediately after printing. The samples were printed with a firing voltage of 35-55 V and a firing frequency of 1-1.2 kHz. The voltage, pulsewidth, and firing frequency were tuned until optimal firing settings were found through sideview imaging, see Figure 4.1, wherein drops with compact tails and limited satellites droplets was desired. The droplet volume was approximately 90 pL. Samples were fabricated with a single layer of printed material, approximately 80-100 μm thick as observed with a 3D Optical Profiler (Zeta Instruments, 10x lens). The stage printed the samples row-by-row from left to right with a forward speed of 2 mm/s and a reverse speed of 8 mm/s. After printing, the samples were allowed to cure at room temperature for 24 hr.

Bridge wires, Figure 4.2(a), were printed with three different wire lengths, nominally 1.08 mm, 1.62 mm, and 2.16 mm. Spark gaps, Figure 4.2(b), were fabricated with three different gap widths: nominally 0.5 mm, 0.85 mm, and 1.7 mm.

Select samples were functionalized with energetic material to test the effectiveness of the device as an igniter. For the spark gaps, copper (II) oxide nanoparticles (Sigma Aldrich, 50 nm) and aluminum nanoparticles (NovaCentrix, 80 nm, 82% active aluminum) were suspended in dimethylformamide (DMF) with polyvinylpyrrolidone (PVP) to achieve an 8% solids loading. For the bridge wires, bismuth (III) oxide nanoparticles (Nanophase Technologies Corporation, 38 nm) and the aluminum nanoparticles were suspended in DMF with Solsperse to achieve an 8% solids loading. Either mixture was then mixed with an acoustical mixer (LabRAM) for 16 min. The material was printed with a 500 μm piezoelectrically-

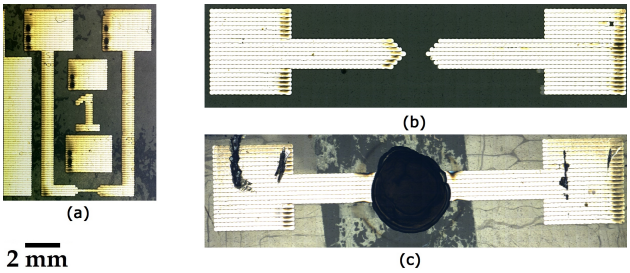

Figure 4.2. (a) A bridge wire and (b) a 0.85 mm spark gap both printed with a single layer of an aqueous dispersion of silver on a flexible, mesoporous medium using a MicroFab piezoelectric inkjet printer. (c) Nanothermite printed on a spark gap, covering both electrodes, with a BioFluidix piezoelectrically actuated pipette.

actuated pipette (BioFluidix, PipeJet P9). The material was printed using the aforementioned dual-axis linear positioning stage such that nanothermite was deposited directly on the spark gap or bridge wire, see Figure 4.2(c).

4.2.2 Sample Testing

To test the bridge wires, a custom circuit was designed and fabricated to pulse power through the device. The functional schematic of the circuit is shown in Figure 4.3. [Note that the decoupling capacitors, integrated circuit (IC) power supply connections, and a trigger conditioning circuit (two series inverting Schmitt trigger stages) have been omitted from the figure for clarity]. A function generator (Agilent 33210A) was used to produce a logic-level (3.3 V logic high, 0 V logic low) pulse with a duration of 10 ms. This voltage pulse drove a gate driver (Fairchild Semiconductor FAN3180, peak source and sink current of 2.5 A) integrated circuit, which in turn drove the base of a high-current N-channel MOSFET (International Rectifier IRFR2405). The gate driver was critical for turning the MOSFET quickly. The output rise time of the MOSFET was measured with an oscilloscope to be less than 1 μs. The MOSFET had its source connected to ground and a drain connected to the low side of the test device. The test device was incorporated into the circuit by sliding the printed contacts into a gap containing spring contacts for the pulse circuit. A

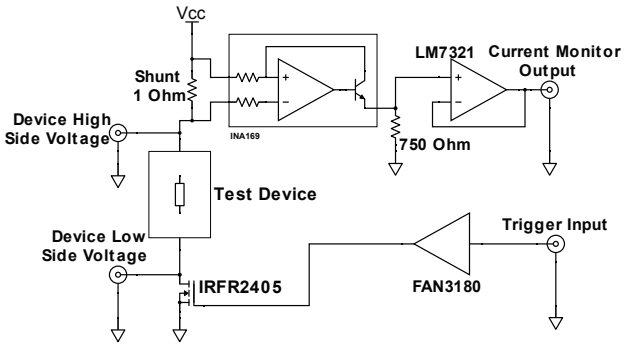

Figure 4.3. A schematic of the test circuit used for bridge wire characterization.

shunt resistor array (eight 8 Ω resistors in parallel) with a total parallel resistance of 1 Ω was connected in series between the power supply and the device under test. A Texas Instruments INA169 high-side measurement current shunt monitor IC was connected across the resistor array, and a 750 Ω load resistor on the current shunt monitor output produced a measurement gain of 0.75 V/A. Estimated from the manufacturer datasheet, the current measurement bandwidth at this gain should be higher than 1 MHz. A Texas Instruments LM7321 operational amplifier served as a unity gain output buffer to the DAQ system. The power supply could be driven from a minimum input of 5 V to a maximum input voltage of 18 V, due to the power supply being shared between all of the ICs, with the limiting device being the FAN3180 gate driver.

Four signals were measured simultaneously by an Agilent DS6014A 100 MHz bandwidth oscilloscope: (i) the function generator pulse signal, (ii) the high-side current shunt monitor output V_I, (iii) the test bridge wire high-side voltage V_H, and (iv) the test bridge wire low-side voltage V_L. These channels were all recorded using a single-shot measurement triggered on the pulse and configured to have a sub-microsecond sampling period, with the voltage ranges of the individual channels configured to maximize the dynamic range of the signal relative to the input voltage range without saturating the input. The data was saved as a time series for each initiation event, and the instantaneous differential device voltage $V_d = V_H - V_L$ was computed, as well as the instantaneous current $I_d = 0.75 V_I$. The instantaneous power was computed as $P_d = V_d I_d$ and plotted as a time series. The effect of the input power on the

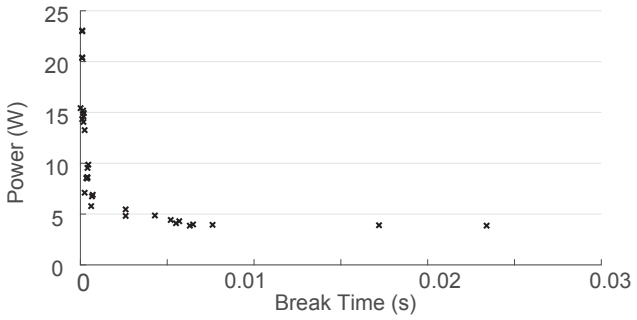

Figure 4.4. The average power through the 1 mm bridge wire compared to the failure time.

failure of the bridge wire was determined by varying the input voltage from 7.5 V to 13.75 V in increments of 1.25 V (Power Source: Agilent E3634A).

The spark gaps were tested with a high voltage power supply (Stanford Research Systems, PS365) with the voltage and current maximums set at 5.2 kV and 50 μA respectively. The power supply was connected to the samples at the square pads using flat alligator clips. The power supply was connected to an oscilloscope to monitor the maximum voltage and current required for spark-over. To test the samples, the voltage output on the power supply was slowly ramped until spark-over occurred, or the voltage maximum was reached. This test was repeated for samples of varying gap widths.

4.3 Results

4.3.1 Electrical Characterization

Bridge wires

The voltage, current, and time needed to break a bridge wire for the three lengths tested are shown in Table 4.1.

The time to failure of the bridge wires with a length of 1 mm is presented in Figure 4.4, wherein the input power was varied and the corresponding failure time was determined.

Table 4.1.
The effects of bridge wire length on failure.

Length (mm)	1.08	1.62	2.16
Average Failure Time (ms)	1.63	1.09	1.10
Failure Range (ms)	(0.55, 4.7)	(0.79, 2.1)	(0.80, 1.4)
Voltage (V)	6.36±0.5	6.68±0.3	6.55±0.2
Current (A)	1.21±0.4	0.97±0.2	1.09±0.1
Resistance (Ω)	5.54±2.8	7.04±1.6	6.01±0.7
Power (W)	7.62±2.0	6.44±1.0	7.16±0.5
Samples	5	7	6

The resistance of the whole bridge wire circuit was calculated using the obtained current and voltage data and was found to be between 4.3 and 9.1 Ω. Resistivity, ρ, was found using $\rho = RA/l$ where the resistance, R, area, A, and length, l, are as reported. The average resistivity was 26 $\mu\Omega$·cm. When compared to the bulk resistivity of silver, 1.59 $\mu\Omega$·cm, this method does not appear promising. However, upon comparison with other printed silver electronics, the performance of the samples described herein is acceptable. It has been reported that printed silver can have resistivities ranging from 12 to 150 $\mu\Omega$·cm based on the substrate, thermal curing, and geometric consistencies of the material [88–90]. This work is on the low end of the reported range, even in the absence of thermal curing, and as such, it is claimed that the printed performance of these devices is on par with that of other printing approaches.

Spark gaps

The voltages required for spark-over for all of the spark gaps tested, without deposited energetic material, are reported in Figure 4.5. 30 of the 31 samples tested successfully sparked below the 5.2 kV maximum voltage threshold. Previous modeling had been conducted for the breakdown in air with sub-millimeter electrode gaps [91] and gap widths in the millimeter to centimeter range [92]. The estimates for breakdown voltages for flat or large radii spherical electrodes and sharp, needle-like electrodes in air are given by given by $V = 3pd + 1.3\sqrt{d}$ and $V = pd + 0.7$ respectively, where d represents the gap width (mm), p represents the atmospheric pressure (atm), and V is the breakdown voltage (kV) [92]. The importance of the electrode geometry is due to the localization of the energy at the electrode tip. It is theorized that an electrode with a small point will require a smaller voltage to spark-over due to the localization of the charge. The validity of these approximations is very sensitive to the environment in which a spark gap is tested; these effects have been investigated thoroughly [93]. The expected spark-over voltages for each gap width tested in this work when modeled as a needle-like or sphere-like electrode are included in Table 4.2.

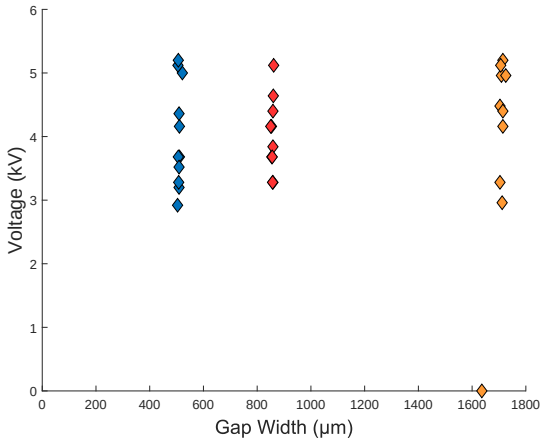

Figure 4.5. The voltage required for a spark discharge across the three different spark gap widths. 30 of 31 samples exhibited a spark-over behavior.

Table 4.2.
The estimated breakdown voltage for three spark gap widths in air for needle- and sphere-like electrodes. The approximations begin to break down for gap widths below 1 mm because gaseous and surface discharge begin to play a role [92].

Gap Width	Needle-like Electrodes	Sphere-like Electrodes
0.5 mm	1.2 kV	2.42 kV
0.85 mm	1.55 kV	3.75 kV
1.7 mm	2.4 kV	6.79 kV

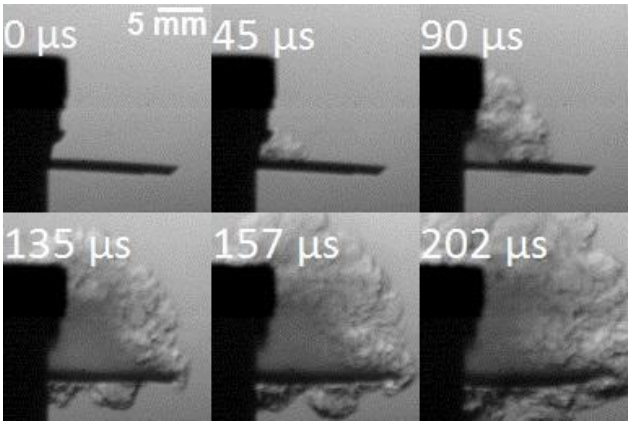

Figure 4.6. High-speed video schlieren images of the ignition of aluminum and bismuth (III) oxide nanothermite obtained with a printed igniter excited at 13.75 V using the test circuit detailed in Figure 4.3. The observed failure time was 70 μs.

4.3.2 Igniter Testing with Energetic Material

To demonstrate the effectiveness of the bridge wires as igniters for energetic material, samples with a 1 mm bridge wire length were functionalized with printed nanothermite: aluminum bismuth (III) oxide. The ignition was captured with a high-speed camera (Phantom v7.0, 20,000 fps), as seen in Figure 4.6. The input voltage for these tests was set to 13.75 V, which is the highest voltage tested. Successful ignition of the nanothermite was observed. Due to the support system and the flexible nature of the substrate, the ignition caused the observed bending of the substrate.

The spark gaps were subsequently tested with deposited nanothermite, in this case, aluminum copper (II) oxide. The nanothermite ignited for 7 of 10 samples tested with the current and voltage limits at 75 μA and 5.2 kV respectively. Figure 4.7 demonstrates the ignition of the deposited energetic material with the printed spark gap. In Figure 4.7(b), the spark jumps over the energetic material between the two electrodes. In the second high speed video frame, Figure 4.7(c), the printed energetic ignites at the two nodes of the spark gap. The final frame, Figure 4.7(d), shows a single flame from the union of the two initial ignition points.

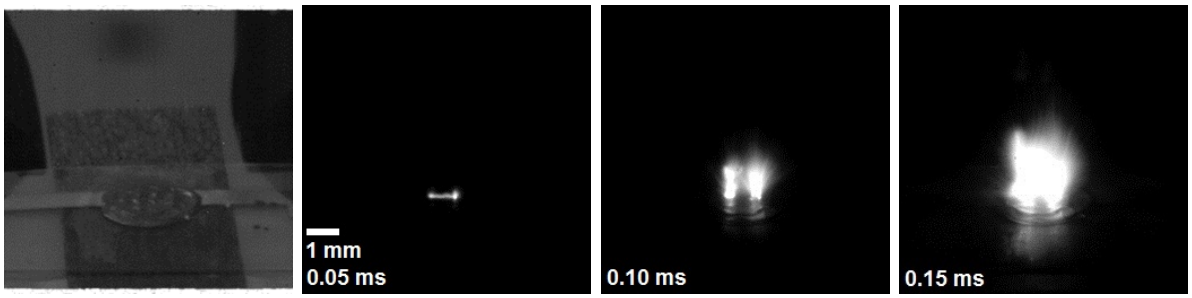

Figure 4.7. (a) Unreacted nanothermite printed on a spark gap. (b)-(d) High-speed video images of the ignition of the printed nanothermite with a printed spark gap.

4.4 Discussion

The manufacturing technique described in this work has provided a solution to fabricate metallic initiators on flexible substrates. They can be directly functionalized with energetic material due to the lack of thermal curing required in the fabrication process. This offers inherent benefits when compared to the traditional inkjet printing of metals, which requires high temperature sintering. As such, both the spark gaps and bridge wires fabricated in this manner can be part of a fully printed solution with deposited energetic material to rapidly fabricate precise igniters.

For the spark gaps, it was found that the width of the gap is a critical design factor due to its correlation with spark-over voltage. In addition, the shape of the printed electrode is critical for accurately predicting the spark-over voltage; the voltage needed decreases with the sharpness of the electrode point. Arguably, the variability of the voltage data for a single gap width in this work can be attributed, in part, to the slight variations in the printed electrode shape.

On the other hand, the key criterion for the bridge wires was the consistency of the deposited material to produce low resistance devices. The resistance of the device was highly correlated to the precision of the geometric features and sufficient solvent evaporation. Due to the nature of the inkjet process, there was wide variability in the resistance of the various bridge wires, and thus the power required for failure. The manufacturing defects can be worked around if the voltage delivered by the power source in these devices is higher than the expected threshold of the lower quality bridge wires produced. Further work fine tuning the fabrication process and defining a narrower input power range is critical before the bridge wires can be reliably implemented.

The spark gaps developed were effective mechanisms for the ignition of energetic material. The limitation to these mechanisms, however, was the miniaturization of the high voltage power source and the environment's influence on breakdown voltage. Overcoming these obstacles with efficient packaging could prove nontrivial. However, in applications where space or power are not limiting factors, these devices would be advantageous.

When compared to each other, spark gaps and bridge wires offer complementary but unique benefits. Both devices can be fabricated relatively quickly with high precision through the use of inkjet printing. As such, they can be functionalized directly with energetic material in the fabrication process. Bridge wires require low voltages, and as such, can be easily miniaturized. However, the spark gaps' large voltage requirement could make packaging the device non-trivial. The uniqueness of these igniters ultimately lie in the energetic material that they can be implemented with. Bridge wires work better with an energetic material that is shock or heat sensitive, while spark gaps are more effective with energetic materials that are sensitive to electrostatic discharge.

Both spark gaps and bridge wires were successful in igniting energetic material. They can be developed into fully printed igniters, however, there is more work to be done with regard to their reliability. In addition, it is imperative that the sensitivity to accidental ignition be studied with these devices before their true feasibility can be assessed.

4.5 Conclusions

In this work spark gaps and bridge wires were fabricated with inkjet printing as a means to develop ignition systems for energetic material. The spark gaps offer an effective ignition mechanism for energetic material that is sensitive to electrostatic discharge. It is acknowledged that fine tuning the performance of the system would be essential for implementation and enhancing the reliability. On the other hand, the bridge wires tested here proved to be most sensitive to the power input. A correlation between input power and failure time for the bridge wires was developed. The devices in this study have proven effective for the ignition of nanothermite. The work described herein is intended as a demonstration of the fabrication process and a comparison of the ignition mechanisms. The repeatability of a single device was not investigated because both the spark gaps and bridge wires were designed to be single use igniters. However, future studies on reliability and manufacturing controls are required.

5. RESONANT MASS SENSORS FOR THE DETECTION OF TRAUMATIC BRAIN INJURY BIOMARKERS

The following chapter is reprinted, in part, from M. Wadas *et al.* "Detection of Traumatic Brain Injury Protein Biomarkers with Resonant Microsystems," which appeared in *IEEE Sensors Letters* [94].

5.1 Introduction

Piezoelectrically transduced resonant microsystems have recently emerged as a promising medical diagnostic tool. Their high sensitivities make them excellent candidates for the mass-based detection of the biomarkers associated with certain diseases and medical conditions [40–43]. The mechanism for detection of the current work relies on the relationship between the mass and resonant frequency of a lumped-mass system,

$$\omega^2 = \frac{K}{m} \tag{5.1}$$

where ω is the resonant frequency, K is the effective spring constant, and m is the effect mass associated with the vibration mode of interest. The mass added to the resonator as a result of the adsorption of a biomarker, Δm, can then be approximated as

$$\Delta m = K\left(\frac{1}{\omega_1^2} - \frac{1}{\omega_2^2}\right) \tag{5.2}$$

where ω_1 and ω_2 are the resonant frequencies of the resonator before and after the adsorption of the biomarker, respectively. This relationship implies that a change in the mass on the surface of a resonator caused by the binding of a biomarker will induce a resonant frequency shift. Furthermore, the sensitivity of the resonator increases as the resonant frequency increases, making high-frequency resonators excellent candidates for biomarker detection. If the surface of such a resonator can be functionalized to allow for the specific adsorption of a biomarker of interest, the binding of that biomarker will cause a change in mass that is

detectable via frequency response analysis. This technique was employed by Fischer et al. in 2008 to detect the presence of streptavidin [95], by Varshney et al. in the same year to detect prion proteins [96], and by Hanay et al. in 2012 to demonstrate single-molecule mass spectrometry in real time [97]. Additional examples of prior work can be found in reviews by Chen [40] and Ziegler [41].

While the most dependable methods of identifying biomarkers rely on immunoassay techniques like the popular enzyme-linked immunosorbent assay (ELISA) test, these methods are cumbersome and involve multiple, time-consuming steps that severely limit their utility for on-site diagnosis [98]. Specifically, ELISA tests require sample, detector antibody, and labeling reagent incubation processes and multiple washing steps that require anywhere from 3 to 8 hr. Mechanical, label-free sensing techniques therefore have a unique niche because they provide portable, high-sensitivity sensing in a fraction of the time [40].

The biomarker of interest for the current work is s100β, a protein closely associated with Traumatic Brain Injury (TBI). The concentrations of s100β in the cerebrospinal fluid of TBI victims immediately after injury typically increase from several ng/ml to several hundreds of ng/ml, making it a promising diagnostic biomarker for TBI [99]. This research leverages recent advancements in mechanical, label-free sensing procedures to demonstrate the successful detection of s100β utilizing a simple, yet powerful, sensor functionalization technique. The work contributes to the aforementioned advancements in label-free sensing and the development of medical tools for TBI diagnosis. The following sections include a description of the methods followed to functionalize the resonators, a description of the experimental procedure, a presentation of results, and a discussion of key implications, areas for improvement, and conclusions.

5.2 Methods

Plate-style, 16 MHz quartz crystal resonators (Kyocera Corp., CX3225) act as the sensors. A single resonator measures 3.20 mm by 2.50 mm and can be seen in Figure 5.1(a). Each sensor was integrated with a circuit that enables its frequency response characterization via an HF2LI Lock-In Amplifier (Zurich Instruments). The characterization was achieved with

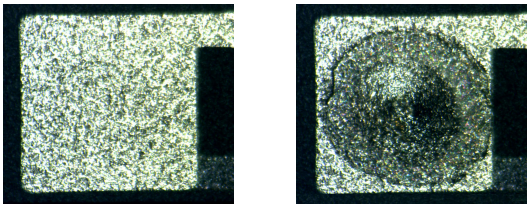

Figure 5.1. (left) A close up view of a 16 MHz plate-style resonator prior to functionalization. (right) The same resonator after functionalization.

1 Hz resolution over a 300 Hz frequency range containing the sensor's resonant frequency. From the frequency response, the peak frequency was taken to be the frequency that yields the highest magnitude output. Any shift in the peak frequency was assumed to be equivalent to a corresponding shift in the resonant frequency, an approximation supported by the high Q-factor of the resonators. A shift in the peak frequency therefore indicated an increase in mass on the surface of the resonator, thus enabling the detection of s100β.

To functionalize the sensors, polystyrene and anti-s100β (Abcam, 100 µL) were suspended in dimethylformamide (DMF) to create a solution of 1.3 mg/mL polystyrene and 0.106 mg/mL anti-s100β in DMF. A piezoelectrically actuated pipette system (BioFluidix) was used to deposit 5.0 nL of this solution onto each sensor, as shown in Figure 5.2. A close up view of a sensor after the solution was deposited is shown in Figure 5.1(b).

The DMF was subsequently allowed to evaporate over a period of approximately 3 hr. This resulted in functionalized sensors with a polystyrene/anti-s100β coating that allowed for the adsorption of s100β. Polystyrene was chosen as a coating due to its relatively low damping on the frequency response of the resonators as compared to other polymers [100]. Anti-s100β was chosen to functionalize the sensors because of its high degree of specificity and affinity for s100β [101]. DMF was chosen as the solvent because of its high evaporation rate and its ability to dissolve polystyrene without denaturing anti-s100β.

Confocal imaging was performed to confirm that the surface of the functionalized sensors would promote the adsorption of s100β. A functionalized sensor was exposed via micropipette to a solution of phosphate buffered saline (PBS) (Abcam) and a fluorescent conjugation of s100β containing a dye known as Alexa Fluor® (Abcam, 100 µL). The exposed

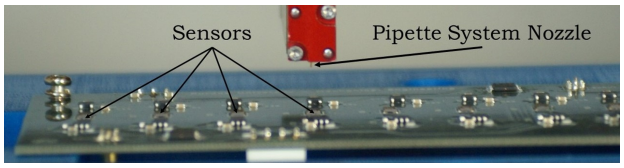

Figure 5.2. The piezoelectrically actuated pipette system. A 200 µm diameter nozzle was used to deposit 5.0 nL of anti-s100β and polystyrene in DMF onto the surface of each sensor.

resonator was subsequently imaged with a confocal microscope to confirm the success of the functionalization. A 20X air lens was used with a pinhole size of 18.01 AU, a laser intensity of 2 %, a gain of 750, and a 1.58 µs pixel dwell time. The fluorescent images taken confirmed the adsorption of the Alexa Fluor® onto the surface of the resonator, validating the functionalization technique.

Forty seven sensors were functionalized as described. After functionalization, the frequency response of each sensor was obtained using the aforementioned experimental setup. An experimental group of 28 sensors was then exposed to 5.0 nL of a 19.6 µg/mL solution of s100β (Abcam, 500 µg) in PBS deposited directly onto the surface of the sensor using the piezoelectrically actuated pipette system. A control group of 19 separate sensors was exposed to 5.0 nL of PBS in the same manner. All of the sensors were subsequently rinsed with 5.0 nL of deionized water deposited onto each resonator again using the piezoelectrically actuated pipette system. After drying over a period of approximately 3 hr, the frequency response of each sensor was again obtained.

5.3 Results

The variable of interest in the experiment is the relative shift in resonant frequency between the experimental group and the control group. An example of this shift is shown in Figure 5.3.

The resonant frequency shift of the sensor represented in Figure 5.3 after exposure to s100β was 23,244 Hz. The resonant frequency shifts of all of the sensors tested are presented in Figure 5.4.

The average frequency shift among the 28 resonators in the experimental group was 13,704 Hz with a standard deviation of 6,259 Hz. The average frequency shift among the 19 resonators in the control group was 1,504 Hz with a standard deviation of 11,431 Hz. Therefore, the average difference in the frequency shift between the experimental and control groups was 12,200 Hz.

A one-sided, two-sample t-test was performed challenging the null hypothesis that the frequency shift experienced by the experimental group is equal to the frequency shift of the

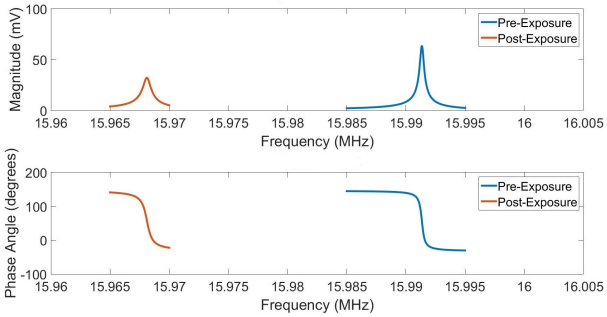

Figure 5.3. The frequency response of a 16 MHz resonator driven by a 200 mV amplitude signal both before and after exposure to a solution of PBS containing s100β. The shift of the resonant frequency is caused by the adsorption of s100β onto the sensor's surface.

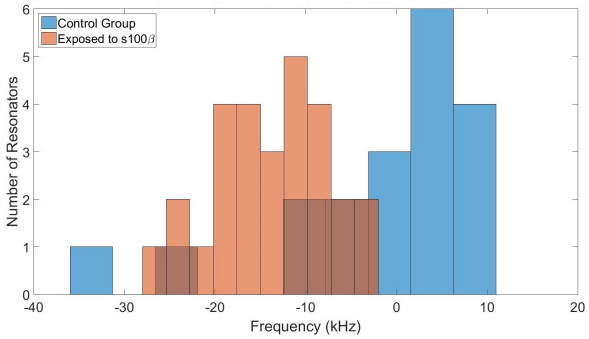

Figure 5.4. The resulting frequency shifts of the 28 sensors in the experimental group that were exposed to PBS and s100β and the 19 sensors in the control group that were exposed to PBS only.

control group. The alternative hypothesis states that the average frequency shift experienced by the sensors in the experimental group is greater than the average frequency shift of the sensors in the control group. A small significance level of $\alpha = 0.001$ was chosen in order to minimize the risk of a Type I error. The resulting probability value was $p = 0.000012$. Therefore the null hypothesis was rejected and the experiment provides strong statistical evidence of the successful detection of s100β.

The total amount of s100β deposited onto the sensors in the experimental group, determined by multiplying the concentration of s100β in the exposure solution by the volume deposited, was approximately 98 pg. This corresponds to an overall sensor sensitivity of 124.49 Hz/pg. This is theoretically sufficient to enable the detection of s100β in victims of TBI, who typically have s100β concentrations on the order of hundreds of ng/ml in their cerebrospinal fluid [99].

5.4 Discussion

On average, the sensors exposed to s100β experienced a resonant frequency shift 12,200 Hz greater than the sensors exposed to PBS only. The experiment thus provides strong evidence that s100β was successfully detected ($p = 0.000012$). It should be noted, however, that despite the statistical significance, there was still a large amount of overlap between the two groups of sensors. This overlap can be explained by a number of factors including the variation in the nominal resonant frequency of the resonators, the variation in the volume of the solution deposited onto the sensors during the functionalization procedure and the s100β exposure procedure, and the spatially dependent mass sensitivity of the resonators. This limits the ability of a single sensor to provide conclusive evidence of the successful detection of the biomarker. As in this experiment, an array of sensors can be used to generate sample statistics to provide conclusive results.

The detection of biomarkers in their native biological fluids is of interest among the research community. This endeavor is complicated by the damping effect of the fluid on the frequency response of the resonators. This obstacle was circumvented in this experiment by allowing the sensors to dry after exposure and rinsing. While sensing in fluids may be

necessary to enable continuous health monitoring applications, the dry sensing techniques utilized in this experiment may be more advantageous for single-use, portable diagnostic applications, akin to the on-site diagnosis of TBI. While the sensors were allowed to dry for approximately 3 hr, prior work not included in this report indicates that a minimum drying time of only 20 min was required.

Another advantage offered by the technique presented is the small volume of fluid (5.0 nL) required for deposition onto the sensors. This is particularly beneficial for TBI diagnosis given the medical difficulties associated with lumbar puncture, otherwise known as a spinal tap, and collecting large amounts of cerebrospinal fluid [102].

It should be noted that an issue was encountered involving a loss of the polystyrene and anti-s100β functional coating on the surface of several sensors in both the experimental and control groups during the rinsing step. This caused an increase in the resonant frequency of those sensors due to the lost mass associated to the coating. The statistical effect of this functional coating loss was reduced in this experiment through the use of multiple sensors and by tracking the relative difference in resonant frequency shift of both groups as the variable of interest. This functional coating loss may have also had an effect on the measured Q factors of the resonators. The average measured Q factors for the native, functionalized, and s100β-exposed resonators were 79,182, 18,786, and 21,248, respectively. The decrease in average Q factor between the native and functionalized resonators is explained by the increased damping from the functional coating. The additional mass of the s100β should further decrease the Q factor between the functionalized and s100β-exposed sensors, but a slight increase was observed instead. Further improvements could be made by incorporating a method for ensuring the strong adherence of the polystyrene/anti-s100β coating to the surface of the sensor, such as surface etching the resonator prior to functionalization. This technique was utilized by Fischer et al. to create nanostructures on the surface of silicon resonators to facilitate the binding of a polymer/biotin functional coating used to detect streptavidin [95].

Finally, the resonator functionalization was at times limited due to the high wetting of DMF on quartz, a non-porous substrate. This sometimes caused the coating solution to spread out past the edge of the resonator. When this happened, binding sites for the s100β

may have been lost, as not all of the anti-s100β settled onto the piezoelectrically active area of the resonator. This may also partially explain the large variance of the experimental data, as some of the sensors may have randomly had a greater potential to bind s100β than others. While the statistical effect of this issue was minimized through the use of a large number of resonators (47 total), future experiments may utilize gold-plated resonators, which cause the coating solution to bead onto the surface rather than spread, or a solvent with a greater surface tension than DMF. This would prevent the coating solution from escaping the boundaries of the piezoelectrically active area of the resonator.

5.5 Conclusions

A novel functionalization technique utilizing a piezoelectrically actuated pipette system to deposit a functional coating solution of polystyrene and anti-s100β in DMF onto the surface of piezoelectric resonators was presented. An experiment was then performed with the functionalized sensors attempting to detect the presence of s100β, a protein biomarker used for diagnosing TBI. Statistical analysis of the experimental results yielded strong evidence of the successful detection of s100β with sensitivities that theoretically enable the diagnosis of TBI. The detection of s100β and the feasibility of rapid TBI diagnostics via mechanical resonators have thus been demonstrated. The novelties of this technique include the small biological sample volume required, the decreased assay time, and the improved portability compared to conventional methods.

6. ADDRESSING THE PREDICTIVE CAPABILITIES OF VOLATILE ORGANIC COMPOUND SENSORS

6.1 Introduction

As society spends more time indoors, the exposure to volatile organic compounds (VOCs) released by building materials, coatings, colorants, and amongst other common sources becomes more prevalent. VOCs are chemicals with high vapor pressures at room temperature and are often detrimental to human health [103]. As regulations and safety concerns increase, the need for reliable, sensitive, and selective VOC sensors is pressing. Lab-based sensing advancements have shown promise for VOC detection [52, 53, 55]. However, most of these technologies struggle to span the valley of death associated with transforming research successes to market-ready products. A major factor in this lack of technology transfer is the difference between bench-top detection claims and predictions of species concentrations in realistic environments. Extensive work has been done to develop portable VOC sensors with detection limits in the low parts-per-million to hundreds of parts-per-billion range [55, 104, 105]. However, there has been comparatively little work extrapolating the concentration of a specific analyte directly from the sensor's voltage or frequency output [52, 53]. For practical implementation, sensing platforms should be designed to maximize predictive capabilities without compromising detection limits [56–58].

There has been extensive research on metal-oxide chemiresistive VOC sensors with parts-per-million sensitivity [104]. These resistive sensors require high operational temperatures, and thus appreciable power budgets. This results in cumbersome and/or costly sensor integration. Additionally, reviews of the subject have concluded there exists a need for a more selective, not just sensitive, approach when identifying specific analytes of interest [104]. Electronic-nose arrays are capable of identifying analytes through large data set processing, but require an appreciable number of sensors to gain information [54, 106]. Furthermore, these sensor networks typically lack quantitative information regarding analyte concentra-

tion and are unable to identify individual chemical gas components [54, 55]. To practically implement selective VOC sensors, low-cost platforms with reliable predictive capabilities are needed.

This work utilized a multi-channel oscillator-based sensing array with a frequency counting algorithm to address the aforementioned limitations in current sensing capabilities. Oscillators have previously been used as the sensing element in mass detection across various applications to achieve sensitive detection at a low cost [47–50]. In this work, a field programmable gate array (FPGA) based frequency counter was used to simultaneously monitor of 16 sensing channels in parallel. Previous work has leveraged frequency counting to monitor the oscillation frequency of mass sensors [107]. Similarly, shifts in the resonance frequency of MEMS resonators and quartz crystal microbalances (QCM) have been quantified using frequency counting for the detection of VOCs in power-efficient devices [108, 109].

The oscillators in this work were functionalized via inkjet printing for tailored manufacturing. This allowed for the deposition of multiple materials across a single sensing array. This manufacturing approach has been used with appreciable success in prior work to precisely deposit a functional chemistry onto the sensing element [10–12, 14, 108]. Through inkjet printing, the amount of functional chemistry and the area of functionalization can be tuned to enable high sensitivity without compromising the nature of oscillation by adding too much mass or damping.

By leveraging 16 parallel channels with redundant elements, simultaneous data collection, and 1 s temporal resolution, a non-trivial amount of frequency shift and concentration level data was collected. This approach facilitated the development of a preliminary linear regression model of ambient air concentration with multiple analyte selectivity. The sensing array demonstrated herein can provide a first step towards predicting resonant mass detection limits based off of large data sets. This work also helps assist laboratory sensors in the translation into practical field implementation with similar performance.

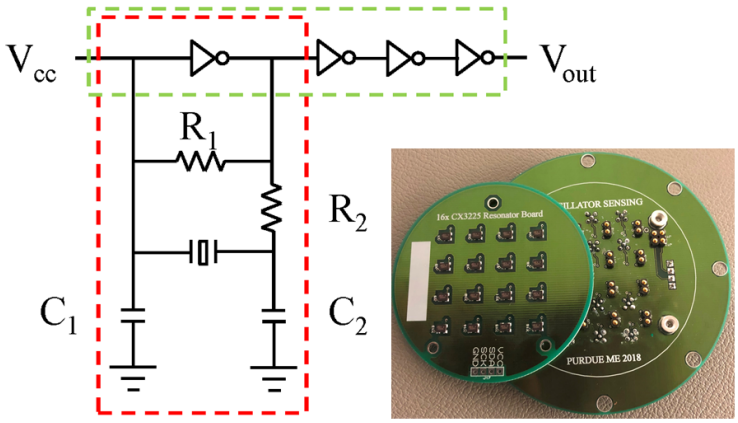

Figure 6.1. A Pierce oscillator circuit with the oscillator (red) and a series of inverters (green) depicted along with the resonator board and instrumentation board offset to show electrical connections.

6.2 Materials and Methods

6.2.1 Sensor Design and Fabrication

A sensor array of 16 Pierce oscillators (see Figure 6.1) was fabricated for this work. Each oscillator consisted of an inverter, two load capacitors, $C_1 = 22$ pF and $C_2 = 22$ pF, one feedback resistor, $R_1 = 2$ MΩ, one isolation resistor, $R_2 = 510$ Ω, and a 16 MHz quartz crystal resonator (Kyocera Corp., CX3225), $C_L = 12$ pF. The crystal oscillator driver, COD (Texas Instruments, SN74LVC1GX04), provided the circuit with the Pierce oscillator inverter, as well as three additional inverters which converted the oscillator output signal to a square wave. The hardware implementation of the oscillator circuit resulted in two printed circuit boards: a board with solely an array of resonators and an instrumentation board containing the remaining elements of the oscillator circuit (see Figure 6.1). The resonator board was secured to the instrumentation board such that spring connection pins provided the necessary electrical coupling to place the resonator within the oscillator circuit. Given this, the resonator boards could be interchanged quickly and without incurring high component costs. The instrumentation board also served as the bottom of the 9.5 cm diameter test chamber.

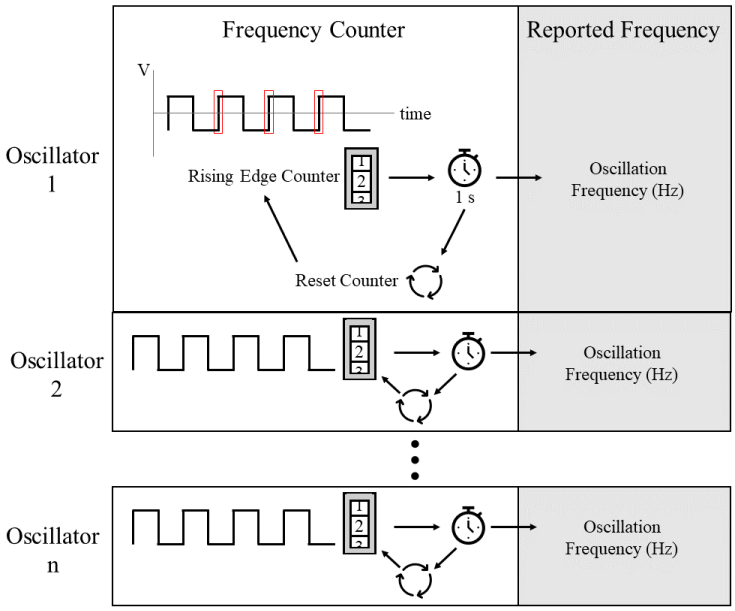

Figure 6.2. A graphical representation of the frequency counting method to accept 16 oscillator outputs and compute the corresponding oscillation frequencies every second with 1 Hz resolution

A frequency counter was implemented to monitor the oscillation frequency of each device in parallel, a schematic of which is shown in Figure 6.2. The instances of the rising edge of the oscillator output voltage were counted. The number of rising edges per second was reported as the oscillation frequency. Because this method required multiple analyses for each cycle of the input signal, the frequency counter loop needed to run significantly faster than 16 MHz, the nominal oscillation frequency of the devices. To achieve the computational speeds required, the frequency counter was synthesized and executed on an NI myRio field-programmable gate array (FPGA) with a 120 MHz internal clock. The FPGA allowed for parallel computing on all 16 channels.

6.2.2 Sensor Functionalization

A BioFluidix PipeJet P9 piezoelectrically actuated pipette with a 200 μm nozzle was used to deposit 5 nL of a functional ink onto each quartz resonator. A machine vision and spatial registration system was implemented with a high-precision linear axis stage (AeroTech

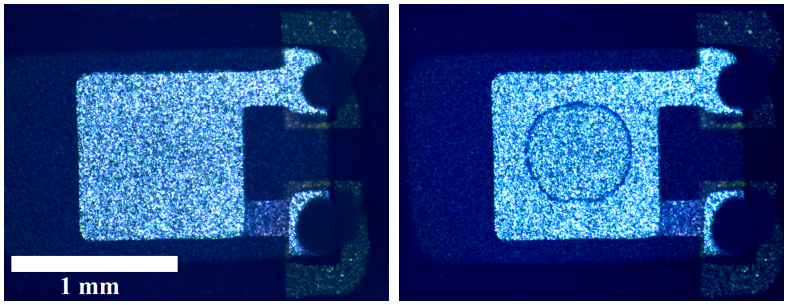

(a) (b)

Figure 6.3. Representative view of a resonator (a) before and (b) after functionalization. Note the center of the resonator is coated with a thin film of poly(4-vinylpyridine).

Table 6.1.
Functional chemistries inkjet printed on the resonators at 5 nL per device. All of the solvents and polymer were sourced from Sigma Aldrich.

Solvent	Polymer	Concentration (mg/mL)
Toluene	Polymethylmethacrylate	1
Toluene	Polystyrene	0.3
Ethanol	Poly(4-vinylpyridine)	1

PlanarDL-200-XY) to deposit the material at the center of the device to maximize sensitivity [14]. A representative image of a resonator before and after functionalization is shown in Figure 6.3. The three polymers detailed in Table 6.1 were chosen as the solutes in this work due to their previously demonstrated sensitivities to volatile organic compounds [110]. The inks were randomly assigned to resonator locations and additional resonators were left unfunctionalized to serve as temperature and humidity references. After functionalization, the resonator board was stored under vacuum for a minimum of 24 hr to remove any remaining solvent.

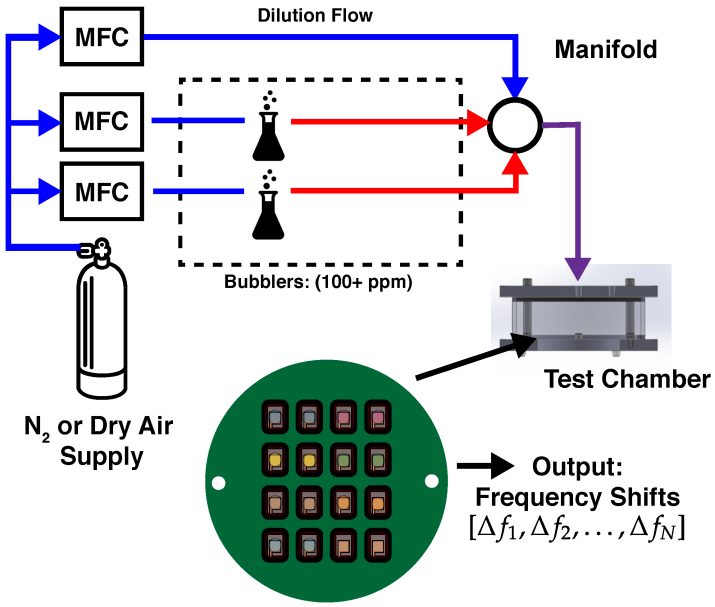

Figure 6.4. Schematic representation of the experimental apparatus used for oscillator-based VOC sensing.

6.2.3 Sensor Testing

Immediately prior to testing, the resonator board was secured to the instrumentation board and the chamber was sealed. The chamber was secured with an inline flow distribution system (see Figure 6.4) to achieve the desired concentrations of the analytes. Nitrogen was connected to three mass flow controllers (MFCs) in parallel. Two of the MFCs (MKS 1480A, 40 ccm) were connected to bubblers (Chemglass, AF-0085) with either 10 mL of methanol or toluene. The other line (MKS 1179A, 500 ccm) remained a pure nitrogen source. The three inlets were connected to a manifold, the output of which was connected directly to the chamber inlet.

The chamber was flushed with pure nitrogen at 150 ccm to create an inert environment, which was used as the baseline for experimentation. Subsequently, the analyte gas was injected into the chamber to achieve the desired concentrations. Concurrently, the oscillation frequencies were recorded every second.

6.3 Results

An array of 16 oscillators was fabricated such that four resonators were left unfunctionalized and three sets of four resonators were functionalized with 5 nL of an ink from Table 6.1. The oscillation frequency recorded as a function of time for each set of devices is shown in Figure 6.5. The data is presented as a shift from the initial oscillation frequency. The stacked color bars represent the makeup of the gas flowing into the chamber at 150 ccm with yellow and purple indicating the concentration of methanol and toluene, respectively. To show the resolution achieved with this approach, a 30 min data subset of a single channel reported in Figure 6.5 is presented in Figure 6.6.

A linear regression model relating frequency shifts and analyte concentration was created. The frequency shift for each oscillator during every analyte exposure event was recorded as the difference in frequency of the oscillator 3 min before and 15 min after the analyte pulse was initiated. Shifts due to methanol and toluene concentrations ranging from 4000 to 14000 ppm were used as a training data set. The set was divided into $n = 4$ subsets according to the functional ink. A linear-regression model of the form:

$$\delta\Omega_1 = a_{1,0} + a_{1,1}M + a_{1,2}T$$

$$\ldots$$

$$\delta\Omega_n = a_{n,0} + a_{n,1}M + a_{n,2}T$$

was developed, where $\delta\Omega_i$ is the frequency shift of an oscillator functionalized with the i_{th} ink, M is the concentration of methanol (ppm), and T is the concentration of toluene (ppm). Additional model terms that were not included due to a lack of predictive significance included resonator location; resonator number; concentration cross terms (e.g., $M * T$); higher-order concentration terms (e.g., M^2); and functional material's position on the resonator. The effect of the aforementioned terms was determined to be negligible through an ANOVA test. The training data set produced four regression equations, a unique equation for each ink in Table 6.1 and an equation for the reference channels. The regression coefficients and the coefficients of determination (R^2) for these four models are presented in Table 6.2.

A new experimental data set with analyte exposure limits within the same range as the training data set was used to test the model. The frequency shifts of the 16 devices were

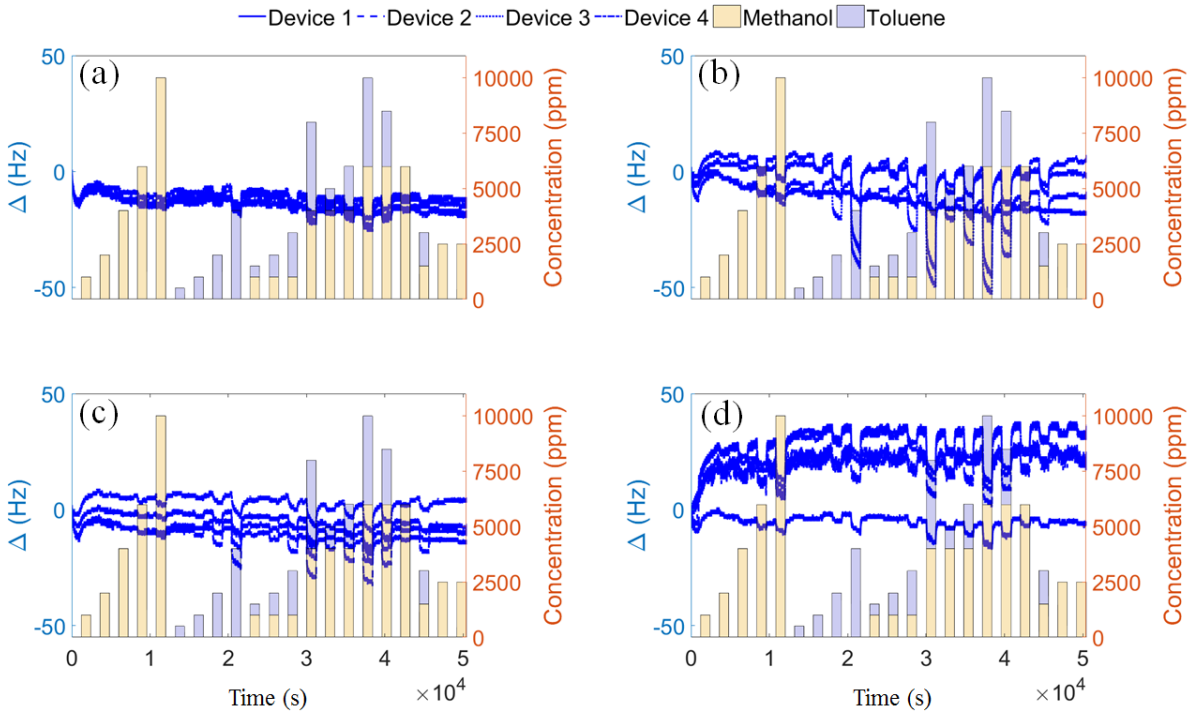

Figure 6.5. The oscillation frequencies of 16 oscillators reported as shifts from the initial frequencies. The devices in (a) were left unfunctionalized as a reference channel and the remaining were functionalized with (b) 1 mg/mL of polymethylmethacrylate in toluene, (c) 0.3 mg/mL of polystyrene in toluene, and (d) 1 mg/mL of poly(4-vinylpyridine) in ethanol. The stacked color bars represent a makeup of the inlet gas at 150 ccm where yellow and purple indicate the methanol and toluene concentrations, respectively.

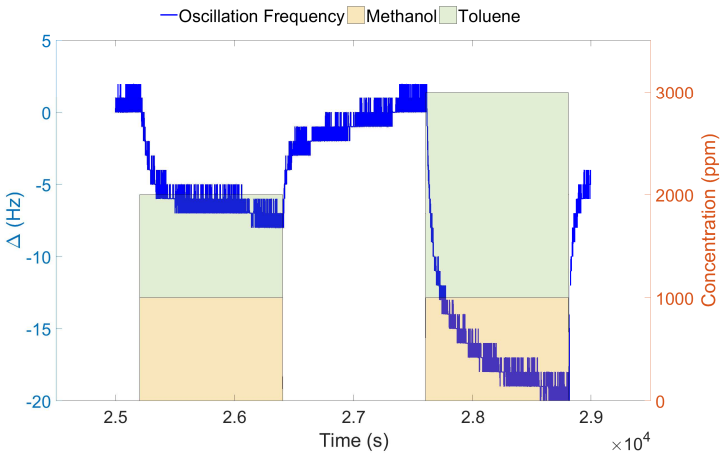

Figure 6.6. A subset of a single channel presented in Figure 6.5 to demonstrate the resolution achievable with the presented sensing method. This device was functionalized with polymethylmethacrylate.

Table 6.2.
Linear regression coefficients and coefficients of determination for each ink grouping where PMMA is polymethylmethacrylate and P4VP is poly(4-vinylpyridine).

Material	Intercept $a_{n,0}$ (Hz)	Methanol $a_{n,1}$ (Hz/ppm)	Toluene $a_{n,2}$ (Hz/ppm)	R^2
Reference	1.5	$-0.4 \cdot 10^{-4}$	$-1.7 \cdot 10^{-3}$	0.98
PMMA	0.3	$-7.2 \cdot 10^{-4}$	$-3.7 \cdot 10^{-3}$	0.48
Polystyrene	2.3	$-5.2 \cdot 10^{-4}$	$-2.9 \cdot 10^{-3}$	0.75
P4VP	0.2	$-13 \cdot 10^{-4}$	$-2.5 \cdot 10^{-3}$	0.87

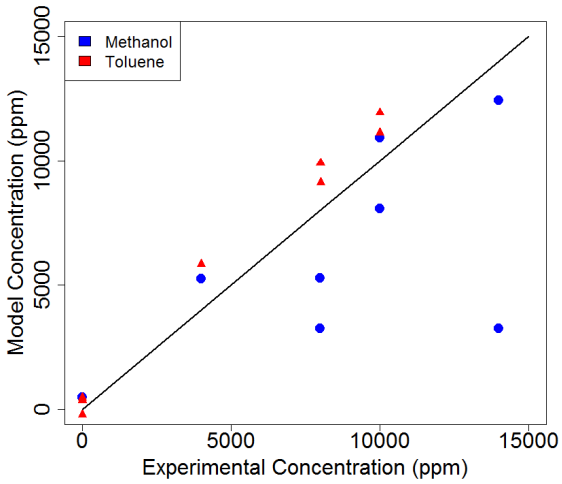

Figure 6.7. The actual concentration of methanol (blue) and toluene (red) plotted against the predicted analyte concentration. An ideal fit would follow the black line.

known and the methanol and toluene concentrations for each pulse were predicted. Due to the over-constrained nature of the data set (i.e. 16 known shifts but only 2 unknown concentrations) a generalized inverse, or least squares, approach was used to invert the coefficient matrix and solve for M and T. To show the accuracy of the model, the experimental concentration was plotted against the predicted concentration in Figure 6.7 with the black line indicating an ideal fit. The methanol and toluene concentrations were predicted with an R^2 of 0.81 and 0.99, respectively. The residuals of the methanol and toluene model are shown in Figure 6.8. These preliminary results suggest a first-step at using redundant training data to predict the analyte concentration based on frequency shifts of functionalized resonators.

6.4 Discussion and Conclusions

It can be seen from Figure 6.5 that the time response of 16 oscillators can be monitored in parallel with this method. This approach generated an appreciable amount of data with 16 parallel channels reporting oscillation frequency once per second. This data provided a real-time picture of the system performance with realistic adsorption and desorption timescales.

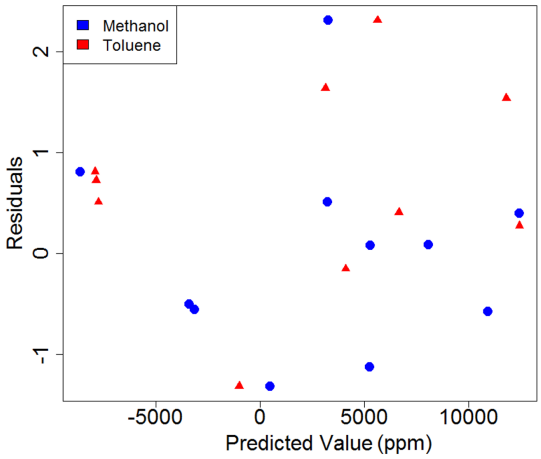

Figure 6.8. The residuals of methanol (blue) and toluene (red) plotted against the predicted analyte concentration.

The data in Figure 6.5 includes an initial drift period of 20 min as the system reached an equilibrium under gas flow and temperature changes. This is of importance as implementation would require sufficient equilibration time. Additionally, Figure 6.6 demonstrated the timescale at which adsorption and desorption occurred in this system. All of the shift data used herein was presented when the system was at steady state, 15 min after the analyte pulse began. When considering practical implementation, the definition of steady state for concentration calculations would need to be defined.

In this work, the shift in oscillation frequency due to the addition of nitrogen, methanol, or toluene is different for each type of functional chemistry. When grouped by the functional ink, a one-way ANOVA test showed statistically significant differences in oscillation frequency shifts due to the addition of methanol, toluene, or a mixture there of. The sensitivity in response to methanol was 2326, 2857, and 833 (ppm/Hz) for PMMA, polystyrene, and P4VP channels, respectively. The sensitivity in response to toluene was 370, 357, and 370 (ppm/Hz) for PMMA, polystyrene and P4VP channels, respectively. The nature of this work was not to develop a more sensitive methanol or toluene sensor but was instead to analyze how predictive capabilities could improved with existing sensors. The key result of these sensitivities is the difference in magnitude between the responses to the analytes of interest. This difference is paramount when identifying candidate functional materials for multi-analyte, multi-channel sensing platforms. Initial ink screening should include identifying functional materials with different responses to the analytes of interest.

A key component in creating an effective sensor model lies in the training data and model terms chosen. Possible additional model terms such as higher order or cross terms, as detailed in the results section, were included in original versions of the regression model. However, when tested they were not significant ($\alpha = 0.01$) predictors of frequency shift due to concentration changes. By choosing to include fewer terms in the model, the degrees of freedom increased. This allowed for more confidence in the detection claims.

The nature of this system of linear regression equations resulted in decisions regarding which equations should be included when performing the generalized inverse to determine the chamber concentration. It was found that to predict methanol concentrations, the data from channels functionalized with poly(4-vinylpyridine) was critical. If these channels were

ignored the R^2 for the methanol concentration did not exceed 0.44 in any other combination of model equations. If that data was used alone, the methanol concentration was predicted with an R^2 of 0.30. However, if that data was used with any of the remaining channels' information, or pairs thereof, the R^2 increased to 0.80-0.84 with the reference channel and poly(4-vinylpyridine) combination producing the highest R^2. This implies that the poly(4-vinylpyridine) was an effective predictor of methanol concentration but required an additional channel to assist in discerning the difference between toluene and methanol in the chamber. This can be seen most clearly from the linear-regression coefficients in Table 6.2. The methanol coefficient for the poly(4-vinylpyridine) equations is an order of magnitude higher than that for the other groupings. This distinction is a driving factor in the significant effect of these channels on predicting the methanol concentration accurately.

When considering the prediction of toluene, any channel type, or combination of channels, resulted in an R^2 greater than or equal to 0.86 with the exception of a model including only polystyrene and polymethylmethacrylate, the two weakest predictors, which resulted in an R^2 of 0.65. This indicates that the functional chemistries chosen were not selective to toluene and thus the response of a bare quartz crystal, the reference channel, was just as significant as the functional channels. This is demonstrated in Table 6.2 in which all of the toluene coefficients are of the same order of magnitude. This result informs the selection of functional chemistries. It is critical to implement functional materials that have significant responses to the analytes of interest and are distinct in their behavior to accurately predict the concentration of several analytes.

Figure 6.5 shows the oscillation frequency of 16 oscillators over time. Each subfigure represents a group of four oscillators with the same functional material. Ideally, these four channels would perform identically. However, it can be seen that the channels have similar qualitative trends but have significant quantitative spread in their data. This can be attributed, in part, to the error in droplet placement during functionalization. It was previously found that the devices used were most sensitive at their geometric center [14]. The location of the functional material was included in an iteration of the concentration/shift model; however, it did not prove to be a significant predictor. As such, the material location is not the only element that this spread can be attributed to. It is hypothesized that there is

a non-trivial effect of surface interactions with the various solvents used. Namely, the same volume of deposited material may spread more or less depending on the surface/ink interactions. Additionally, this spread could result in non-uniform film thickness across devices. These added effects represent some of the device-to-device differences.

Due to the apparent spread in frequency shifts within an ink group, it is important to discern if the resonator has a random effect on the shift. To do so, the linear regression model with four ink groupings was expanded to 16 unique resonator equations. The least squares approach was then used to invert the equations and predict the methanol and toluene concentrations based on the same experimental data set. The result did not produce an improved concentration prediction. As such, it was concluded that the random resonator-based effects are not as significant as the ink effects. Moving forward, the ink-based groupings are sufficient to capture behavior with as few model equations as possible.

By implementing an array of oscillators functionalized with inkjet printing, a multi-channel sensing platform was created. The use of an FPGA-based frequency monitoring algorithm allowed for oscillation frequency data to be recorded every second and in parallel on all 16 channels. For practical field implementation, the FPGA approach can be miniaturized and integrated on chip for a fully deployable solution. The sensing platform and approach produced a low-cost, scalable sensing array for multiple analyte monitoring once per second. This allows the system to capture processes with non-trivial time scales. Furthermore, the redundant elements and multiple functional inks resulted in a linear regression model with high correlation coefficients, $R^2 = 0.81$ and $R^2 = 0.99$ for toluene and methanol predictions, respectively. Through the use of least squares analysis, the model was able to be inverted and experimental shifts could be used to predict analyte concentrations. This step is meaningful because it brings the technology a step beyond claiming detection through demonstrated frequency shifts and towards building models to interpret the relationship between these shifts and possible analyte concentrations. Future sensor developments should keep practical sensing considerations in mind when developing platforms so the systems can be scalable and integrate with predictive methods for analyte concentrations.

7. SELECTIVE DETECTION OF AROMATIC HYDROCARBONS USING PIERCE OSCILLATOR SENSORS

The work presented herein was a shared effort in which A. K. Murray was responsible for subsections 7.2.2-7.2.4, and 7.3.2 and J. N. Hodul was responsible for subsections 7.2.1 and 7.3.1. The remainder of Chapter 7 was a shared effort.

7.1 Introduction

While several factors influence public health in interior spaces, a main contributor to long-term deleterious health effects are volatile organic compounds (VOCs) [111–114]. VOCs, such as xylene, toluene, and benzene, have been shown to be toxic even at low concentrations [59, 60]. As a result, these chemicals have been strictly regulated in many countries [115]. This regulation and the associated health hazards have created a need for a variety of VOC sensing platforms [52, 70, 105]. To date VOCs have been primarily detected using photo ionization detectors (PIDs), amperometric detectors, semiconductors (resistive sensors), portable gas chromatographs, electronic noses/sensor arrays, and optical sensors [61–69]. These sensors though capable of VOC detection lack adequate selectivity, durability, energy consumption, cost, performance, and/or humidity stability [52, 70]. Given this, there is a need for simple, low-cost, long-lasting, and efficient indoor sensors for the detection of VOCs that can seamlessly be incorporated into existing buildings for interior monitoring.

Xylene, specifically, is a toxic, colorless, and sweet smelling volatile aromatic hydrocarbon which is emitted by building materials, coatings, colorants, adhesives, solvents, and paints [116, 117]. Xylene has a chemical formula of $C_6H_4(CH_3)_2$ and consists of a six-carbon ring to which two methyl groups are bound. It exists in three isomeric forms: ortho-, meta- and para-xylene. Exposure to xylene has been linked to many deleterious health effects such as nervous system depression (headaches, brain hemorrhages, seizures, and memory

loss), gastrointestinal tract irritation (vomiting), skin irritation (burns and blistering), and even death [117–121]. The permissible exposure limit for xylene given by the Occupational Safety and Health Administration is 100 ppm as an 8 hr time-weighted average (TWA) [122]. Therefore, it is of critical importance to personal safety in interior monitoring that a reliable and cost effective sensing platform, specifically tailored to the selectively of xylene, be integrated into environments where xylene could potentially be present.

Xylene has previously been detected using metal oxide based resistive sensing [123–126]. Though efficient in the selective sensing of xylene, these sensors typically utilize expensive metals such as tin, cobalt, and nickel [52]. Metal oxides also require manipulation to be more selective to xylene versus other aromatic hydrocarbons, such as toluene [127]. Additionally, resistive sensing requires high operational temperatures, $> 200°C$, and thus high energy input [127]. In addition, single ppm detection of p-xylene has been demonstrated with functionalized quartz crystal microbalances (QCM) [128,129]. These QCMs have also shown promise when implemented with frequency counting algorithms in the selective detection of xylene at 2500 ppm [130]. However, QCMs tend to be high cost. Similarly, functionalized resonators have been widely used for aromatic hydrocarbon detection but lack the sampling rate needed for vapor-phase detection [131]. Additionally, the practical implementation of VOC sensors requires redundant sensing channels to adequately achieve the selective sensing of a specific analyte. As such, there exists a need to develop a low-cost, low-power sensor array that has ppm level sensitivity with xylene selectivity and single second temporal resolution.

Previously, hydroxylamine hydrochloride (HHCl) has been used in sensing technology for the sub ppm detection of formaldehyde, releasing HCl gas upon chemical interaction with formaldehyde requiring sensor modifications to adapt to the surface chemistry [132]. In this work, quantitative detection of xylene (100 ppm) using a resonant mass sensor functionalized with HHCl drop cast on single-walled carbon nanotubes (SWCNTs) was shown. These sensors demonstrated the reusable and reliable detection of xylene through both adsorption and desorption pathways. An array of Pierce oscillators implemented with a frequency counting algorithm resulted in simultaneous monitoring of 16 sensors each with a temporal

resolution of 1 s and frequency resolution of 1 Hz. This produced a low-cost, low-power, multi-channel sensing array capable of detecting xylene at 100 ppm.

7.2 Experimental Methods

7.2.1 Material Preparation and Characterization

Raw (HiPCO) SWCNTs, used as received from ChemElectronics Inc. were further purified by exposure to air at 300 °C followed by a concentrated hydrochloric acid (HCl) wash to remove remaining metal catalysts prior to use following a previously reported procedure [133,134]. HHCl was purchased from Sigma Aldrich, stored under inert conditions, and used as received.

To characterize the structural integrity of the SWCNTs before and after the addition of HHCl, a 633 nm He:Ne laser Horiba/Jobin-Yvon LabRAM HR800 confocal microscope Raman Spectrometer setup was implemented. Additionally a Rigaku SmartLab X-ray diffractometer was utilized.

7.2.2 Sensor Configuration

This work utilized an array of 16 Pierce oscillators, Figure 7.1. Each oscillator consisted of an inverter, two load capacitors, C_1 = 22 pF and C_2 = 22 pF, one feedback resistor, R_1 = 2 MΩ, one isolation resistor, R_2 = 510 Ω, and a quartz crystal resonator (Kyocera Corp., CX3225), C_L = 12 pF. The crystal oscillator driver, COD (Texas Instruments, SN74LVC1GX04), provided the circuit with the Pierce oscillator inverter, as well as three additional inverters which converted the oscillator output signal to a square wave. A Field Programmable Gate Array (FPGA) was implemented as a frequency counter to track the oscillation frequency of each oscillator in parallel. This resulted in 16 parallel frequency measurements every second with 1 Hz resolution. To improve experimental efficiency, the 16 resonators were isolated on a disposable resonator board. This was mechanically coupled to an instrumentation board that contained the remaining elements of the oscillator circuitry.

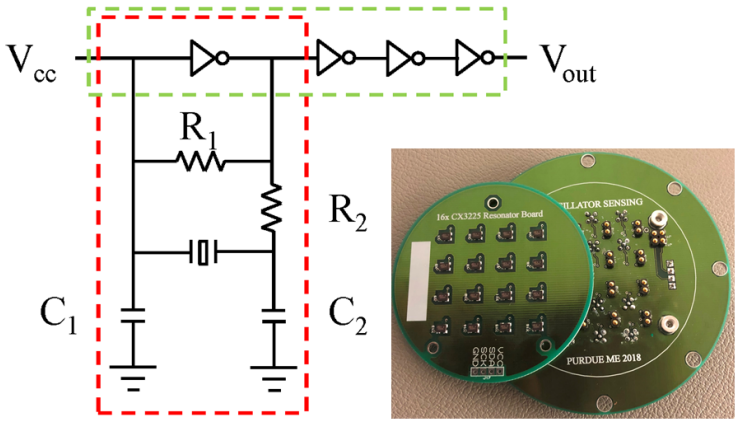

Figure 7.1. A Pierce oscillator circuit with the oscillator (red) and a series of inverters (green) depicted along with the resonator board and instrumentation board offset to show connections.

7.2.3 Device Functionalization

SWCNTs were functionalized with HHCl via inkjet printing in an adaptation of a previously reported procedure [132]. The SWCNTs ink was prepared by dispersing SWCNTs in a tetrahydrofuran (THF) solution at 0.1 mg/mL loading using a probe tip sonicator (QSonica, LLC). The suspension of SWCNTs in THF was drop cast at 1 μL on the quartz resonator surface. The devices were left to dry in a vacuum oven at room temperature for a minimum of 30 min to allow for solvent evaporation. Subsequently, 5 nL of a suspension of HHCl in methanol, various concentrations, was printed on the resonator surface using a BioFluidix PipeJet P9 piezoelectrically actuated pipette. After functionalization, the resonator board was stored under vacuum for a minimum of 24 hr to remove any remaining solvent.

7.2.4 Sensor Testing

Prior to sensor tests, the resonator board was secured to the instrumentation board and the 9.5 cm diameter chamber was sealed. The chamber was secured with an inline flow distribution system to achieve the desired concentrations of the analytes, Figure 7.2. Nitrogen was connected to multiple (n) mass flow controllers (MFC) in parallel. A subset ($n-1$) of the MFCs (MKS 1480A, 40 ccm) were connected to bubblers (Chemglass, AF-0085) with 10 mL of the analyte of interest in the bubbler. The other line (MKS 1179A, 500 ccm) remained a pure nitrogen source. The source lines were connected to a manifold, the output of which was connected directly to the chamber inlet.

The chamber was flushed with nitrogen at 500 cm^3/min to create an inert environment as the baseline for experimentation. Subsequently, the analyte gases were injected into the chamber to achieve the desired concentrations. Simultaneously, the oscillation frequencies were recorded every second with a 1 Hz resolution using the aforementioned myRio FPGA and an in-house LabVIEW program.

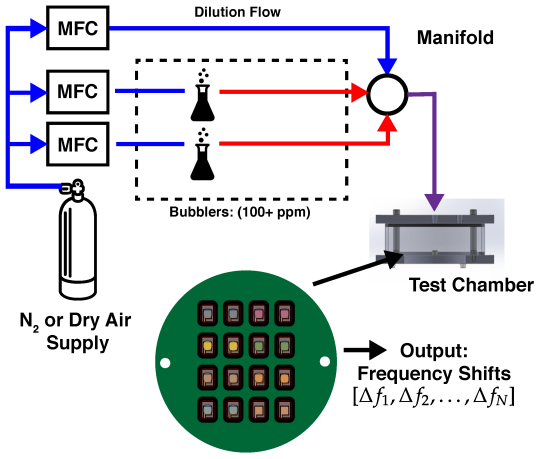

Figure 7.2. Experimental setup for gas testing of oscillators for xylene detection.

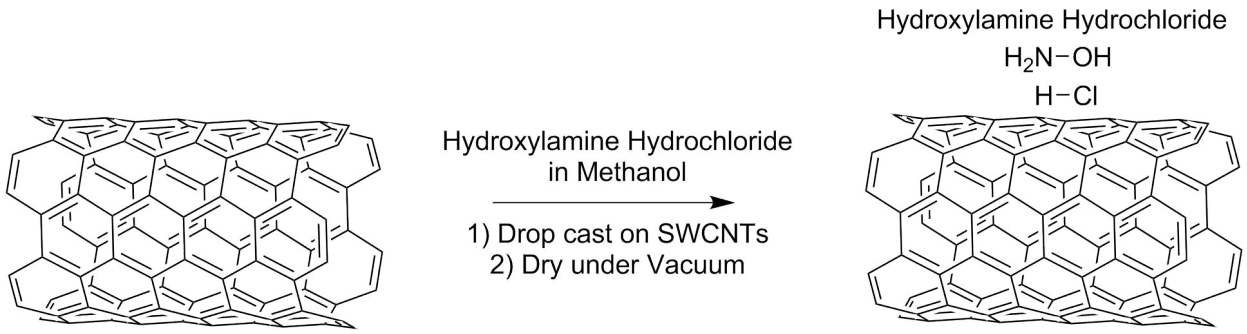

Figure 7.3. Schematic illustration of the chemical synthesis functionalization of the HHCl SWCNTs. A diluted solution of HHCl in methanol ranging from 0.2 mg/mL to 100 mg/mL was drop cast printed onto SWCNTs and then dried under vacuum prior to device testing.

7.3 Results

7.3.1 Chemical Characterization

SWCNTs were functionalized with HHCl, Figure 7.3, to observe if the dispersion of SWCNTs was concentration dependent. Additionally, Raman spectroscopy was used to investigate if the dispersion of the SWCNTs had an impact on the structural integrity of the SWCNTs. The Raman spectra is shown in Figure 7.4. Additionally, XRDs of the SWCNTs, SWCNTs after HHCl 1 mg/mL and 100 mg/mL, and HHCl can be observed in Figure 7.5 and Figure 7.6 below.

7.3.2 Sensor Testing

To determine the effect of HHCl concentration on oscillation frequency, a device with 32 MHz resonant elements was created. The 16 Pierce oscillators were divided into 6 groups to determine the functional chemistry on each device (Table 7.1). Note two resonators were left unfunctionalized to serve as a reference channels to account for changes in temperature and humidity. The board was exposed to five 20 min xylene pulses at 100 ppm using the aforementioned experimental setup ($n = 2$), see Figure 7.2, with each pulse separated by 20 min of nitrogen. Table 7.1 details the minimum, mean, and maximum frequency shift of each

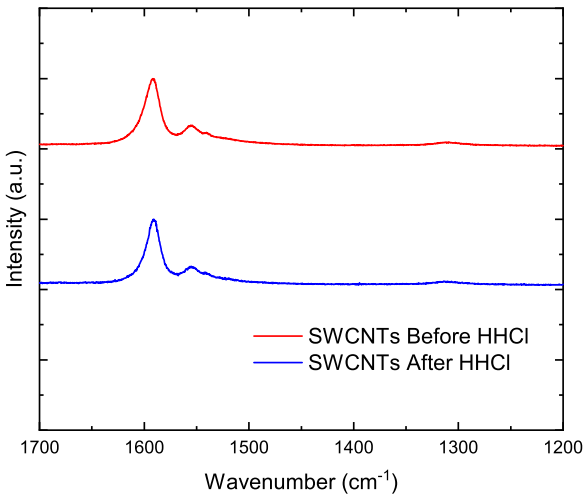

Figure 7.4. Raman spectra of SWCNTs before and after the drop casting of the 100 mg/mL HHCl solution. The Raman spectra shows similar peak locations and peak intensities before and after HHCl indicating that no structural changes occurred on the surface of the nanotubes.

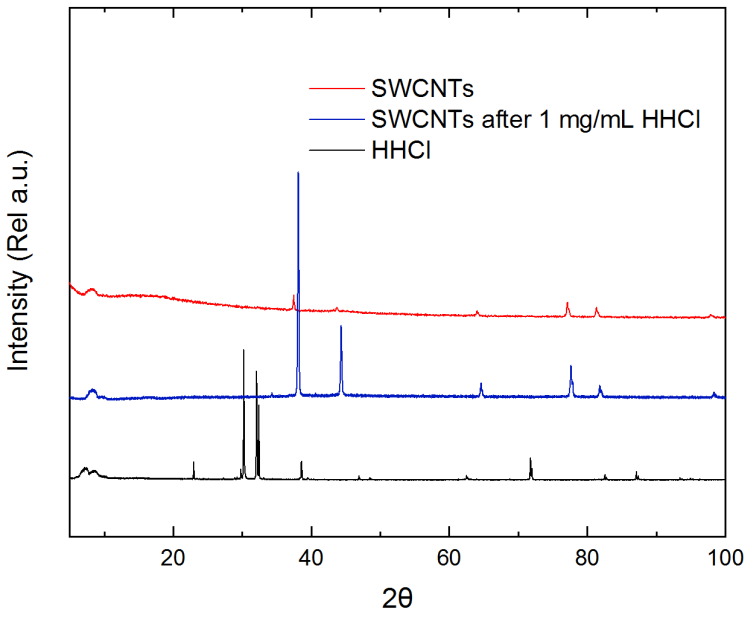

Figure 7.5. Comparison XRD of the SWCNTs, SWCNTs after HHCl Treatment at 1 mg/mL, and HHCl separately. A different XRD pattern for each of the different samples was observed. Note important peak location at 38.11 for the SWCNTs after HHCl Treatment at 1 mg/mL.

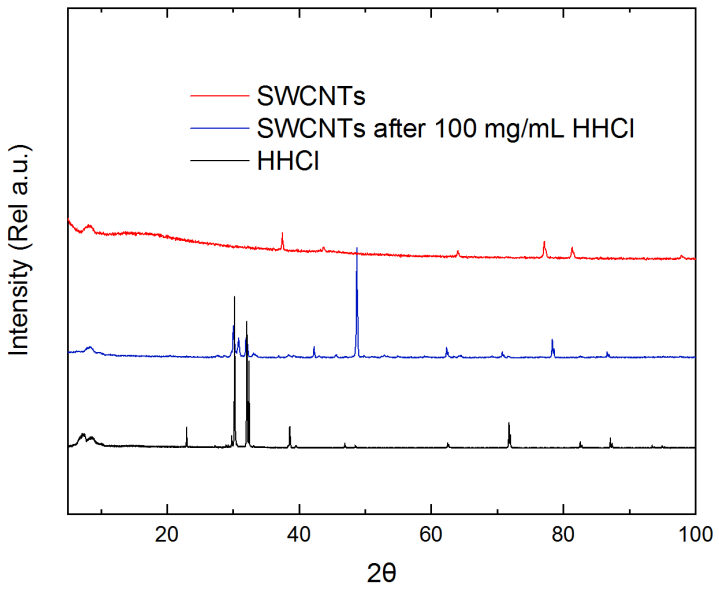

Figure 7.6. Comparison XRD of the SWCNTs, SWCNTs after HHCl Treatment at 100 mg/mL, and HHCl separately. A different XRD pattern for each of the different samples was observed. Note important peak location at 48.6 for the SWCNTs after HHCl Treatment at 100 mg/mL.

Table 7.1.
The minimum, mean, and maximum shift of resonator groups exposed to five pulses of 100 ppm of xylene. Note that the first group was not functionalized to account for temperature and humidity changes.

No. of Resonators	HHCl (mg/mL)	SWCNTs (mg/mL)	Min Shift (Hz)	Mean Shift (Hz)	Max Shift (Hz)
2	None	None	0	6	13
3	25	0.1	2	15	41
3	5	0.1	5	29	100
3	1	0.1	0	29	90
3	0.2	0.1	0	13	24
2	None	0.1	0	9	26

resonator group in response to 100 ppm of xylene. Figure 7.7 is the oscillation frequency of a single channel from Table 7.1 to demonstrate the repeatable nature of adsorption and desorption. The yellow bars indicate the concentration of xylene and the blue lines indicate the oscillation frequency of each device. It should be noted that the device was still reaching a steady state under test conditions during the first 20 minutes.

To determine the selectivity of the device to analytes similar to xylene, devices were exposed to toluene, xylene, and trimethylbenzene while the oscillation frequency was recorded. A 16 MHz resonator board was divided into two groups, as detailed in Table 7.2. Note only 10 resonators on the board were used in this test. Figure 7.8 shows the oscillation frequency of the devices in response to xylene, toluene, and trimethylbenzene. The blue lines indicate the oscillation frequency and the yellow, purple, and red bars represent the concentration of xylene, toluene, and trimethylbenzene, respectively, in ppm. Each analyte pulse was 20 min and was separated by 30 min of nitrogen.

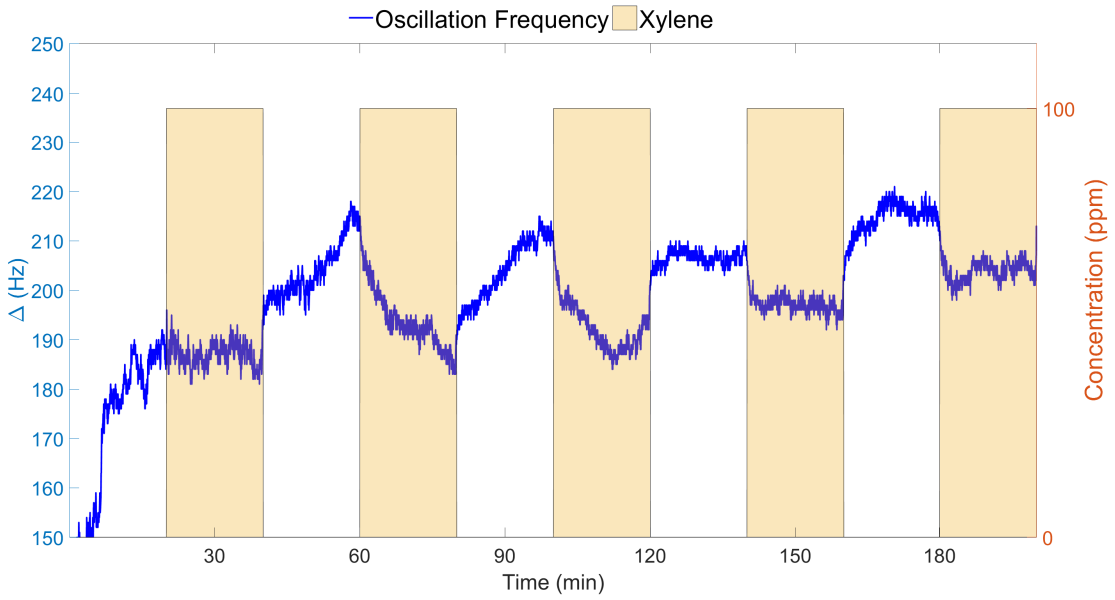

Figure 7.7. The oscillation frequency of a single resonator functionalized with 0.2 mg/mL of HHCl and 0.1 mg/mL SWCNTs. The blue line indicates oscillation frequency and the yellow bars indicate the concentration of xylene in the chamber.

Table 7.2.
Functional materials deposited on the resonators for toluene, xylene, and trimethylbenzene selectivity tests.

Resonators	HHCl (mg/mL)	SWCNTs (mg/mL)	Figure 7.8 Subplot
4	None	None	(a)
6	1	0.1	(b)

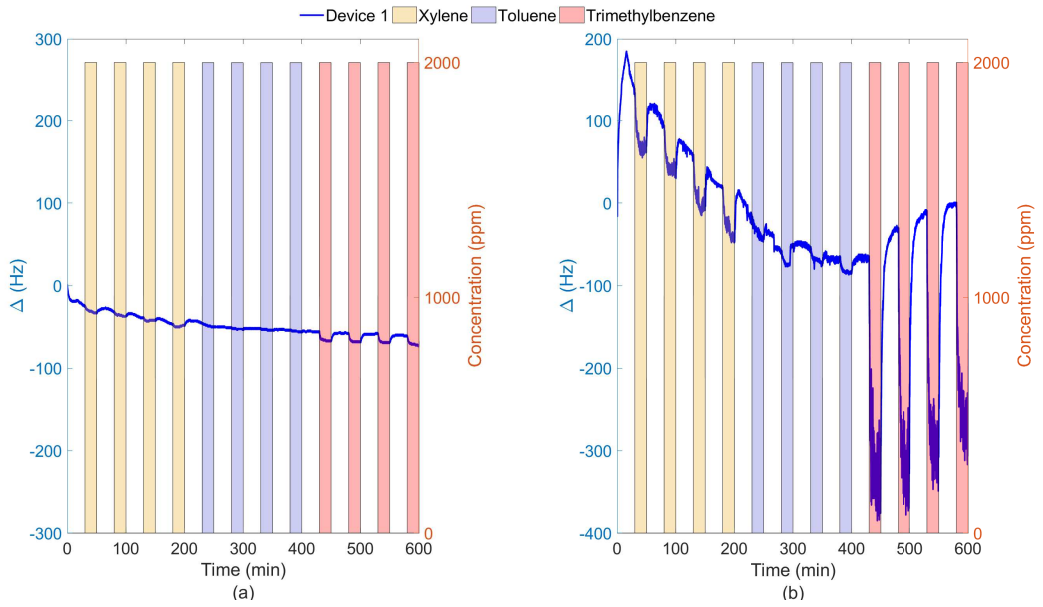

Figure 7.8. The oscillation frequency of devices exposed to 2000 ppm of either xylene, toluene, or trimethylbenzene. The blue lines represent the oscillation frequency of the device while the yellow, purple, and red bars indicate the concentration of xylene, toluene, and trimethylbenzene, respectively. The devices were functionalized as follows: (a) reference channels and (b) 1 mg/mL HHCl and SWCNTs.

7.4 Discussion

Pierce oscillators functionalized with SWCNTs and HHCl led to the detection of xylene at 100 ppm. This is the first demonstration of xylene detection using SWCNTs with HHCl. The repeatable nature of this sensing technique was shown in Figure 7.7. The oscillation frequency of the device shown had a rapid response to xylene. Additionally, the frequency nominally returned to its original value after exposure. This adsorption and desorption is critical when designing sensors for repeatable detection of analytes. To improve the sensitivity of the devices, 32 MHz resonators were used, as opposed to the 16 MHz resonators of other tests. This increase in nominal operating frequency resulted in a larger frequency shift due to added mass improving the sensitivity. However, there were trade-offs to be had with the improved sensitivity. The noise of the signal greatly increased, as seen in Figure 7.7. As such, when choosing the resonator for a sensing platform a trade-off must be analyzed to balance a desire of improved sensitivity or reduced noise, and thus improved selectivity. Ultimately, the oscillator-based approach which resulted in 1 Hz frequency resolution allowed for detection at 100 ppm, the TWA exposure limit, with a frequency shift above this noise floor. Additionally, the oscillation frequency was recorded once a second and thus captured information about the chamber with meaningful timescales.

It was determined that HHCl selectively disperses SWCNTs onto the resonator substrates which allows for the selective sensing of xylene. This dispersion allows for better surface coverage of the resonators specifically which allows for the selectivity of xylene versus other aromatic hydrocarbons. To achieve the maximum sensitivity of the devices the ideal concentration of deposited HHCl was determined. HHCl concentrations (5 mg/mL and 1 mg/mL) when paired with SWCNTs produced frequency shifts that were larger in magnitude than exclusively SWCNTs, as detailed in Table 7.1. It was shown that it is possible to detect xylene at 100 ppm using a combination of SWCNTs and HHCl; the reference channels had an average frequency shift of approximately 6 Hz while all other channels had an average above 12 Hz. The best performing groups, devices with 1 mg/mL and 5 mg/mL HHCl in methanol, both had average frequency shifts of approximately 29 Hz. The concentration dependence of HHCl is due to the fact that when the HHCl dissociates in solution, it forms

positive ions in solution which are attracted to the SWCNT's surface causing electrostatic repulsions among nanotubes [135]. The 1 mg/mL and 5 mg/mL HHCl solutions provided the necessary amount of ions to separate the tubes specifically which selectively fit one hydrocarbon over the other. Whereas at high concentrations of HHCl (100 mg/mL) there is not as high of selective adsorption as detailed in Figure 7.1.

To further expand and test the selectivity of the functional chemistry, devices were tested with xylene, toluene, and trimethylbenzene. Toluene and trimethylbenzene were of interest due to their similar aromatic structure to xylene. The average shifts in frequency to 2000 ppm of toluene, xylene, and trimethylbenzene were approximately 35 Hz, 71 Hz, and 206 Hz, respectively. The shifts in the reference channels for toluene, xylene, and trimethylbenzene were 2 Hz, 8 Hz, and 10 Hz, respectively. Due to the distinct differences in frequency shift when compared to the reference channels, it is concluded that the SWCNTs and HHCl combination produced a significant response to toluene, xylene, and trimethylbenzene. The difference in shifts due to each analytes resulted in a selective sensing approach. However, more work must be done to distinguish the analytes at different concentrations. For example, trimethylbenzene causes nominally three times the shift as xylene at the same concentration. But if there is three times more xylene than trimethylbenzene they could exhibit the same response. This risk could be mitigated through redundant channels with unique sensitivities or additional selective materials that can assist in discerning the unique analytes.

Carbon nanotube sensing of VOCs has been explored from the perspective of chemiresistive sensors where carbon nanotube sensors exhibited specific electronic sensing mechanisms [136, 137]. Additionally, these sensors require a need for structural integrity and alignment or other alterations in nanotube ordering to achieve adequate selective sensing of non-polar VOCs [138, 139]. The structural integrity and alignment of carbon nanotubes promotes the electronic properties of the carbon nanotubes upon the adsorption of analytes. On resonant mass sensors, these mechanisms are not necessarily required from an electronic perspective, but still are important in terms of enhancing the interaction between carbon nanotube and analyte. Thus, it was necessary to investigate if any structural changes or alignment alterations of the carbon nanotubes occurred. Therefore, the SWCNTs were investigated using Raman spectroscopy and XRD to determine if these features in the SWC-

NTs were occurring. The SWCNTs, when characterized with Raman spectroscopy, did not show any electronic structural changes. As shown in Figure 7.4, the HHCl drop cast SWCNTs showed similar D bands at 1330 cm^{-1}, D′ at 1610 cm^{-1}, and G bands at 1580 cm^{-1}. This indicates that the SWCNTs before and after functionalization had the same amount of sp^2 defects on the carbon nanotube surface. In other words, the surface structure of the SWCNTs did not change when in direct contact with HHCl. No chemical or structural changes occurred on the surface of the SWCNTs. This is an intriguing result because without disruption of the carbon cage structure and without excessive loss of the aromatic density of the surface of the SWCNTs, a great basis for modifying nanotubes to work in various sensor applications is formed [140]. Next, XRD testing was performed on the nanotubes to determine if there was any alignment of the nanotubes occurring. Alignment of SWCNTs has been observed through XRD testing previously [141, 142]. When observing the XRD spectra in Figures 7.5 and 7.6, 2Θ peaks were located at 38.1° and 48.6° for the SWCNTs after 1 mg/mL and 100 mg/mL HHCl treatment, respectively. These peaks did not exist in either the SWCNTs or HHCl samples when they were analyzed separately. These peaks have been determined to be due to the formation of in-plane spacing effects induced upon the exposure to HHCl. These in-plane spacing effects determine the distance between layers in a particular lattice [142]. This means the nanotubes are more spaced from each other at the 1 mg/mL HHCl treatment than the 100 mg/mL treatment. This means there is likely a selective concentration dependence between the space between nanotubes and the amount of HHCl used. This likely explains why the HHCl concentration made a difference in the sensing ability of xylene and why it was necessary to have the HHCl concentration set at 1 mg/mL and 5 mg/mL when performing these tests.

7.5 Conclusions

This work leveraged SWCNTs functionalized with HHCl for enhanced selective xylene sensing. This chemistry resulted in a novel, selective xylene adsorption pathway. For practical VOC monitoring, this approach achieved both meaningful concentration detection limits, 100 ppm, and sensing temporal resolution, 1 s. Through the use of 32 MHz resonators, the

repeatable detection of xylene at low concentrations was achieved. However, this frequency improvement resulted in a noise trade-off. As such, 16 MHz resonators were used with a reduction in noise to show the selective nature of the aromatic hydrocarbon detection by exhibiting a unique response to xylene, toluene, and trimethylbenzene. As such, sensor implementation can be tailored to sensitivity or selectivity through the choice of nominal operating frequency. Additionally, low-cost components and functional materials combined with additive manufacturing resulted in an efficient, reusable, economical VOC sensor.

8. CONCLUSIONS

The work presented herein demonstrated a sustained ability to print functional materials for a wide range of applications. These developments led to improvements in the additive manufacturing of energetic material. Additionally, metallic igniters fabricated with inkjet printing have been studied. Inkjet printing was further utilized to functionalize sensors for the detection of traumatic brain injuries and volatile organic compounds. These sensing platforms were further studied and improved to address various practical limitations of current sensing platforms.

Chapter 2 provided an extensive review of three printing systems for the deposition of nanothermite. This work included ink characterization at various solids loadings to determine the optimized ink formulation for each printing process. Furthermore, it presented a qualitative evaluation of the presented systems with respect to their ability to achieve several printing metrics, most importantly high sample throughput and ink solids loading. Finally, the BioFluidix system, which proved the optimal solution for high solids loading suspensions, was used to successfully deposit nanothermite and determine how geometric parameters affect the performance of the energetic material. Utilizing high speed videos and imaging processing techniques, the propagation speeds of printed nanothermite were reported. This work has contributed to safely and efficiently printing a wide range of other energetic materials.

In connection with the nanothermite deposition of Chapter 2, Chapter 3 detailed the printing of energetic materials through reactive inkjet printing. This work developed a dual-nozzle technique to separate the components of nanothermite into individual inks, that are relatively inert, and use drop kinetics to provide sufficient mixing for energetic performance during the printing process. In doing so, the risks associated with the storage and transportation of the constituent inks was greatly reduced. The reaction performance of the nanothermite printed with this method was comparable to that of the pre-mixed nanothermite. Thermal and STEM images suggested that the samples fabricated with the reactive

inkjet printing were more evenly mixed than the pre-mixed ink deposited with traditional inkjet printing.

Inkjet printing has proven to be valuable for the fabrication of metallic igniters, as detailed in Chapter 4. This work demonstrated the development of two igniters for energetic material, bridge wires and spark gaps. Both of these igniters were printed using traditional inkjet printing. The bridge wires were found to be a low-voltage igniter option that could ignite nanothermite, but proved to be sensitive to repeatability constraints. These were attributed to the dependence on consistent, and low, resistance values for the bridge wire which were not reliably achievable with inkjet printing. However, the spark gap igniters developed proved reliable for electrostatically sensitive energetic material.

Chapter 5 details how inkjet printing could be used with functional chemicals for the development of resonant mass sensors. This work utilized printing to functionalize resonators with a protein anti-body such that the resonator would be sensitive to s100β, a protein typically secreted after a traumatic brain injury. It was shown that this use of inkjet printing was sufficient to create devices with sensitivities previously unrealizable for detecting this protein. This approach should be easily transferrable to other sensing applications, biological or otherwise, in which the receptive chemistries can be made into an ink, and in turn, used to functionalize sensors.

To expand on the successes of analyte detection using resonators, Chapter 6 detailed the implementation of Pierce oscillator sensors functionalized with inkjet printing for the detection of volatile organic compounds. This work leveraged previous additive manufacturing successes to functionalize sensors. Through the use of an FPGA controlled frequency counter, the oscillator-based sensing array recorded the oscillation frequency of 16 parallel sensors once per second with 1 Hz resolution. This approach resulted in a large dataset that was used to train a linear regression model. Using least squares, the model was flipped and a predictive model for analyte concentration based on frequency shifts was deployed. This approach addressed many of the practical limitations of currents sensors by providing an array with redundant elements that had predictive capabilities and was selective to multiple analytes.

The platform developed in Chapter 6 was implemented for the selective detection of xylene, as detailed in Chapter 7. The repeatable detection of xylene at 100 ppm, the 8-hr TWA safe exposure limit for humans, was demonstrated by leveraging SWCNTs functionalized with HHCl. Additionally, these devices were exposed to toluene, xylene, and trimethylbenzene to investigate the selectivity of the devices. These advancements demonstrate a realistic application for oscillator-based sensors.

As a whole, this work demonstrated the sustained ability to additively manufacture functional materials. The ground work was laid for depositing energetic material and initiation devices. Additionally, sensing platforms for volatile organic compounds have been studied. Future work to expand on this work has begun in several areas. First, there is work studying new energetic material systems and destruction mechanisms using the techniques pioneered in this work. These advancements address current and realistic needs of defense customers while continuing to develop the understanding of inkjet printed energetic materials. Furthermore, the sensing work advanced with these efforts is continuing with the selective and sensitive detection of several harmful VOCs. These devices are working to improve sensor platforms and, in turn, human safety. The modeling steps in this work are translatable to other VOC sensors to push more advanced technology into the field. Ultimately, the work presented herein addressed many customer needs, laid the ground work for future major advancements, and addressed current gaps in scientific understanding.

REFERENCES

[1] A. K. Mogalicherla, S. Lee, P. Pfeifer, and R. Dittmeyer. Drop-on-Demand Inkjet Printing of Alumina Nanoparticles in Rectangular Microchannels. *Microfluidics and Nanofluidics*, 16(4):655–666, 2014.

[2] W. Boley, T. Bhuvana, B. Hines, R.A. Sayer, G. Chiu, T.S. Fisher, D. Bergstrom, R. Reifenberger, and G.U. Kulkarni. Inkjet Printing Involving Palladium Alkanethiolates and Carbon Nanotubes Functionalized with Single-Strand DNA. In *NIP and Digital Fabrication Conference*, pages 824–827, 2009.

[3] S. Limem, D. McCallum, G. G. Wallace, M. Panhuis, and P. Calvert. Inkjet Printing of Self-Assembling Polyelectrolyte Hydrogels. *Soft Matter*, 7(8):3818–3826, 2011.

[4] R. M. Verkouteren, G. Gillen, and D. W. Taylor. Piezoelectric Trace Vapor Calibrator. *Review of Scientific Instruments*, 77(8):085104, 2006.

[5] E. Windsor, M. Najarro, A. Bloom, B. Benner, R. Fletcher, R. Lareau, and G. Gillen. Application of Inkjet Printing Technology to Produce Test Materials of 1,3,5-Trinitro-1,3,5 Triazcyclohexane for Trace Explosive Analysis. *Analytical Chemistry*, 82(20):8519–8524, 2010.

[6] A. C. Ihnen, A. M. Petrock, T. Chou, P. J. Samuels, B. E. Fuchs, and W. Y. Lee. Crystal Morphology Variation in Inkjet-Printed Organic Materials. *Applied Surface Science*, 258(2):827–833, 2011.

[7] A. S. Tappan, J. P. Ball, and J. W. Colovos. Inkjet Printing of Energetic Materials: Sub-Micron Al/MoO_3 and Al/Bi_2O_3 Thermite. Technical report, Sandia National Laboratories (SNL-NM), Albuquerque, NM (United States), 2012.

[8] A. Liberska, J. T. Delaney, A. R. Liberski, D. Wett, U. Weiss, D. Nestler, B. Wielage, and U. S Schubert. *The Use of Inkjet Printing as a Tool for the Preparation of Nanothermites: Some First Result*. 2010. Australian Institute of High Energetic Materials.

[9] A. S. Tappan, J. Cesarano, and J. N. Stuecker. Nanocomposite Thermite Ink, US Patent: 8048242B1, 2011.

[10] A. Bietsch, J. Zhang, M. Hegner, H. P. Lang, and C. Gerber. Rapid Functionalization of Cantilever Array Sensors by Inkjet Printing. *Nanotechnology*, 15(8):873–880, 2004.

[11] J. B. Chang, V. Liu, V. Subramanian, K. Sivula, C. Luscombe, A. Murphy, J. Liu, and J. M. J. Fréchet. Printable Polythiophene Gas Sensor Array for Low-Cost Electronic Noses. *Journal of Applied Physics*, 100(1):014506, 2006.

[12] V. Kumar, J. W. Boley, Y. Yang, H. Ekowaluyo, J. K. Miller, G. T.-C. Chiu, and J. F. Rhoads. Bifurcation Based Mass Sensing Using Piezoelectrically Actuated Microcantilevers. *Applied Physics Letters*, 98(15):153510, 2011.

[13] V. Kumar, Y. Yang, J. W. Boley, G. T.-C. Chiu, and J. F. Rhoads. Modeling, Analysis, and Experimental Validation of a Bifurcation Based Microsensor. *Journal of Microelectromechanical Systems*, 21(3):549–558, 2012.

[14] N. Bajaj, J. F. Rhoads, and G. T.-C. Chiu. Characterizing the Spatially Dependent Sensitivity of Resonant Mass Sensors using Inkjet Deposition. *Journal of Dynamic Systems, Measurement, and Control*, 139(11):114505–1145010, 2017.

[15] S. D. Hoath. *Fundamentals of Inkjet Printing: The Science of Inkjet and Droplets*. John Wiley and Sons, Inc., 2015.

[16] N. Morita, A. A. Khalate, A. M. van Buul, and H. Wijshoff. Inkjet Printheads. *Fundamentals of Inkjet Printing*, 1:57–92, 2016.

[17] S. K. Chou, W. M. Yang, K. J. Chua, J. Li, and K. L. Zhang. Development of Micro Power Generators – A Review. *Applied Energy*, 88(1):1–16, 2011.

[18] N. Chigier and T. Gemci. A Review of Micro Propulsion Technology. In *41st Aerospace Sciences Meeting and Exhibit*, pages 6–9, 2003.

[19] C. Rossi and D. Estève. Micropyrotechnics, a New Technology for Making Energetic Microsystems: Review and Prospective. *Sensors and Actuators A: Physical*, 120(2):297–310, 2005.

[20] K. Zhang, C. Rossi, M. Petrantoni, and N. Mauran. A Nano Initiator Realized by Integrating Al/CuO-Based Nanoenergetic Materials With a Au/Pt/Cr Microheater. *Journal of Microelectromechanical Systems*, 17(4):832–836, 2008.

[21] C. S. Staley, C. J. Morris, R. Thiruvengadathan, S. J. Apperson, K. Gangopadhyay, and S. Gangopadhyay. Silicon-Based Bridge Wire Micro-Chip Initiators for Bismuth Oxide–Aluminum Nanothermite. *Journal of Micromechanics and Microengineering*, 21(11):115015, 2011.

[22] C. Rossi. Two Decades of Research on Nano-Energetic Materials. *Propellants, Explosives, Pyrotechnics*, 39(3):323–327, 2014.

[23] A. S. Rogachev and A. S. Mukasyan. Combustion of Heterogeneous Nanostructural Systems (Review). *Combustion, Explosion, and Shock Waves*, 46(3):243–266, 2010.

[24] K. T. Sullivan, J. D. Kuntz, and A. E. Gash. Electrophoretic Deposition and Mechanistic Studies of Nano-Al/CuO Thermites. *Journal of Applied Physics*, 112(2):024316, 2012.

[25] V. E. Sanders, B. W. Asay, T. J. Foley, B. C. Tappan, A. N. Pacheco, and S. F. Son. Reaction Propagation of Four Nanoscale Energetic Composites (Al/MoO_3, Al/WO_3, Al/CuO, and Bi_2O_3). *Journal of Propulsion and Power*, 23(4):707–714, 2007.

[26] S. F. Son, B. W. Asay, T. J. Foley, R. A. Yetter, M. H. Wu, and G. A. Risha. Combustion of Nanoscale Al/MoO_3 Thermite in Microchannels. *Journal of Propulsion and Power*, 23(4):715–721, 2007.

[27] P. J. Smith and A. Morrin. Reactive Inkjet Printing. *Journal of Materials Chemistry*, 22(22):10965–10970, 2012.

[28] P. Krober, J. T. Delaney, J. Perelaer, and U. S. Schubert. Reactive Inkjet Printing of Polyurethanes. *Journal of Materials Chemistry*, 19(29):5234–5238, 2009.

[29] M. Abulikemu, E. H. Da'as, H. Haverinen, D. Cha, M. A. Malik, and G. E. Jabbour. In Situ Synthesis of Self-Assembled Gold Nanoparticles on Glass or Silicon Substrates through Reactive Inkjet Printing. *Angewandte Chemie*, 126(2):430–433, 2014.

[30] Z-K. Kao, Y-H. Hung, and Y-C. Liao. Formation of Conductive Silver Films via Inkjet Reaction System. *Journal of Materials Chemistry*, 21(46):18799–18803, 2011.

[31] A. Hofmann, H. Laucht, D. Kovalev, Victor Y. T., J. Diener, N. Künzner, and E. Gross. Explosive Composition and Its Use, US Patent: 6984274B2, 2006.

[32] J. H. Evans. Airbag Igniter and Method of Manufacture, US Patent: 5639986A, 1997.

[33] D. H. Lewis, S. W. Janson, R. B. Cohen, and E. K. Antonsson. Digital Micropropulsion. *Sensors and Actuators A: Physical*, 80(2):143–154, 2000.

[34] T. A. Baginski, T. S. Parker, and W. D. Fahey. Electro-Explosive Device with Laminate Bridge, US Patent: 6925938B2, 2005.

[35] B. Neyer, D. R. Knick, P. T. Moore, and R. Tomasoski. Initiator, US Patent: 9534875B2, 2017.

[36] R. Varesh. Electric Detonators: EBW and EFI. *Propellants, Explosives, Pyrotechnics*, 21(3):150–154, 1996.

[37] C. S. Staley, C. J. Morris, R. Thiruvengadathan, S. J. Apperson, K. Gangopadhyay, and S. Gangopadhyay. Silicon-Based Bridge Wire Micro-Chip Initiators for Bismuth Oxide–Aluminum Nanothermite. *Journal of Micromechanics and Microengineering*, 21(11):115015, 2011.

[38] J. C. Fisher. Ignitor with Printed Electrostatic Discharge Spark Gap, US Patent: 6467414B1, 2002.

[39] R. Reynolds, C. Nance, and A. Cunningham. Plastic Encapsulated Energetic Material Initiation Device, US Patent: 20050235858A1, 2005.

[40] P. Chen, N.-T. Huang, M.-T. Chung, T. T. Cornell, and K. Kurabayashi. Label-Free Cytokine Micro- and Nano-Biosensing Towards Personalized Medicine of Systemic Inflammatory Disorders. *Advanced Drug Delivery Reviews*, 95:90–103, 2015.

[41] C. Ziegler. Cantilever-Based Biosensors. *Analytical and Bioanalytical Chemistry*, 379(7-8):946–959, 2004.

[42] J. Rickert, A. Brecht, and W. Göpel. Quartz Crystal Microbalances for Quantitative Biosensing and Characterizing Protein Multilayers. *Biosensors and Bioelectronics*, 12(7):567–575, 1997.

[43] R. E. Speight and M. A. Cooper. A Survey of the 2010 Quartz Crystal Microbalance Literature. *Journal of Molecular Recognition*, 25(9):451–473, 2012.

[44] L. A. Beardslee, O. Brand, and F. Josse. Resonant MEMS Chemical Sensors. In *Resonant MEMS*, pages 355–390. Wiley-Blackwell, 2015.

[45] N. Bajaj, A. B. Sabater, J. N. Hickey, G. T.-C. Chiu, and J. F. Rhoads. Design and Implementation of a Tunable, Duffing Like Electronic Resonator via Nonlinear Feedback. *Journal of Microelectromechanical Systems*, 25(1):2–10, 2016.

[46] V.-N. Nguyen, S. Baguet, C.-H. Lamarque, and R. Dufour. Bifurcation Based Micro-/Nanoelectromechanical Mass Detection. *Nonlinear Dynamics*, 79(1):647–662, 2015.

[47] J. Toledo, T. Manzaneque, V. Ruiz-Díez, F. Jiménez-Márquez, M. Kucera, G. Pfusterschmied, E. Wistrela, U. Schmid, and J. L. Sánchez-Rojas. Out-of-Plane Piezoelectric Microresonator and Oscillator Circuit for Monitoring Engine Oil Contamination with Diesel. In *Smart Sensors, Actuators, and MEMS VII; and Cyber Physical Systems*, volume 9517, page 95170C. International Society for Optics and Photonics, 2015.

[48] T. Manzaneque, V. Ruiz-Díez, J. Hernando-García, E. Wistrela, M. Kucera, U. Schmid, and J. L. Sánchez-Rojas. Piezoelectric MEMS Resonator-Based Oscillator for Density and Viscosity Sensing. *Sensors and Actuators A: Physical*, 220(1):305–315, 2014.

[49] H. C. Hao, K. T. Tang, P. H. Ku, J. S. Chao, C. H. Li, C. M. Yang, and D. J. Yao. Development of a Portable Electronic Nose Based on Chemical Surface Acoustic Wave Array with Multiplexed Oscillator and Readout Electronics. *Sensors and Actuators B: Chemical*, 146(2):545–553, 2010.

[50] F. Liu and M. Hossein-Zadeh. Mass Sensing With Optomechanical Oscillation. *IEEE Sensors Journal*, 13(1):146–147, 2013.

[51] A. T. Nimal, Mohan Singh, U. Mittal, and R. D. S. Yadava. A Comparative Analysis of One-Port Colpitt and Two-Port Pierce SAW Oscillators for DMMP Vapor Sensing. *Sensors and Actuators B: Chemical*, 114(1):316–325, 2006.

[52] L. Spinelle, M. Gerboles, G. Kok, S. Persijn, and T. Sauerwald. Review of Portable and Low-Cost Sensors for the Ambient Air Monitoring of Benzene and Other Volatile Organic Compounds. *Sensors (Switzerland)*, 17(7):1520–1550, 2017.

[53] M. Leidinger, T. Sauerwald, W. Reimringer, G. Ventura, and A. Schütze. Selective Detection of Hazardous VOCs for Indoor Air Quality Applications using a Virtual Gas Sensor Array. *Journal of Sensors and Sensor Systems*, 3(2):253–263, 2014.

[54] A. D. Wilson. Review of Electronic-Nose Technologies and Algorithms to Detect Hazardous Chemicals in the Environment. *Procedia Technology*, 1:453–463, 2012.

[55] S. De Vito, E. Massera, M. Piga, L. Martinotto, and G. Di Francia. On Field Calibration of an Electronic Nose for Benzene Estimation in an Urban Pollution Monitoring Scenario. *Sensors and Actuators B: Chemical*, 129(2):750–757, 2008.

[56] W. Miekisch, J. Herbig, and J. K. Schubert. Data Interpretation in Breath Biomarker Research: Pitfalls and Directions. *Journal of Breath Research*, 6(3):036007, 2012.

[57] N. Queralto, A. N. Berliner, B. Goldsmith, R. Martino, P. Rhodes, and S. H. Lim. Detecting Cancer by Breath Volatile Organic Compound Analysis: A Review of Array-Based Sensors. *Journal of Breath Research*, 8(2):027112, 2014.

[58] M. Calleja, P. M. Kosaka, A. San Paulo, and J. Tamayo. Challenges for Nanomechanical Sensors in Biological Detection. *Nanoscale*, 4(16):4925–4938, 2012.

[59] Q. Lan, R. Vermeulen, M. Dosemeci, M. Shen, B. P. Alter, C. Rabkin, S. Chanock, R. B. Hayes, M. Linet, N. Rothman, L. Zhang, W. Guo, M. T. Smith, G. Li, S. Yin, R. S. Weinberg, S. M. Rappaport, S. Waidyanatha, S. Kim, Y. Wu, and W. Kopp. Hematotoxicity in Workers Exposed to Low Levels of Benzene. *Science*, 306(5702):1774–1776, 2004.

[60] J. R. Meeks and C. R. Mackerer. Health Effects of the Alkylbenzenes. *Toxicology and Industrial Health*, 4(1):49–75, 1988.

[61] F. M. Peng, P. H. Xie, Y. G. Shi, J. D. Wang, W. Q. Liu, and H. Y. Li. Photoionization Detector For Portable Rapid GC. *Chromatographia*, 65(5-6):331–336, 2007.

[62] P. Jacquinot, A. W. E. Hodgson, P. C. Hauser, B. Müller, and B. Wehrli. Amperometric Detection of Gaseous Ethanol and Acetaldehyde at Low Concentrations on an Au–Nafion Electrode. *Analyst*, 124(6):871–876, 1999.

[63] N. Miura, G. Lu, and N. Yamazoe. High-Temperature Potentiometric/Amperometric Nox Sensors Combining Stabilized Zirconia with Mixed-Metal Oxide Electrode. *Sensors and Actuators B: Chemical*, 52(1):169–178, 1998.

[64] M. Kadosaki, T. Terasawa, K. Tanino, and C. Tatuyama. Exploration of Highly Sensitive Oxide Semiconductor Materials to Indoor-Air Pollutants. *IEEJ Transactions on Sensors and Micromachines*, 119(7):383–389, 1999.

[65] M. Kadosaki, S. Yamazaki, S. Fujiki, K. Tanino, and C. Tatsuyama. Development of SnO_2-Based Gas Sensors for Detection of Volatile Organic Compounds. *IEEJ Transactions on Sensors and Micromachines*, 121(7):395–401, 2001.

[66] S. C. Terry, J. H. Jerman, and J. B. Angell. A Gas Chromatographic Air Analyzer Fabricated on a Silicon Wafer. *IEEE Transactions on Electron Devices*, 26(12):1880–1886, 1979.

[67] H. Lahlou, X. Vilanova, and X. Correig. Gas Phase Micro-Preconcentrators for Benzene Monitoring: A Review. *Sensors and Actuators B: Chemical*, 176:198–210, 2013.

[68] K. Arshak, E. Moore, G.M. Lyons, J. Harris, and S. Clifford. A Review of Gas Sensors Employed in Electronic Nose Applications. *Sensor Review*, 24(2):181–198, 2004.

[69] J. Janata and A. Bezegh. Chemical Sensors. *Analytical Chemistry*, 60(12):62–74, 1988.

[70] C. K. Ho, M. T. Itamura, M. J. Kelley, and R. C. Hughes. *Review of Chemical Sensors for In-Situ Monitoring of Volatile Contaminants*. U.S. Department of Energy, Sandia National Lab, 2001.

[71] A. K. Murray, W. A. Novotny, T. J. Fleck, I. E. Gunduz, S. F. Son, G. T. C Chiu, and J. F. Rhoads. Selectively-Deposited Energetic Materials: A Feasibility Study of the Piezoelectric Inkjet Printing of Nanothermites. *Additive Manufacturing*, 22:69–74, 2018.

[72] M. Petrantoni, C. Rossi, L. Salvagnac, V. Conédéra, A. Estève, C. Tenailleau, P. Alphonse, and Y. J. Chabal. Multilayered Al/CuO Thermite Formation by Reactive Magnetron Sputtering: Nano versus Micro. *Journal of Applied Physics*, 108(8):084323, 2010.

[73] K. Meeks, M. L. Pantoya, and C. Apblett. Deposition and Characterization of Energetic Thin Films. *Combustion and Flame*, 161(4):1117–1124, 2014.

[74] C. Ru, J. Luo, S. Xie, and Y. Sun. A Review of Non-Contact Micro- and Nano-Printing Technologies. *Journal of Micromechanics and Microengineering*, 24(5):053001, 2014.

[75] P. Calvert. Inkjet Printing for Materials and Devices. *Chemistry of Materials*, 13(10):3299–3305, 2001.

[76] R. R. Nellums, B. C. Terry, B. C. Tappan, S. F. Son, and L. J. Groven. Effect of Solids Loading on Resonant Mixed Al-Bi_2O_3 Nanothermite Powders. *Propellants, Explosives, Pyrotechnics*, 38(5):605–610, 2013.

[77] T. J. Fleck. *Additive Manufacturing of Energetic Materials and Its Uses in Various Applications*. M.S.M.E. Thesis, Purdue University, United States – Indiana, 2017.

[78] J. F. Dijksman and A. Pierik. Dynamics of Piezoelectric Print-Heads. In *Inkjet Technology for Digital Fabrication*, pages 45–86. Wiley-Blackwell, 2014.

[79] Novele IJ-220: Printed Electronics Substrate – Inkjet Receptive. Technical report, NovaCentrix, 2011.

[80] T. Driessen and R. Jeurissen. Drop Formation in Inkjet Printing. *Fundamentals of Inkjet Printing*, pages 93–116, 2016.

[81] A. K. Murray, W. A. Novotny, N. Bajaj, I. E. Gunduz, S. F. Son, G. T-C. Chiu, and J. F. Rhoads. Piezoelectric Inkjet Printed Metallic Igniters. *Journal of Imaging Science and Technology*, 62(4):040406, 2018.

[82] A. K. Murray, T. Isik, V. Ortalan, I. E. Gunduz, S. F. Son, G. T.-C. Chiu, and J. F. Rhoads. Two-Component Additive Manufacturing of Nanothermite Structures via Reactive Inkjet Printing. *Journal of Applied Physics*, 122(18):184901, 2017.

[83] W. A. Novotny. *Inkjet Printing of Metallic Initiators*. M.S.M.E. Thesis, Purdue University, United States – Indiana, 2017.

[84] J. E. Bengston and G. B. Larson. Method for Fabricating Printed Circuits, US Patent: 5235139A, 1993.

[85] C. F. Coombs. *Printed Circuits Handbook*. McGraw-Hill, Inc., 1987.

[86] H. Sirringhaus, T. Kawase, R. H. Friend, T. Shimoda, M. Inbasekaran, W. Wu, and E. P. Woo. High-Resolution Inkjet Printing of All-Polymer Transistor Circuits. *Science*, 290(5499):2123–2126, 2000.

[87] A. S. Tappan, J. P. Ball, and J. W. Colovos. Inkjet Printing of Energetic Materials. In *2011 MRS Fall Meeting*, Boston, MA, 2011.

[88] J. Perelaer, C. E. Hendriks, A. W. M. de Laat, and U. S. Schubert. One-Step Inkjet Printing of Conductive Silver Tracks on Polymer Substrates. *Nanotechnology*, 20(16):165303, 2009.

[89] A. Bonea, A. Brodeala, M. Vladescu, and P. Svasta. Electrical Conductivity of Inkjet Printed Silver Tracks. In *2012 35th International Spring Seminar on Electronics Technology*, pages 1–4, 2012.

[90] A. Arazna, K. Janeczek, and K. Futera. Mechanical and Thermal Reliability of Conductive Circuits Inkjet Printed on Flexible Substrates. *Circuit World*, 43(1):9–12, 2017.

[91] C.-H. Chen, J. A. Yeh, and P.-J. Wang. Electrical Breakdown Phenomena for Devices with Micron Separations. 16(7):1366–1374, 2006.

[92] Appendix C: Spark-Over Voltages. In *Electrostatic Discharge*, pages 255–257. Wiley-Blackwell, 2009.

[93] S. Bonisch, D. Pommerenke, and W. Kalkner. Broadband Measurement of ESD Rise-times to Distinguish Between Different Discharge Mechanisms. In *2001 Electrical Overstress/Electrostatic Discharge Symposium*, pages 371–382, 2001.

[94] M. J. Wadas, M. Tweardy, N. Bajaj, A. K. Murray, G. T. C. Chiu, E. A. Nauman, and J. F. Rhoads. Detection of Traumatic Brain Injury Protein Biomarkers With Resonant Microsystems. *IEEE Sensors Letters*, 1(6):1–4, 2017.

[95] L. M. Fischer, V. A. Wright, C. Guthy, N. Yang, M. T. McDermott, J. M. Buriak, and S. Evoy. Specific Detection of Proteins using Nanomechanical Resonators. *Sensors and Actuators B: Chemical*, 134(2):613–617, 2008.

[96] M. Varshney, P. S. Waggoner, C. P. Tan, K. Aubin, R. A. Montagna, and H. G. Craighead. Prion Protein Detection Using Nanomechanical Resonator Arrays and Secondary Mass Labeling. *Analytical Chemistry*, 80(6):2141–2148, 2008.

[97] M. S. Hanay, S. Kelber, A. K. Naik, D. Chi, S. Hentz, E. C. Bullard, E. Colinet, L. Duraffourg, and M. L. Roukes. Single-Protein Nanomechanical Mass Spectrometry in Real Time. *Nature Nanotechnology*, 7(9):602–608, 2012.

[98] T. G. Ksiazek, C. P. West, P. E. Rollin, P. B. Jahrling, and C. J. Peters. ELISA for the Detection of Antibodies to Ebola Viruses. *The Journal of Infectious Diseases*, 179(1):192–198, 1999.

[99] T. Hayakata, T. Shiozaki, O. Tasaki, H. Ikegawa, Y. Inoue, F. Toshiyuki, H. Hosotubo, F. Kieko, T. Yamashita, H. Tanaka, T. Shimazu, and H. Sugimoto. Changes in CSF S100β and Cytokine Concentrations in Early-Phase Severe Traumatic Brain Injury. *Shock*, 22(2):102–107, 2004.

[100] S. J. Martin and G. C. Frye. Polymer Film Characterization using Quartz Resonators. In *IEEE 1991 Ultrasonics Symposium,*, pages 393–398 vol.1, 1991.

[101] Abcam. Anti-S100β Antibody [EP1578y], 2017.

[102] R. L. Frank. Lumbar Puncture and Post-Dural Puncture Headaches: Implications for the Emergency Physician. *The Journal of Emergency Medicine*, 35(2):149–157, 2008.

[103] World Health Organization Regional Office for Europe. *WHO Guidelines for Indoor Air Quality: Selected Pollutants*. World Health Organization. Regional Office for Europe, 2010.

[104] A. Mirzaei, S. G. Leonardi, and G. Neri. Detection of Hazardous Volatile Organic Compounds (VOCs) by Metal Oxide Nanostructures-Based Gas Sensors: A Review. *Ceramics International*, 42(14):15119–15141, 2016.

[105] B. Szulczyński and J. Gębicki. Currently Commercially Available Chemical Sensors Employed for Detection of Volatile Organic Compounds in Outdoor and Indoor Air. *Environments*, 4(1):21–36, 2017.

[106] L. Spinelle, M. Gerboles, M. G. Villani, M. Aleixandre, and F. Bonavitacola. Field Calibration of a Cluster of Low-Cost Available Sensors for Air Quality Monitoring. Part A: Ozone and Nitrogen Dioxide. *Sensors and Actuators B: Chemical*, 215:249–257, 2015.

[107] K. Zeng, K. G. Ong, C. Mungle, and C. A. Grimes. Time Domain Characterization of Oscillating Sensors: Application of Frequency Counting to Resonance Frequency Determination. *Review of Scientific Instruments*, 73(12):4375–4380, 2002.

[108] J. Pettine, V. Petrescu, D. M. Karabacak, M. Vandecasteele, M. Crego-Calama, and C. Van Hoof. Power-Efficient Oscillator-Based Readout Circuit for Multichannel Resonant Volatile Sensors. *IEEE Transactions on Biomedical Circuits and Systems*, 6(6):542–551, 2012.

[109] M. D. Valdes, I. Villares, J. Farina, and M. J. Moure. A FPGA-Based Frequency Measurement System for High-Accuracy QCM Sensors. In *2008 34th Annual Conference of IEEE Industrial Electronics*, pages 1707–1712, 2008.

[110] B. E. DeMartini, J. F. Rhoads, M. A. Zielke, K. G. Owen, S. W. Shaw, and K. L. Turner. A Single Input Single Output Coupled Microresonator Array for the Detection and Identification of Multiple Analytes. *Applied Physics Letters*, 93(5):054102, 2008.

[111] J. H. Ware, J. D. Spengler, L. M. Neas, J. M. Samet, G. R. Wagner, D. Coultas, H. Ozkaynak, and M. Schwab. Respiratory and Irritant Health Effects of Ambient Volatile Organic Compounds: the Kanawha County Health Study. *American Journal of Epidemiology*, 137(12):1287–1301, 1993.

[112] L. Mølhave. Volatile Organic Compounds, Indoor Air Quality and Health. *Indoor Air*, 1(4):357–376, 1991.

[113] G. De Gennaro, G. Farella, A. Marzocca, A. Mazzone, and M. Tutino. Indoor and Outdoor Monitoring of Volatile Organic Compounds in School Buildings: Indicators Based on Health Risk Assessment to Single Out Critical Issues. *International Journal of Environmental Research and Public Health*, 10(12):6273–6291, 2013.

[114] L. C. Holcomb and B. S. Seabrook. Review: indoor Concentrations of Volatile Organic Compounds: Implications for Comfort, Health and Regulation. *Indoor Environment*, 4(1):7–26, 1995.

[115] Y. Chen, L.-N. Li, C.-Q. Yang, Z.-P. Hao, H.-K. Sun, and Y. Li. Countermeasures for Priority Control of Toxic VOC Pollution. *Huanjing Kexue*, 32(12):3469–3475, December 2011.

[116] Agency for Toxic Substances and Disease Registry. *Public Health Statement for Xylene*, 2007.

[117] R. Kandyala, S. P. Raghavendra, and S. Rajasekharan. Xylene: An Overview of Its Health Hazards and Preventive Measures. *Journal of Oral and Maxillofacial Pathology*, 14(1):1–5, 2010.

[118] K. Niaz, H. Bahadar, F. Maqbool, and M. Abdollahi. A Review of Environmental and Occupational Exposure to Xylene and Its Health Concerns. *EXCLI Journal*, 14:1167–1186, 2015.

[119] S. Abu Al Ragheb, A. S. Salhab, and S. S. Amr. Suicide by Xylene Ingestion. A Case Report and Review of Literature. *The American Journal Of Forensic Medicine And Pathology*, 7(4):327–329, 1986.

[120] R. Morley, D. W. Eccleston, C. P. Douglas, W. E. J. Greville, D. J. Scott, and J. Anderson. Xylene Poisoning: A Report on One Fatal Case and Two Cases of Recovery after Prolonged Unconsciousness. *BMJ*, 3(5720):442–443, 1970.

[121] National Academy of Sciences. *Emergency and Continuous Exposure Limits for Selected Airborne*, volume 2. 1984.

[122] Occupational Safety and Health Administrations. *Xylenes (o-, m-, p-isomers) ethylbenzene*, 1999.

[123] F. Qu, W. Shang, D. Wang, S. Du, T. Thomas, S. Ruan, and M. Yang. Coordination Polymer-Derived Multishelled Mixed Ni–Co Oxide Microspheres for Robust and Selective Detection of Xylene. *ACS Applied Materials & Interfaces*, 10(17):15314–15321, 2018.

[124] B.-Y. Kim, J.-W. Yoon, J. K. Kim, Y. C. Kang, and J.-H. Lee. Dual Role of Multiroom-Structured Sn-Doped Nio Microspheres for Ultrasensitive and Highly Selective Detection of Xylene. *ACS Applied Materials & Interfaces*, 10(19):16605–16612, 2018.

[125] B.-Y. Kim, J. H. Ahn, J.-W. Yoon, C.-S. Lee, Y. C. Kang, F. Abdel-Hady, A. A. Wazzan, and J.-H. Lee. Highly Selective Xylene Sensor Based on Nio/$Nimoo_4$ Nanocomposite Hierarchical Spheres for Indoor Air Monitoring. *ACS Applied Materials & Interfaces*, 8(50):34603–34611, 2016.

[126] J.-W. Yoon and J.-H. Lee. Toward Breath Analysis on a Chip for Disease Diagnosis Using Semiconductor-Based Chemiresistors: Recent Progress and Future Perspectives. *Lab on a Chip*, 17(21):3537–3557, 2017.

[127] A. Mirzaei, J.-H. Kim, H. W. Kim, and S. S. Kim. Resistive-Based Gas Sensors for Detection of Benzene, Toluene and Xylene (BTX) Gases: A Review. *Journal of Materials Chemistry C*, 6(16):4342–4370, 2018.

[128] X. Fan and B. Du. Selective Detection of Trace P-Xylene by Polymer-Coated QCM Sensors. *Sensors and Actuators B: Chemical*, 166:753–760, 2012.

[129] Z. Ihdene, A. Mekki, B. Mettai, R. Mahmoud, B. Hamada, and M. M. Chehimi. Quartz Crystal Microbalance VOCs Sensor Based on Dip Coated Polyaniline Emeraldine Salt Thin Films. *Sensors and Actuators B: Chemical*, 203:647–654, 2014.

[130] H Nanto, N Dougami, T Mukai, M Habara, E Kusano, A Kinbara, T Ogawa, and T Oyabu. A Smart Gas Sensor Using Polymer-Film-Coated Quartz Resonator Microbalance. *Sensors and Actuators B: Chemical*, 66(1):16–18, 2000.

[131] P. Clément, E. Llobet, C. Lucat, and H. Debéda. Use of a CNT-Coated Piezoelectric Cantilever with Double Transduction as a Gas Sensor for Benzene Detection at Room Temperature. *Procedia Engineering*, 87:708–711, 2014.

[132] S. Ishihara, J. Labuta, T. Nakanishi, T. Tanaka, and H. Kataura. Amperometric Detection of Sub-ppm Formaldehyde Using Single-Walled Carbon Nanotubes and Hydroxylamines: A Referenced Chemiresistive System. *ACS Sensors*, 2(10):1405–1409, 2017.

[133] W. Zhang, J. K. Sprafke, M. Ma, E. Y. Tsui, S. A. Sydlik, G. C. Rutledge, and T. M. Swager. Modular Functionalization of Carbon Nanotubes and Fullerenes. *Journal of the American Chemical Society*, 131(24):8446–8454, 2009.

[134] E.R. Edwards, E.F. Antunes, E.C. Botelho, M.R. Baldan, and E.J. Corat. Evaluation of Residual Iron in Carbon Nanotubes Purified by Acid Treatments. *Applied Surface Science*, 258(2):641–648, 2011.

[135] Y. Sabba and E. L. Thomas. High-Concentration Dispersion of Single-Wall Carbon Nanotubes. *Macromolecules*, 37(13):4815–4820, 2004.

[136] A. Wang, X.and Ugur, H. Goktas, N. Chen, M. Wang, N. Lachman, E. Kalfon-Cohen, W. Fang, B. L. Wardle, and K. K. Gleason. Room Temperature Resistive Volatile Organic Compound Sensing Materials Based on a Hybrid Structure of Vertically Aligned Carbon Nanotubes and Conformal OCVD/ICVD Polymer Coatings. *ACS Sensors*, 1(4):374–383, 2016.

[137] J. Li, Y. Lu, Q. Ye, M. Cinke, J. Han, and M. Meyyappan. Carbon Nanotube Sensors for Gas and Organic Vapor Detection. *Nano Letters*, 3(7):929–933, 2003.

[138] Y. Wang and J. T. W. Yeow. A Review Of Carbon Nanotubes-Based Gas Sensors. *Journal of Sensors*, 2009, 2009.

[139] B. R. Goldsmith, J. G. Coroneus, V. R. Khalap, A. A. Kane, G. A. Weiss, and P. G. Collins. Conductance-Controlled Point Functionalization of Single-Walled Carbon Nanotubes. *Science*, 315(5808):77–81, 2007.

[140] S. Manzetti and J.-C. P. Gabriel. Methods for Dispersing Carbon Nanotubes for Nanotechnology Applications: Liquid Nanocrystals, Suspensions, Polyelectrolytes, Colloids and Organization Control. *International Nano Letters*, 9(1):31–49, 2019.

[141] G. Liu, Y. Zhao, K. Deng, Z. Liu, W. Chu, J. Chen, Y. Yang, K. Zheng, H. Huang, W. Ma, L. Song, H. Yang, C. Gu, G. Rao, C. Wang, S. Xie, and L. Sun. Highly Dense and Perfectly Aligned Single-Walled Carbon Nanotubes Fabricated by Diamond Wire Drawing Dies. *Nano Letters*, 8(4):1071–1075, 2008.

[142] R. Das, S. B. Abd Hamid, M. Ali, S. Ramakrishna, and W. Yongzhi. Carbon Nanotubes Characterization by X-Ray Powder Diffraction – A Review. *Current Nanoscience*, 11(1):23–35, 2015.

VITA

Allison K. Murray received her B.S. and M.S. degrees in mechanical engineering from Purdue University in 2015 and 2018, respectively. Her research interests focus on advancing additive manufacturing processes with applications spanning energetic materials to volatile organic compound sensors. Through her graduate career Allison has been recognized for her teaching and research successes as a William E. Fontaine Research Fellow, a Ward A. Lambert Teaching Fellow, and a Women in Defense HORIZONS Scholar. Allison is currently enrolled in the School of Mechanical Engineering at Purdue University and is advised by Dr. Jeffrey Rhoads and Dr. George Chiu.

PUBLICATIONS

1. M. P. McConnell, **A. K. Murray**, B. W. Boudouris, I. E. Gunduz, S. F. Son, G. T.-C. Chiu, J. F. Rhoads. *Additively Manufactured Conductive Polymer Spark Gap Igniters*. Submitted 2018.
2. J. N. Hodul, **A. K. Murray**, N. F. Carneiro, J. Morris, B. W. Boudouris, J. F. Rhoads. *Tuning the Chemistry of Single-Walled Carbon Nanotubes for Selective Mass Uptake of Xylene on Resonant Sensors*. Submitted 2019.
3. **A. K. Murray**, J. R. Meseke, N. Bajaj, J. F. Rhoads. *A Field Programmable Gate Array Controlled Oscillator-Based Sensing Array for Improved Sensing Statistics*. Submitted 2019.
4. E. R. Westphal, **A. K. Murray**, M. P. McConnell, T. J. Fleck, G. T.-C. Chiu, J. F. Rhoads, I. E. Gunduz, S. F. Son. *The Effects of Confinement on the Prescribed Substrate Fracturing Performance of Printed Nanothermites*. Propellants, Explosives, Pyrotechnics. 2018. 44(1): p. 1-9.
5. **A. K. Murray**, W. A. Novotny, N. Bajaj, I. E. Gunduz, S. F. Son, G. T.-C. Chiu, J. F. Rhoads. *Piezoelectric Inkjet Printed Metallic Igniters*. Journal of Imaging Science and Technology. 2018. 62(4): p. 40406-1-40406-6.
6. **A. K. Murray**, W. A. Novotny, T. J. Fleck, I. E. Gunduz, S. F. Son, G. T.-C. Chiu, and J. F. Rhoads. *Selectively-Deposited Energetic Materials: A Feasibility Study of the Piezoelectric Inkjet Printing of Nanothermites*. Additive Manufacturing. 2018. 22: p. 69-74.
7. M. J. Wadas, M. Tweardy, N. Bajaj, **A. K. Murray**, G. T.-C. Chiu, E. A. Nauman, J. F. Rhoads. *Detection of Traumatic Brain Injury Protein Biomarkers with Resonant Microsystems*. IEEE Sensors Letters. 2017. 1(6): p. 1-4.
8. **A. K. Murray**, T. Isik, V. Ortalan, I. E. Gunduz, S. F. Son, G. T.-C. Chiu, and J. F. Rhoads. *Two-Component Additive Manufacturing of Nanothermite Structures via Reactive Inkjet Printing*. Journal of Applied Physics. 2017. 122(18): p. 184901.

9. T. J. Fleck, **A. K. Murray**, G. T.-C. Chiu, I. E. Gunduz, S. F. Son, and J. F. Rhoads. *Additive Manufacturing of Multifunctional Reactive Materials.* Additive Manufacturing. 2017. 17: p. 176-182.
10. T. J. Fleck, R. Ramachandran, **A. K. Murray**, W. A. Novotny, G. T.-C. Chiu, I. E. Gunduz, S. F. Son, and J. F. Rhoads. *Controlled Substrate Destruction Using Nanothermite.* Propellants, Explosives, Pyrotechnics. 2017. 42(6): p. 579-584.